

SNS SINGPRJ-10-PN0002-R01

Date: March 1, 2004

**CONCEPTUAL DESIGN DOCUMENT
FOR THE SING
(SNS INSTRUMENTS—NEXT GENERATION)
PROJECT**

SING *SNS Instruments - Next Generation*



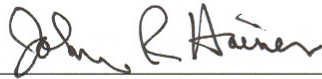
This report was prepared as an account of work sponsored by an agency of the United States government. Neither the United States government nor any agency thereof, nor any of their employees, makes any warranty, express or implied, or assumes any legal liability or responsibility for the accuracy, completeness, or usefulness of any information, apparatus, product, or process disclosed, or represents that its use would not infringe privately owned rights. Reference herein to any specific commercial product, process, or service by trade name, trademark, manufacturer, or otherwise, does not necessarily constitute or imply its endorsement, recommendation, or favoring by the United States government or any agency thereof. The views and opinions of authors expressed herein do not necessarily state or reflect those of the United States government or any agency thereof.

**CONCEPTUAL DESIGN DOCUMENT
FOR THE
SING (SNS INSTRUMENTS—NEXT GENERATION) PROJECT**

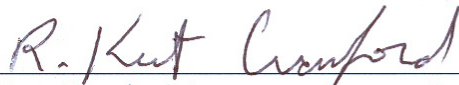
Date Published: March 2004

Prepared by
OAK RIDGE NATIONAL LABORATORY
P.O. Box 2008
Oak Ridge, Tennessee 37831-6285
managed by
UT-Battelle, LLC
for the
U.S. DEPARTMENT OF ENERGY
Office of Science
Basic Energy Science
under contract DE-AC05-00OR22725

CONCEPTUAL DESIGN DOCUMENT
FOR
SING (SNS INSTRUMENTS—NEXT GENERATION) PROJECT



John Haines, SING Project Manager



3/19/04

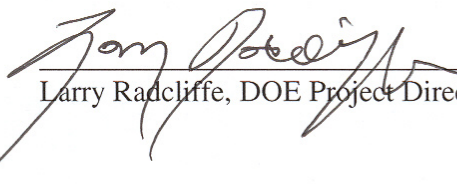
Kent Crawford, Instrument Systems Senior Team Leader



3/19/04

Ian Anderson, Experimental Facilities Division Director

Concurrence:



Larry Radcliffe, DOE Project Director, SING Project

TABLE OF CONTENTS

	Page
LIST OF FIGURES	v
LIST OF TABLES	vii
ACRONYMS	viii
1. SING PROJECT OVERVIEW	1
1.1 DESIRED OUTCOME AND REQUIREMENTS DEFINITION	1
1.1.1 Background	1
1.1.2 Summary Project Description	1
1.1.3 SING Project Scope	2
1.1.4 Performance Parameters Required to Obtain the Desired Outcome	3
1.1.5 Critical Decision 0 Approval	3
1.2 CONCEPTUAL DESIGNS FOR THE FIVE INSTRUMENTS	4
2. HIGH-PRESSURE DIFFRACTOMETER (SNAP)	5
2.1 SNAP INSTRUMENT OVERVIEW	5
2.1.1 Introduction	5
2.1.2 Instrument Summary	5
2.2 SNAP INSTRUMENT DETAILS	6
2.2.1 General Orientation	6
2.2.2 The Press	7
2.2.3 Bandwidth (Disk) Choppers	8
2.2.4 T ₀ Chopper	10
2.2.5 Moderator Choice	11
2.2.6 Focusing Super-Mirror Reflectors (Series of Supermirror Funnel)s	13
2.2.7 Resolution Function	15
2.3 POSITION-SENSITIVE DETECTORS	20
2.3.1 Introduction	20
2.3.2 Key Requirements	20
2.3.3 Choice of Detector Technology	21
3. HIGH-RESOLUTION CHOPPER SPECTROMETER (SEQUOIA)	25
3.1 SEQUOIA INSTRUMENT OVERVIEW	25
3.2 INCIDENT FLIGHT PATH	26
3.2.1 Moderator	26
3.2.2 T ₀ Chopper	27
3.2.3 Neutron Guide	27
3.2.4 Frame Overlap Chopper	27
3.2.5 Fermi Chopper	28
3.2.6 Collimators	28
3.2.7 Biological Shielding	28
3.3 SAMPLE CHAMBER	28
3.3.1 Vacuum Isolation	28
3.3.2 Sample Manipulation	29
3.4 FINAL FLIGHT PATH	30

TABLES OF CONTENTS (Continued)

	Page
3.4.1 Vacuum Vessel	30
3.4.2 Detectors	30
3.4.3 Shielding	30
3.5 COMPUTER HARDWARE AND DATA ACQUISITION	31
3.6 SAMPLE ENVIRONMENT	31
3.6.1 Closed Cycle Refrigerator (9–350 K)	31
3.6.2 Cryo-Furnace (2 –700 K)	31
3.7 INSTRUMENT PERFORMANCE	32
3.7.1 Intensity and Energy Resolution	32
3.7.2 Q Resolution and Range	35
4. SINGLE-CRYSTAL DIFFRACTOMETER (SCD)	41
4.1 SCD OVERVIEW: CURRENT TREND	41
4.2 INSTRUMENT DESCRIPTION	41
4.3 PERFORMANCE ESTIMATES AND DESIGN CHOICES	45
4.3.1 Choice of Moderator	45
4.3.2 Beam Guide or Beam Tube	48
4.3.3 Chopper Arrangement	48
4.3.4 Inelastic Discrimination Through Beam Conditioning	48
4.3.5 Instrument Functions and Performance	49
4.3.6 Further Issues	54
4.4 RELATIVE FLUX COMPARISON BETWEEN SNS AND IPNS	55
4.5 GUIDE GAINS	56
4.6 TIME-DISTANCE DIAGRAMS FOR CHOPPER CHOICES	57
4.7 PRELIMINARY DETECTOR ARRANGEMENT EVALUATIONS	59
5. DISORDERED MATERIALS DIFFRACTOMETER (NOMAD)	62
5.1 NOMAD INSTRUMENT OVERVIEW	62
5.2 INCIDENT BEAM CONSIDERATIONS	63
5.3 SAMPLE AND DETECTOR CONSIDERATIONS	65
5.4 COMPARISONS WITH OTHER INSTRUMENTS	66
6. HYBRID SPECTROMETER (HYSPEC)	68
6.1 HYSPEC INSTRUMENT OVERVIEW	68
6.2 PRIMARY SPECTROMETER (MONOCHROMATOR)	69
6.3 SAMPLE STAGE	71
6.4 SECONDARY SPECTROMETER (ANALYZER/DETECTOR)	71
6.5 POLARIZATION ANALYSIS	71
6.5.1 The Polarizing Crystal	72
6.5.2 The Polarization Analyzers	72
6.6 PERFORMANCE	75
6.6.1 Moderator Choice	76
6.6.2 Additional Advantages of the HYSPEC Concept	76
6.6.3 Future Considerations	76
REFERENCES	78

LIST OF FIGURES

Figure	Page
2.1 Stylized drawing of the high-pressure cell with incident beam collimation (or focusing optic) and detector location.....	6
2.2 Top view of the high-pressure cell as shown in Fig. 2.1	7
2.3 Line drawing of the three web open cylinder panoramic device in a three post press, based on the P-E design	8
2.4 Drawing of the frame press design with a hydraulic pancake-style cylinder on the bottom of the opening and a panoramic-type pressure cell.....	8
2.5 Timing diagrams for a two chopper system operating in the first frame (left plot) and second frame (right plot).....	9
2.6 d-spacing range versus scattering angle.....	10
2.7 Geometry used to calculate the T_0 chopper parameters	11
2.8 Pulse timing (FWHM) and flux profiles from various moderators as functions of wavelength....	12
2.9 Comparison of simulated data generated from the same sample, in the same scattering geometry, with the water moderator (blue) and with the poisoned decoupled hydrogen moderator (red)	13
2.10 Representation of a focusing system for very small samples	14
2.11 Focusing of neutron beam with series of rectangular supermirror funnels.....	16
2.12 Flux gain calculated with and without the focusing mirrors in place	17
2.13 Simulated diffraction peak.....	17
2.14 Neutron flux on sample with and without supermirror funnel system in place	18
2.15 Analytical form of the resolution function for selected wavelengths in the first frame.....	18
2.16 Simulated Bragg peak indicates asymmetry in the resolution function.....	19
2.17 Simulated resolution as a function of d-spacing at various angles in the large high-resolution bank.....	20
2.18 Detection efficiency for thermal neutrons in 15-mm gas depth @ 6 atm ^3He	21
2.19 Edge view of curved, wire segment.....	22
2.20 Arrangement of two of the proposed detectors, with significant angular coverage within the restrictions imposed by the gem anvil pressure cell	23
2.21 A curved detector, covering 120 by 15° with a radius of curvature of 0.7 m that has recently been commissioned for protein crystallography at LANSCE.....	24
3.1 Three-dimensional rendering of SEQUOIA	25
3.2 Schematic diagram of SEQUOIA with the components described in Sections 3.2 through 3.4 labeled	26
3.3 One degree of freedom allows q_1 to intersect \mathbf{Q} by rotation of ω	29
3.4 Flux on sample and Energy resolution for the SEQUOIA spectrometer	33
3.5 Flux on sample for ARCS (red) and SEQUOIA (blue) as a function of energy resolution, for incident energies of 50 and 500 meV	34
3.6 Finest possible \mathbf{Q} resolution for the SEQUOIA instrument for elastic scattering for several different incident energies.....	36
3.7 The components of \mathbf{Q} defined by the instrument geometry.....	37
3.8 Locus of \mathbf{Q} components for SEQUOIA	38
3.9 Locus of \mathbf{Q} components for ARCS.....	38
3.10 Finest possible \mathbf{Q} resolution perpendicular to the incident beam direction	39

LIST OF FIGURES (Continued)

Figure	Page
3.11	Finest possible Q resolution parallel to the incident beam direction 40
4.1	Schematic view of the SNS SCD 42
4.2	Figures 4.2a through 4.2d show further instrument details..... 43
4.3	FWHM for the hydrogen moderator (blue), the water moderator face with deep poisoning (green), and the water moderator face with shallow poisoning (red)..... 46
4.4	Simulated total peak flux intensity: (a) intensity $\times \lambda^2$, (b) intensity $\times \lambda^3$, and (c) for the hydrogen and the two water moderator faces 47
4.5	The peak time-width comparison shows a favorable profile for the hydrogen moderator, increasing linearly with wavelength 48
4.6	Detector pixel size w_D vs diffraction angle 2θ for incident angular divergence $\delta\theta_i = 0.5^\circ$ and $\delta d/d = 0.005$ 49
4.7	Resolution increase in d for pixel sizes between 0.5 and 5 mm, for $d_{\min} = 0.3 \text{ \AA}$ 50
4.8	Resolution increase in d , as a function of 2θ , for 0.5-, 1-, 1.5-, 2-, 2.5-, 3-, 3.5-, and 4-mm pixel sizes compared to that for 5-mm pixel size 50
4.9	Instrumental resolution $\delta d/d$ plotted vs incident angular divergence $\delta\theta$, assuming $2\theta = 90^\circ$ and detector pixel size $w_D = 1 \text{ mm}$ 51
4.10	Maximum resolved unit-cell repeat, as a function of diffraction angle 2θ , computed for $d_{\min} = 0.3, 0.5, 0.7, 0.9,$ and 1.2 \AA 52
4.11	Comparison of maximum resolvable unit cell repeats for the SNS SCD with ISIS SXD and IPNS SCD at $2\theta = 90^\circ$ 53
4.12	Acceptance diagram for 1.5- \AA neutrons incident on a 1-mm sample from a tapered $4\theta_c^{\text{Ni}}$ guide 56
4.13	Gain from a doubly tapered guide (rectangular funnel) for intensity on 1-mm ² sample 57
4.14a	Time-distance diagram for the first frame (0.5-5.07 \AA) 58
4.14b	Time-distance diagrams for the second frame (5.07-10.14 \AA) 59
4.15	The 44 crystal settings required to measure a full set of diffraction data on IPNS SCD 60
4.16	The seven crystal settings that would be required on IPNS SCD with three 2D detectors 60
4.17	Ten 2D detectors can shorten the measurement time from 44 to three settings..... 61
5.1	Overall view of NOMAD, showing extensive detector coverage (red and yellow) around the sample position (green)..... 62
5.2	Flux characteristics of water and decoupled poisoned hydrogen moderators at SNS 64
5.3	Conceptual arrangement of detector banks on NOMAD 65
6.1	Schematic showing the HYSPEC principle elements 68
6.2	Incident neutron spectrum before and after reflection from a PG monochromator: (a) $E_i = 5 \text{ meV}$; (b) $E_i = 15 \text{ meV}$ 70
6.3	Spatial distribution of two neutron polarizations on the detector as created by a single supermirror bender 74
6.4	Average beam polarization in each of the two beams..... 74
6.5	Calculated flux on sample for HYSPEC and other inelastic spectrometers planned for the SNS 75

LIST OF TABLES

Table	Page
4.1 SNS SCD instrument parameters	44
4.2 Flux ratios for SNS relative to IPNS	45
4.3 Comparison of the ISIS, IPNS, and SNS instruments	53
4.4 Estimated measurement times for hydrogenous samples with unit-cell repeats of 5, 10, 15, 20, 25, 50, 75, 100 Å	54
4.5 Detector design parameters	61
5.1 Comparison of NOMAD characteristics with current benchmark instruments	67
6.1 Instrument parameters	69

ACRONYMS

ANL	Argonne National Laboratory
ARCS	A High-Resolution Chopper Spectrometer (neutron-scattering instrument at SNS)
BES	Basic Energy Sciences
BNL	Brookhaven National Laboratory
CD	Critical Decision
CNCS	Cold Neutron Chopper Spectrometer (neutron-scattering instrument at SNS)
DOE	U.S. Department of Energy
EFAC	Experimental Facilities Advisory Committee (external advisory committee to SNS)
FOCUS	Time-of-Flight Spectrometer for Cold Neutrons at SINQ (neutron-scattering instrument at SINQ)
FWHM	Full Width at Half Maximum
GEM	General Materials diffractometer (neutron-scattering instrument at ISIS)
GeV	Gigaelectronvolt
GPa	GigaPascals
GPPD	General-Purpose Powder Diffractometer (neutron-scattering instrument at IPNS)
Hi Pr, PEARL	High-Pressure diffractometer (neutron-scattering instrument at ISIS)
HRCS	High-Resolution Chopper Spectrometer (another name for SEQUOIA)
HRMECS	High-Resolution Medium-Energy Chopper Spectrometer (neutron-scattering instrument at IPNS)
HYSPEC	HYbrid SPECTrometer (one of the SING instruments)
ILL	Institut Laue-Langevin (neutron scattering facility in France)
IPNS	Intense Pulsed Neutron Source (neutron-scattering facility at ANL)
IPNS SCD	Single-Crystal Diffractometer (neutron-scattering instrument at IPNS)
ISIS	Neutron-scattering facility at Rutherford-Appleton Laboratory, UK
LANSCE	Los Alamos Neutron Science Center
LRMECS	Low-Resolution Medium-Energy Chopper Spectrometer (neutron-scattering instrument at IPNS)
MAPS	Multi-Angle Chopper Spectrometer (neutron-scattering instrument at ISIS)
MC	Monte Carlo
MCNPX	Monte Carlo code for neutronics calculations
McStas, MCSTAS	Monte Carlo Simulation of Triple-Axis Spectrometers (Monte Carlo code for instrument simulation)
MeV	Megaelectronvolt
MIE	Major Item of Equipment
NIST	National Institute of Standards and Technology (neutron-scattering facility at that Institute)
NOMAD	Nanoscale Ordered Materials Diffractometer (one of the SING instruments)
ORNL	Oak Ridge National Laboratory
P-E	Paris-Edinburgh (particular type of high-pressure cell)
PEARL, Hi Pr	High-Pressure diffractometer (neutron-scattering instrument at ISIS)
PG	Pyrolytic Graphite
POWGEN3	POWder diffractometer GENERation 3 (one of the SNS neutron-scattering instruments)
RAID	Redundant Array of Independent Disks (high-performance computer disk system)
SANDALS	Small-Angle Neutron Diffractometer for Amorphous and Liquid Samples (neutron-scattering instrument at ISIS)

ACRONYMS (Continued)

SBIR	Small B usiness I nnovative R esearch
SC	SC ience (DOE Office)
SCD	S ingle- C ystal D iffractometer (one of the SING instruments)
SEQUOIA	H igh- R esolution C hopper S pectrometer (one of the SING instruments)
SING	S NS I nstruments- N ext G eneration
SINQ	S wiss S pallation N eutron S ource (neutron-scattering facility in Switzerland)
SNAP	S pallation N eutrons A t P ressure (one of the SING instruments)
SNS	S pallation N eutron S ource (neutron-scattering facility at ORNL)
SXD	S ingle X tal D iffractometer (neutron-scattering instrument at ISIS)
TBD	T o B e D etermined
T0, T ₀	Initiation time for the neutron pulse from the moderator
T ₀ Chopper	Neutron mechanical device to eliminate prompt-pulse, high-energy neutrons
TDS	T hermal D iffuse S cattering
WBS	W ork B reakdown S tructure

1. SING PROJECT OVERVIEW

1.1 DESIRED OUTCOME AND REQUIREMENTS DEFINITION

1.1.1 Background

The mission of the U.S. Department of Energy (DOE) Office of Science (SC) is “To advance basic research and the instruments of science that are the foundations for DOE’s applied missions, a base for U.S. technology innovation, and a source for remarkable insights into our physical and biological world and the nature of matter and energy.” Within SC, the Basic Energy Sciences (BES) program’s responsibilities include planning, constructing, and operating major scientific user facilities to serve researchers from universities, federal laboratories, and industry.

The purpose of the Spallation Neutron Source (SNS) project is to provide a next-generation short-pulse spallation neutron source for neutron scattering and related research in broad areas of the physical, chemical, materials, and biological sciences. SNS will be a national facility with an open user policy attractive to scientists from universities, industries, and federal laboratories. It is anticipated that the facility, when fully operational, will be used by 1,000 to 2,000 scientists and engineers each year and that it will meet the national need for neutron science capabilities well into the 21st Century. The SNS construction project includes an initial suite of five neutron-scattering instruments, and more instruments will be added by various means (including both DOE-BES and non-DOE funding) over time to reach the ultimate capacity of the SNS target station—24 instruments in all. The SNS construction project is on schedule for completion by June 2006.

The scientific justification and need for a new neutron source and instrumentation in the United States have been established by numerous studies by the scientific community since the 1970s. Neutron scattering enables determination of the positions and motions of atoms in materials, and it has become an increasingly indispensable scientific tool. Over the past decade, it has made invaluable contributions to the understanding and development of many classes of new materials, from high-temperature superconductors to fullerenes, a new form of carbon. The information that neutron scattering provides has wide impacts. For example, chemical companies use neutrons to make better fibers, plastics, and catalysts; drug companies use neutrons to design drugs with higher potency and fewer side effects; and automobile manufacturers use the penetrating power of neutrons to understand how to cast and forge gears and brake discs in order to make cars run better and more safely. Furthermore, research on magnetism using neutrons has led to higher strength magnets for more efficient electric generators and motors and to better magnetic materials for magnetic recording tapes and computer hard drives.

1.1.2 Summary Project Description

The technical objective of the SNS Instruments–Next Generation (SING) project is to design, build, and install at SNS a suite of five best-in-class neutron instruments that complement the initial five SNS instruments included in the SNS construction project and to support the identified neutron-scattering needs of the U.S. research community. As the science programs advance and new technological challenges appear, instrumentation needs to be developed and be ready to conquer these new opportunities. Future SNS instrument concepts are being developed in close consultation with the scientific community through a series of workshops, conferences, and focused review and advisory committees. In particular, the five SING project instruments have been identified as meeting the most urgent needs of the scientific community in supplementing the capabilities of the initial SNS instrument suite in the near-term [reference: Report of the October 2002 Meeting of the SNS Experimental Facilities Advisory Committee (EFAC), SNS-110040000-AC0004-R00]. In keeping with the guidelines for Project Management for the Acquisition of Capital Assets (DOE M 413.3-1), these instruments are grouped as a set of deliverables under a single project work breakdown structure (WBS).

1.1.3 SING Project Scope

The five instruments and their capabilities, as recommended by the SNS EFAC, are described in the following.

1.1.3.1 High-Pressure Diffractometer (SNAP)

The high-pressure diffractometer (SNAP) is a specialized diffractometer dedicated to advancing the frontier of high-pressure neutron science. Capitalizing on recent developments in materials under pressure, this unique instrument will use the high neutron flux of SNS, together with state-of-the-art high-pressure devices. This capability will extend the current pressure range of neutron studies well beyond present limits (tens of gigapascals or GPa) and make entirely new classes of experiments possible. Material behavior spanning many orders of magnitude will be examined for the first time into the megabar range (>100 GPa) with unprecedented resolution, accuracy, and sensitivity at all conditions. With the dramatic advances in techniques for preparing and investigating single crystals, studies of more complex materials have become tractable. This instrument will expand the boundaries of high-pressure science in the United States and set a new standard for the world community.

1.1.3.2 High-Resolution Chopper Spectrometer (SEQUOIA)

The high-resolution chopper spectrometer (SEQUOIA) is a direct geometry time-of-flight chopper spectrometer with fine energy (E) and wave-vector (Q) resolution. It will be used to conduct forefront research on dynamical processes in materials. In particular, it will enable unprecedented high-resolution inelastic neutron-scattering studies of magnetic excitations and fluctuations and lattice vibrations. The impact on condensed matter and materials science will span a wide cross section of important research areas, including strongly correlated electrons systems, high-temperature superconductors, colossal magnetoresistive materials, quantum and molecular magnetism, itinerant magnets and multilayers, alloys, ferroelectric, piezoelectric and thermoelectric materials, and soft condensed matter. This spectrometer is a necessary complement to the wide-angle chopper spectrometer.

1.1.3.3 Single-Crystal Diffractometer (SCD)

The single-crystal diffractometer (SCD) will be optimized for the rapid measurement of Bragg intensities on materials with moderate-sized unit cells (up to about 50 Å). A major objective is to study small 0.1-mm³ samples, approaching the size that is routinely used in a broad range of laboratories for single-crystal X-ray studies. To maximize the scientific impact, the instrument design will include the capabilities for magnetic scattering experiments (using polarized neutron beams) and for diffuse scattering measurements. By greatly expanding the range of materials that can be explored, this instrument will revolutionize single-crystal neutron diffraction as we know it, especially from the viewpoint of the practicing synthetic chemist. In addition to chemistry, great advances are also expected in studying critical structural problems in biology, earth science, materials science and engineering, and solid-state physics.

1.1.3.4 Disordered Materials Diffractometer (NOMAD)

The disordered materials diffractometer (NOMAD) is a diffractometer for the investigation of systems with no long-range order, where interatomic and intermolecular interactions can be probed only through detailed investigation of short-range order. The ability to synthesize and use novel nanoscale systems, including crystalline materials, can be enhanced through accurate determination of structural features of materials from interatomic to nanometer length scales. The structural characterization of new materials

provides critical feedback for further improvements in synthesis and for tuning of desired properties. The disordered materials diffractometer is designed to effectively and efficiently use the high flux at SNS to conduct studies of atomic-level and nanoscale structure. These studies will provide the basis for continuing advances in understanding and exploiting the fundamental interactions that control the properties of materials.

1.1.3.5 Hybrid Polarized Beam Spectrometer (HYSPEC)

The hybrid polarized beam spectrometer (HYSPEC) is a direct geometry, hybrid time-of-flight spectrometer that uses a crystal monochromator for beam focusing and polarization and a neutron chopper for fine energy resolution. It will be used to conduct forefront research on dynamical processes in materials. In particular, it is optimized for polarized neutron studies of dynamics in small single-crystal samples at energies ranging from cold to thermal. These capabilities will enable this instrument to carry out unique world-class studies of magnetic excitations in materials of current interest. Although this instrument is optimized for such magnetic studies, it also provides excellent capabilities for other single-crystal dynamical studies. This spectrometer provides capabilities that complement those of SEQUOIA (see Sect. 1.1.1.2) and of the SNS wide-angle chopper spectrometer (ARCS).

1.1.4 Performance Parameters Required to Obtain the Desired Outcome

Each instrument must satisfy the following requirements:

- Fill a scientific need identified by the community, as demonstrated by strong support from a sizeable group of potential users.
- Perform significantly better than any other instrument intended for its class of science—in other words, be “best in class.”
- Be compatible with the characteristics of the SNS facility, including safety conditions, source performance, and physical constraints imposed by other instruments and the existing physical plant.

Compatibility with the SNS facility characteristics will be assessed for each instrument by the SNS organization. All other selection criteria will be judged for each instrument by a peer review process or processes to ensure that the proposed instrument is appropriate and makes the best use of an SNS beam line from a scientific perspective.

1.1.5 Critical Decision 0 Approval

Critical Decision 0 (CD-0) for the “Five Spallation Neutron Source Instruments as Major Items of Equipment” project was approved on May 14, 2003, by Dr. Raymond Orbach, director of the Office of Science. The project was subsequently retitled the “Spallation Neutron Source Instruments—Next Generation,” although the mission and scope have remained the same. The mission need statement encompassed the five neutron-scattering instruments, described previously, to be installed at the SNS facility after its completion. Although the mission need statement envisioned that the five instruments would be managed as individual projects, the Office of Basic Energy Sciences subsequently decided to consolidate the five instruments as Level 2 WBS elements under one major item of equipment (MIE) project organization at Oak Ridge National Laboratory (ORNL). This arrangement will provide much better technical and managerial integration with the SNS facility. Thus, there have been no material changes to the project’s mission, scope, or cost range since CD-0 was approved.

1.2 CONCEPTUAL DESIGNS FOR THE FIVE INSTRUMENTS

Sections 2 through 6 of this document present conceptual designs for each of the five SING instruments, one section per instrument. Each section also includes analyses of design alternatives, including choice of moderator, physics design of neutron guide systems, choice and location of neutron choppers, and detector coverage and performance requirements. Quantitative assessments of the expected performance of each instrument are also included.

2. HIGH-PRESSURE DIFFRACTOMETER (SNAP)

2.1 SNAP INSTRUMENT OVERVIEW

2.1.1 Introduction

The initial instrument concept for SNAP was first presented to the SNS EFAC in March 2001. Subsequently, it was recommended that SNS move forward with more detailed engineering design and construction of the instrument. The following is a brief overview of the instrument that highlights some aspects of its conceptual design; the overall design is subject to technical review and change.

2.1.2 Instrument Summary

SNAP will be a high-flux, medium-resolution diffractometer designed primarily for the study of very small samples under extreme conditions of pressure and temperature. One goal of this instrument is to maintain resolution requirements for crystallographic studies of powdered and single-crystal samples and to increase the pressure range routinely achieved by at least a factor of five over that currently attained at the world's best neutron sources, that is, from the current pressure maximum of 20 GPa to >100 GPa. The increased flux at SNS, coupled with new and highly efficient microdetector technology and neutron focusing devices, will likely enable a significant increase in the on-sample neutron flux, thus leading to diffraction from significantly smaller samples and at significantly higher pressures. It can easily be argued that such an instrument will open many new avenues of research that span many interdisciplinary fields, including condensed matter physics, geosciences, interplanetary sciences, and biosciences.

The goal of the design effort is to produce a highly compact instrument that is optimized around a neutron-scattering, high-pressure device (i.e., highly integrated incident beam optics, pressure cell, and detector array). The primary consideration for increasing the on-sample neutron flux is a short incident flight path. A highly compact instrument with a secondary flight path of only 0.37 m can be constructed with an incident flight path as short as 15 m and still maintain sufficient instrumental resolution. With such a short secondary flight path, the detector banks must have high positional resolution (i.e., a pixel size of 1.5 mm² matches with sample size and with the moderator view). One of the initial workhorse high-pressure devices will likely be based on the new open cylinder (panoramic) opposed gem anvil design, which allows for exceptionally large area detector coverage while still providing excellent anvil stability. Such a design significantly minimizes the amount of material through which the incident and scattered neutrons must penetrate. Workable samples will likely range in size from ~ 1 mm³ for studies at the highest pressure, to ~ 100 mm³ for work at more moderate pressures but where sample scattering is weak. Anvil sets could range from large single-crystal synthetic diamonds for the highest pressures (>100 GPa), to single-crystal moissanite or sapphire anvils for intermediate pressure ranges (1–50 GPa), to tungsten carbide Bridgman type (or toroidal) anvils for the lower pressure ranges (1–25 GPa). With the current design of gem anvil panoramic cells, a maximum of 6.5 steradians of detector coverage may be possible, thus allowing study of single-crystal samples.

The instrument will likely view the top upstream, poisoned decoupled hydrogen moderator, which is currently preferred (over the ambient water moderator) for its increased neutron flux at wavelengths greater than 2 Å and for its shorter pulse width over the entire bandwidth of the first frame (i.e., between 0 and 4 Å). Included will be two (possibly three) bandwidth choppers, thus significantly reducing the background and extending the operational bandwidth into the second frame, thereby providing d-spacing coverage from 0.212 Å < d < 5.94 Å at 2θ = 90°. To significantly reduce the background levels from the prompt neutrons, a T₀ chopper operating at 60 Hz and placed ~7 m from the moderator will likely be required. Also important for background reduction is a well-defined collimated neutron beam. Because of slight changes in sample position during pressure loadings, it is anticipated that the position of the sample should be adjustable; therefore, the press should be small enough to allow precise positioning after each pressure loading. A set of continuously adjustable variable apertures will allow for significant flexibility

of the beam shape, which may also be essential during the sample alignment process. These design features, along with resolution function calculations and Monte Carlo simulations, are discussed in the following sections.

2.2 SNAP INSTRUMENT DETAILS

2.2.1 General Orientation

The geometry of SNAP will be completely dominated by the design of the high-pressure device. Recently, an open cylinder gem anvil cell (or panoramic cell), based on the mega-bar type cell, has been produced and tested. This large sample volume cell may be readily adapted for neutron scattering. A stylized drawing of this cell, with detectors but without a press, is shown in Fig. 2.1. Figure 2.2 shows a schematic of the cell, possible detector locations, and incident beam collimation as viewed from the top (without a press assembly). In Fig. 2.1, one of the detector sections is not shown to illustrate the anvil assembly.

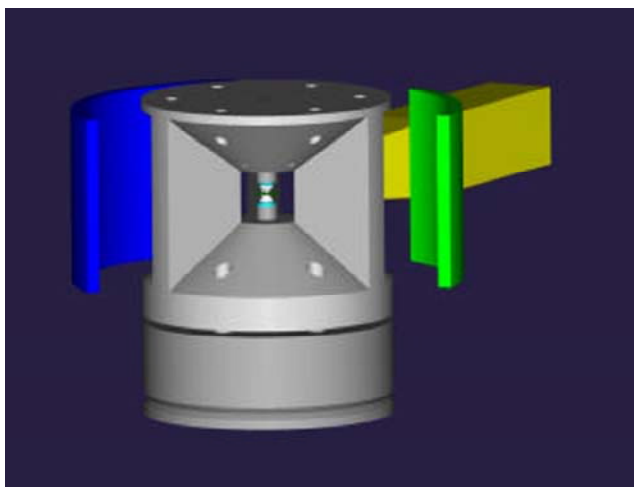


Fig. 2.1. Stylized drawing of the high-pressure cell with incident beam collimation (or focusing optic) and detector location. The press is not included.

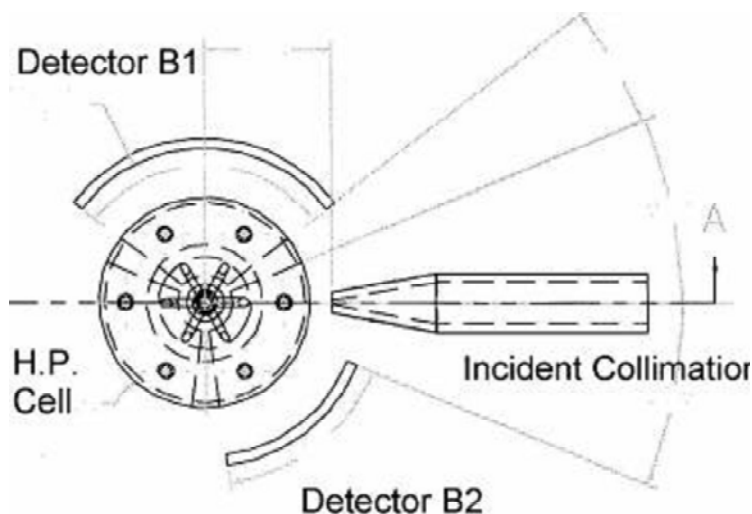


Fig. 2.2. Top view of the high-pressure cell as shown in Fig. 2.1. Incident beam collimation and the detector loci of two banks are shown.

For maximum detector coverage, there are three symmetrically spaced “open” sections of the prototype panoramic cell. Each “open” section measures 105° in the equatorial plane (2θ) and 68° in the longitudinal plane. This geometry helps minimize the amount of material the incident beam must penetrate to reach the sample and maximizes the amount of possible detector coverage. (With such a cell design, up to 6.5 steradians of solid angle may be covered with detectors.) The optimum pixel size, and consequently count rate, is determined by a solid angle subtended by a representative 1-mm^3 sample and the solid angle subtended by the $9.7\text{-} \times 12\text{-cm}$ projected view of the moderator. Given the constraints placed by the cylinder dimensions and the minimum detector pixel size (1.5 mm^2) available with current technology, the optimum secondary flight path was determined to be 0.37 m, which allows for a 15-m incident flight path when fitted next to neighboring instruments. Using this geometry, a large area detector may range continuously from $2\theta = 37.5^\circ$ to 142.5° for a bank centered on $2\theta = 90^\circ$, as shown in the figure. One viable detector design option has been developed at Brookhaven National Laboratory (BNL), and an example is discussed subsequently in Section 2.3.

2.2.2 The Press

Compression of large volume samples ($1\text{--}2\text{ mm}^3$) to generate the target pressures of $>100\text{ GPa}$ will require hydraulic presses with clamping forces on the order of $\sim 400\text{--}500$ tonnes. Although the clamping force is high, such a press need not be large and might weigh only several hundred kilograms, thus making integration with the detector array feasible. In fact, a 400-tonne version of the more common 200-tonne Paris-Edinburgh (P-E) press already exists and has total dimensions of $\sim 400 \times 600\text{ mm}$. The novel aspect of this press design is the ability to pretighten the breech bolt, located at the top of the cell, during the initial sample loading process, resulting in a very short stroke of the piston upon pressurization (only 2–3 mm). It is envisioned that the press and anvil assembly could be lifted in and out of the scattering chamber for easy sample loading.

It is proposed that one option for the press design for the SNAP instrument be a variant of the P-E design with three tie-rods aligned appropriately with the three web sections of the panoramic cell. An illustration of such a three-post press is shown in Fig. 2.3.

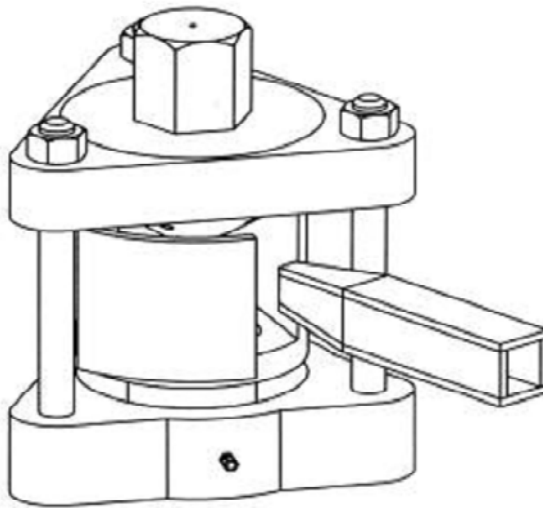


Fig. 2.3. Line drawing of the three web open-cylinder panoramic device in a three-post press, based on the P-E design. Incident beam collimation elements are shown, along with the position of one detector.

Another option would be to incorporate a version of a frame press shown in Fig. 2.4. This has the advantage of (1) providing load uniformity throughout the frame and (2) a very *open* geometry that could allow for even greater detector coverage. Note that such a press may also incorporate a panoramic cell with only two webs rather than three (as shown previously), thus further increasing the maximum solid angle available for detector coverage.

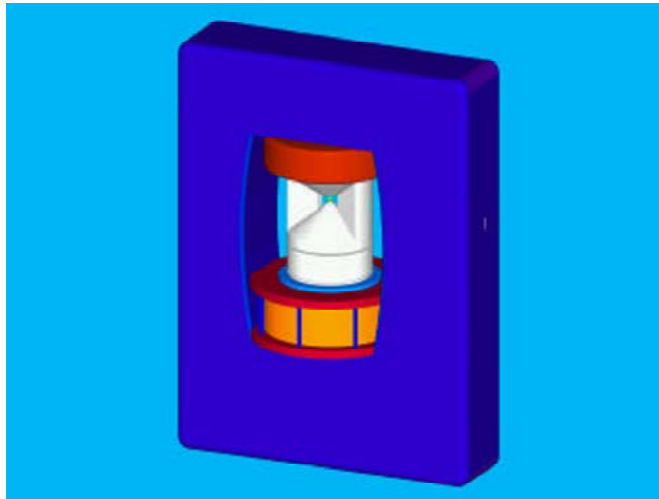


Fig. 2.4. Drawing of the frame press design with a hydraulic pancake-style cylinder on the bottom of the opening and a panoramic-type pressure cell.

2.2.3 Bandwidth (Disk) Choppers

With a total flight path of 15.37 m and with SNS source running at 60 Hz, frame overlap occurs at ~ 4.1 Å. To reduce background generated by longer wavelength neutrons and to significantly extend the

bandwidth into the second frame, a set of disk choppers will likely be required. A set of two choppers can be placed at 6 and 11 m from the moderator. As illustrated in the timing diagram in Fig. 2.5, such a system operating in the first frame results in longer wavelength neutron *bleed-through* occurring at $\lambda \sim 15$ Å. For operation in the second frame, longer wavelength neutron *bleed-through* occurs at $\lambda \sim 18.5$ Å. Note that at $\lambda = 15$ Å the poisoned decoupled hydrogen moderator flux is reduced by almost three orders of magnitude from that at $\lambda = 2.5$ Å, the peak position in the moderator profile. To further reduce the background created by long wavelength neutrons, the option of using a three chopper system has also been investigated. With an additional disk chopper placed at 8 m from the moderator, longer wavelength neutron *bleed-through* occurs at $\lambda = 26$ Å.

Operating in the first frame ($\lambda \leq 4.1$ Å) at a scattering angle of $2\theta = 90^\circ$ provides d-space coverage of $d \leq 3.0$ Å. This is extended when operating in the second frame to $d = 5.8$ Å. The largest length scales probed with this instrument by detectors at 90° is ~ 1.5 times higher than that of the HiPr beam line at ISIS. The d-space coverage in the first and second frame as a function of scattering angle 2θ is given in Fig. 2.6.

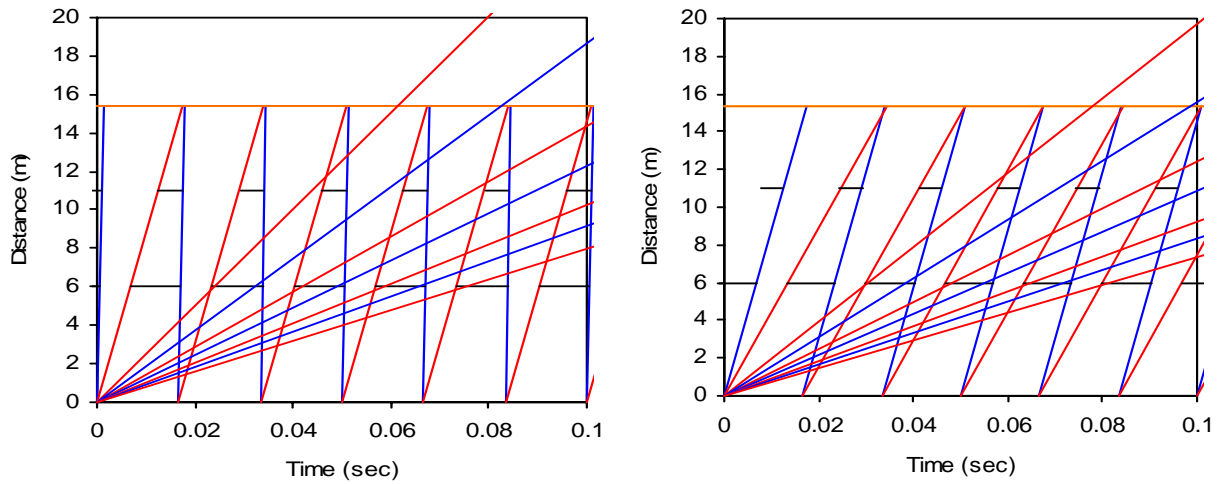


Fig. 2.5. Timing diagrams for a two-chopper system operating in the first frame (left plot) and second frame (right plot).

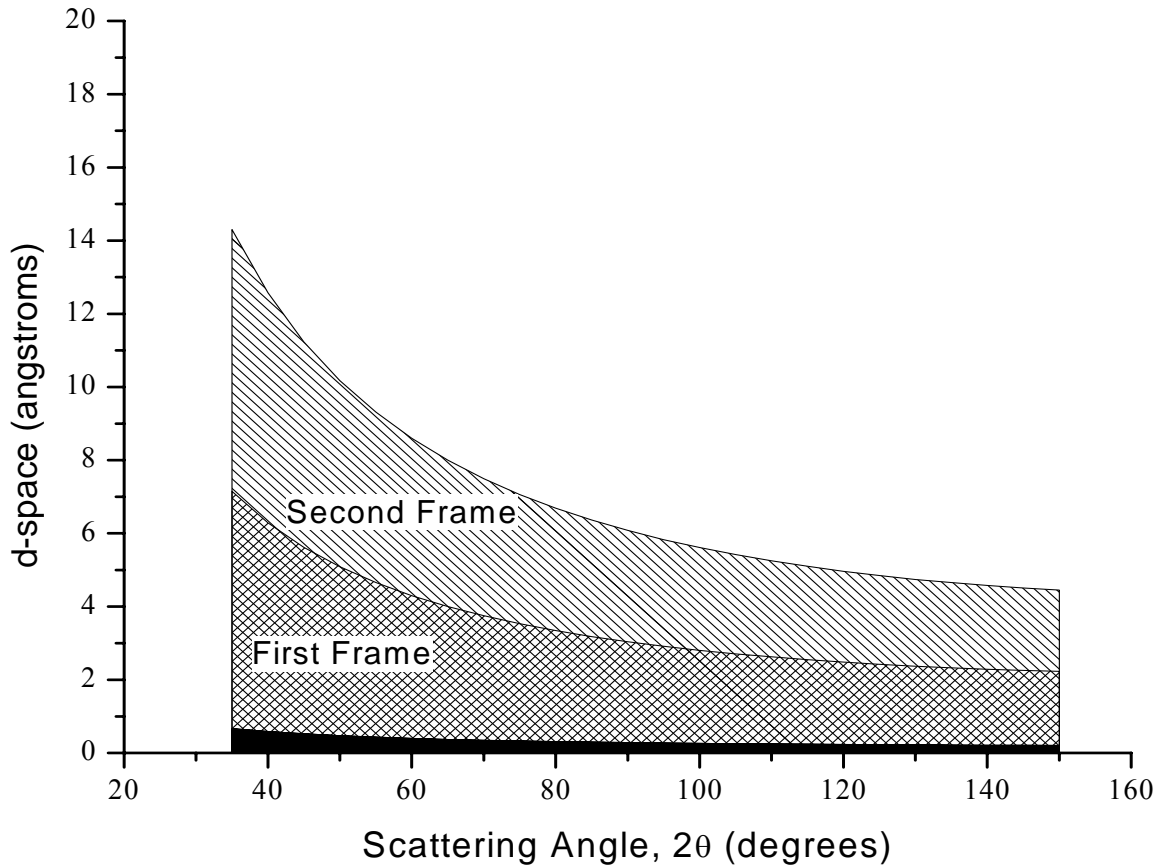


Fig. 2.6. d-spacing range versus scattering angle.

2.2.4 T_0 Chopper

Another significant source of background radiation is the highly energetic prompt pulse neutrons that travel along the beam tube and into the scattering chamber. Although the detectors are not very sensitive to such neutrons, the neutrons could moderate in the shielding material and scatter from the massive metal structure of the press assembly, thus raising background levels. In addition, neutron-focusing devices will likely be placed upstream of the sample position. These devices are almost completely transparent to very high-energy neutrons. Consequently, not only is alignment of the optical device difficult but also the unfocussed high-energy neutrons would illuminate large volumes of the gasket, anvils, and press, thus creating additional background scattering. This instrument will therefore require a means to remove the high-energy neutrons from the incident beam. Design parameters for a T_0 chopper with rotation axis parallel to the neutron beam are given subsequently. Schematic representations of the instrument geometry used in the calculations of the T_0 chopper parameters are shown in Fig. 2.7.

The moderator to sample distance (d_{MS}) and sample dimensions are defined as 15 m and 1 mm^3 , respectively. The moderator to chopper distance (d_{MC}) is 7 m. The dimensions of the apertures placed at $d_{MA1} = 1 \text{ m}$ and $d_{MA2} = 7.6 \text{ m}$ are defined by the projected view of the moderator and the sample size and are used to define the chopper blade dimensions. The relative beam penumbra geometry is illustrated in the lower diagram. The chopper frequency is set to 60 Hz. The distance from the axis of rotation of the chopper to the center of the neutron beam was taken to be 0.25 m, and the axis of rotation of the chopper blade is parallel to the beam axis.

Given the preceding geometrical requirements, and the minimum wavelength required to pass unobstructed ($\lambda = 0.4 \text{ \AA}$), the following chopper parameters have been calculated:

- Maximum blade arc length: 15.3°
- Maximum inner blade radius: 0.227 m
- Maximum outer blade radius: 0.273 m
- Time required to fully close the beam: 359.44 \mu s
- Time after T_0 that the chopper begins to open: 347 \mu s
- Maximum wavelength that passes unobstructed: 9.19 \AA (just beyond second frame)
- Minimum wavelength contamination in beam penumbra: 0.2 \AA

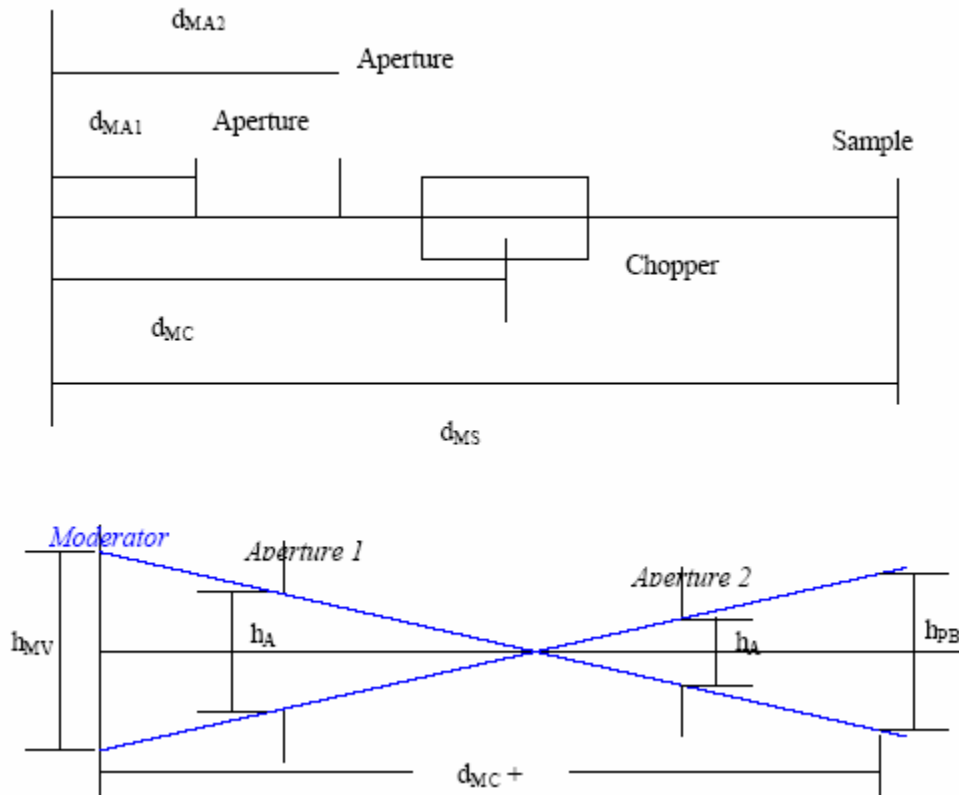


Fig. 2.7. Geometry used to calculate the T_0 chopper parameters.

2.2.5 Moderator Choice

The current SNS design provides three cryogenic hydrogen moderators and one ambient temperature water moderator. Because of the very small sample size and surrounding gasket material, it is essential that this instrument be located on a beam line with high neutron flux between 0.5 and 4.1 \AA while maintaining a resolution of at least $\Delta d/d = 0.8\%$. Figure 2.8 (left) illustrates the timing resolution for the coupled and the decoupled hydrogen and ambient water moderators. The timing resolution (FWHM as a function of wavelength) of the coupled hydrogen moderator is sufficiently large that it would be impractical for this diffractometer, particularly at high scattering angles, and thus it is not considered further. Figure 2.8 (right) compares the neutron flux as a function of wavelength at the moderator face for the ambient water moderator and the poisoned decoupled hydrogen moderator. The decoupled poisoned

hydrogen moderator provides superior neutron flux performance above ~ 2 Å. (Recall that the instrument is designed such that frame overlap occurs at ~ 4.1 Å; therefore, for the portion of the first frame with λ above ~ 2 Å, the hydrogen moderator will give superior flux and resolution performance, and during operation in the second frame the hydrogen moderator will provide slightly poorer resolution but far greater neutron flux.)

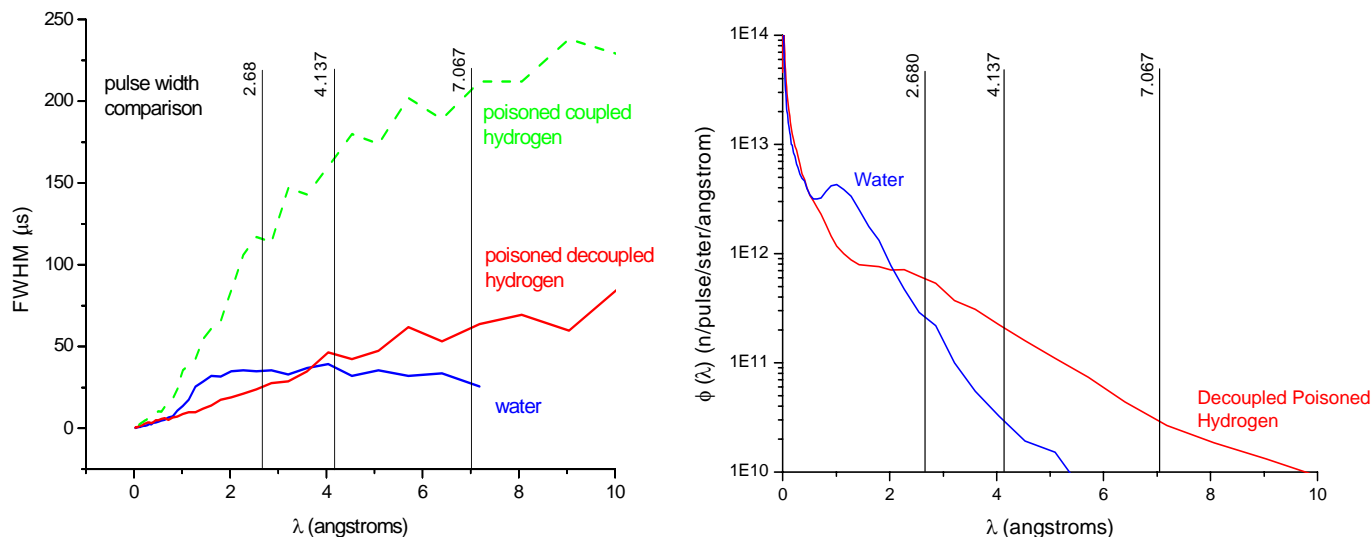


Fig. 2.8. Pulse timing (FWHM) and flux profiles from various moderators as functions of wavelength.

As an illustration of which moderator provides optimal performance, a Monte Carlo computer simulation program has been written to simulate diffraction peaks at various d-spacing. This code incorporates the neutron flux and FWHM timing parameters as a function of wavelength for both the water and poisoned decoupled hydrogen moderators. Several peaks of a powdered structure II clathrate hydrate (cubic unit cell, $a = 17.3$ Å, space group Fd3m) have been chosen to illustrate the relative resolutions and peak intensities at various wavelengths. The simulation has been performed at $2\theta = 90^\circ$, and the peaks have been chosen such that they are generated by neutrons with wavelengths (1) in the first frame, $\lambda = 2.680$ Å, d-space = 1.900 Å, i.e., the [753] clathrate peak; (2) at the boundary between the first and second frame $\lambda = 4.137$ Å, d-space = 2.926 Å, i.e., the [531] clathrate peak; and (3) well into the second frame $\lambda = 7.067$ Å, d-space = 4.997 Å, the [222] clathrate peak. These neutron wavelengths are illustrated on the plots in Fig. 2.8 as vertical lines. These simulated peaks are illustrated in Fig. 2.9.

In the case of the two smaller d-spacings, the resolution of the two moderators is found to be comparable; however, at longer wavelengths the resolution from the water is, as expected, superior. The timing contribution to the resolution function for each of these cases has been calculated from the data presented in Fig. 2.8 and is given as (1) for $\lambda = 2.68$ Å, $\Delta t/t = 0.24\%$ for the poisoned decoupled hydrogen moderator and 0.34% for the ambient water moderator; (2) for $\lambda = 4.14$ Å, $\Delta t/t = 0.27\%$ for the poisoned decoupled hydrogen moderator and 0.23% for the ambient water moderator; and (3) for $\lambda = 7.067$ Å, $\Delta t/t = 0.23\%$ for the poisoned decoupled hydrogen moderator and 0.10% for the ambient water moderator. However, the increased flux provided by the poisoned decoupled hydrogen moderator is overwhelming in all three cases. Thus, the top upstream poisoned decoupled moderator is the current choice for SNAP.

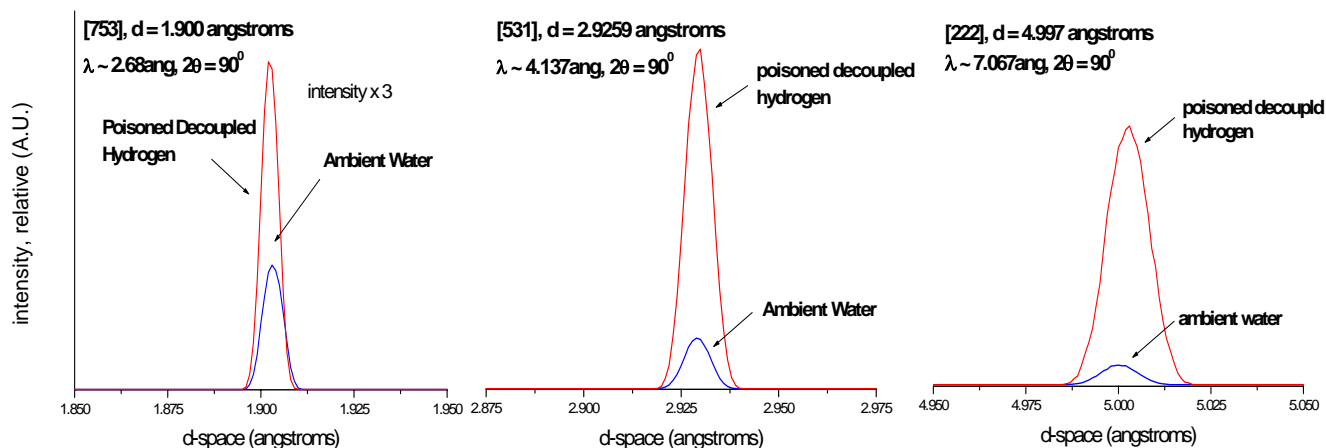


Fig. 2.9. Comparison of simulated data generated from the same sample, in the same scattering geometry, with the water moderator (blue) and with the poisoned decoupled hydrogen moderator (red). Relative intensities are accurate (the intensity of the $d = 1.9 \text{ \AA}$ peak has been multiplied by three).

2.2.6 Focusing Super-Mirror Reflectors (Series of Supermirror Funnel)

The use of a neutron-focusing device coupled with high-pressure cells could prove to be particularly useful for increasing the on-sample neutron flux. Although significant flux gain can be readily achieved with modern neutron-focusing devices, it is highly desirable that the beam be focused onto a very small focal spot so as to minimize the neutron illumination of the surrounding gasket and anvil assembly. In addition, the device must be capable of a very tight focus without significantly increasing the on-sample divergence and thus degrading the instrument resolution function. One way to increase the neutron flux on a very small sample, while minimizing the increase in beam divergence, is to use a long series of square supermirror funnels and to *collimate out* the highly divergent neutrons before they enter the focusing system. Such a device has been simulated, and the results are given subsequently. It should be noted, however, that such a device is presented only as an illustration of a possible scheme that might meet the design requirements and that neutron optical design for SNAP is a very active area of investigation.

Many neutrons can travel along the beam tube but outside the beam umbra, which is the envelope defined by the sample dimensions and the viewed moderator surface. These neutrons are often a significant source of background and are usually either absorbed by the shielding material or scattered out of the incident beam as far upstream of the sample position as possible. Many of these neutrons can, however, be reflected onto the sample by using a long series of square supermirror funnels oriented to form a set of so-called *focusing anti-trumpets*. The system is illustrated in the schematic diagram of Fig. 2.10; note that only a cross section is shown in this figure. The line between the edges of the viewed moderator surface and the edges of the sample defines the envelope of the beam umbra. Neutrons within the beam umbra are not reflected by the focusing device. A collimator is placed upstream of the supermirror funnels to define a highly collimated incident neutron beam that is outside of the umbra. Neutrons that are traveling within the beam umbra do not travel through the collimators before hitting the sample. As such, the collimator system defines a *frame* that is open in the middle. The view down the beam showing the position of the collimators is also presented in Fig. 2.10.

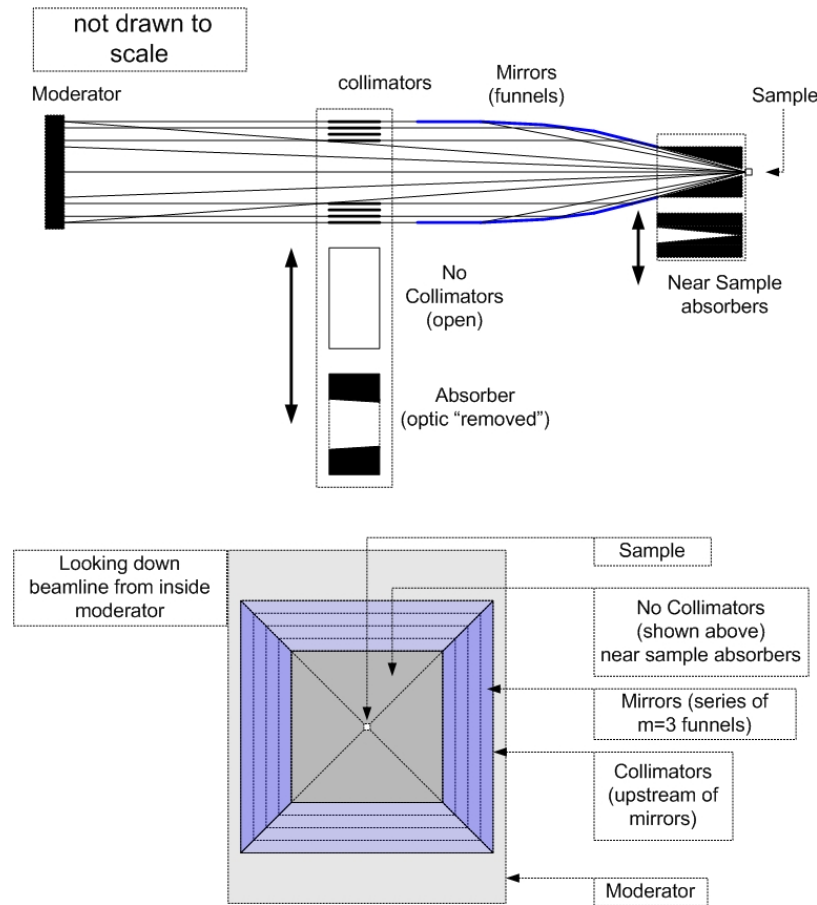


Fig. 2.10. Representation of a focusing system for very small samples.

In the present simulation, the focusing system was made up of 13 slightly tapered rectangular supermirror funnel sections ($m = 3$), with lengths ranging from 0.3 to 0.5 m, with an entrance size of 9.7×9.7 cm. Each successive section has a slightly higher taper angle. The taper angle of the entrance section is chosen so that neutrons passing through the collimator with wavelengths greater than 0.5 \AA are reflected once and are directed toward the focal point, defined by the taper angle to be a 3×3 -mm spot at 15 m from the moderator surface. Likewise, the taper angle and length of each subsequent section is chosen so that the incident neutrons are reflected only once and are directed toward the same focal point with dimensions of 3×3 mm, as shown in the figure. The collimators can also be removed, leaving a series of focusing funnels. (It should be noted, however, that with no collimators in place, highly divergent longer wavelength neutrons would be reflected, resulting in a significant defocusing effect.) Conversely, a neutron absorber can be put in place of the collimators, resulting in the effective “removal” of the focusing device.

Monte Carlo (MC) simulations showing the focal plane with and without the mirror sections in place are illustrated in Fig. 2.11. Note that *only reflected* neutrons are included in this simulation and that the grey scale intensities are different in each plot. The neutron gain factor given by the mirror system at the sample position is plotted in Fig. 2.12. Notice that significant gain is realized starting at $\lambda = 0.5 \text{ \AA}$, and for neutrons with $\lambda = 1 \text{ \AA}$, the gain is nearly a factor of 8 and reaches a maximum value of 8.8 at $\lambda = 2.2 \text{ \AA}$. The resulting effects on the resolution can be found by investigating the simulated neutron intensity at the sample position versus the horizontal/vertical divergence. Because of the highly collimated neutron beam entering the funnel system, the divergence is not highly wavelength dependent. In fact, the maximum divergence is ~ 10 mrad with $\lambda = 0.9 \text{ \AA}$ and does not significantly increase at longer wavelengths. The divergence exiting the system can be tailored by adjusting the divergence of the beam entering the

system. As a result, the simulated diffraction line shape is not significantly affected at longer wavelengths (i.e., there are no observed *winglets* in the peak shape, (see the MC simulations in Fig. 2.13); there is however a slight broadening at the base of the peak.

Given the gain factor as a function of wavelength, the neutron flux on the sample can be calculated. The time-averaged neutron flux (in counts per second) on a sample that is 1 mm³ located at the focal point 15 m from the poisoned decoupled hydrogen moderator is shown in Fig. 2.14.

2.2.7 Resolution Function

An analytical approximation to the instrumental resolution function is given by

$$\frac{\Delta d}{d} \approx \left[\left(\frac{\Delta t}{t} \right)^2 + \left(\frac{\Delta L}{L} \right)^2 + (\Delta \theta \cot \theta)^2 \right]^{\frac{1}{2}}, \quad 2.1$$

for a given sample size, optimized detector pixel size, pulse characteristics, and flight path lengths. This analysis assumes a normal moderator view and that each term acts independently, has a natural instrumental divergence of ~ 4 mrad, and has been used in these calculations.

For wavelengths approximately bracketing the bandwidth of the first frame (i.e., neutron wavelengths between 1.4 and 4.04 Å), the $\Delta d/d$ resolution function has been calculated for detector banks centered on a 37-cm secondary flight path and is shown in Fig. 2.15. By comparison, the HiPr beam line at ISIS has $\Delta d/d \sim 0.008$ at $2\theta = 90^\circ$, which is the resolution obtained at a scattering angle of 63° in the current design.

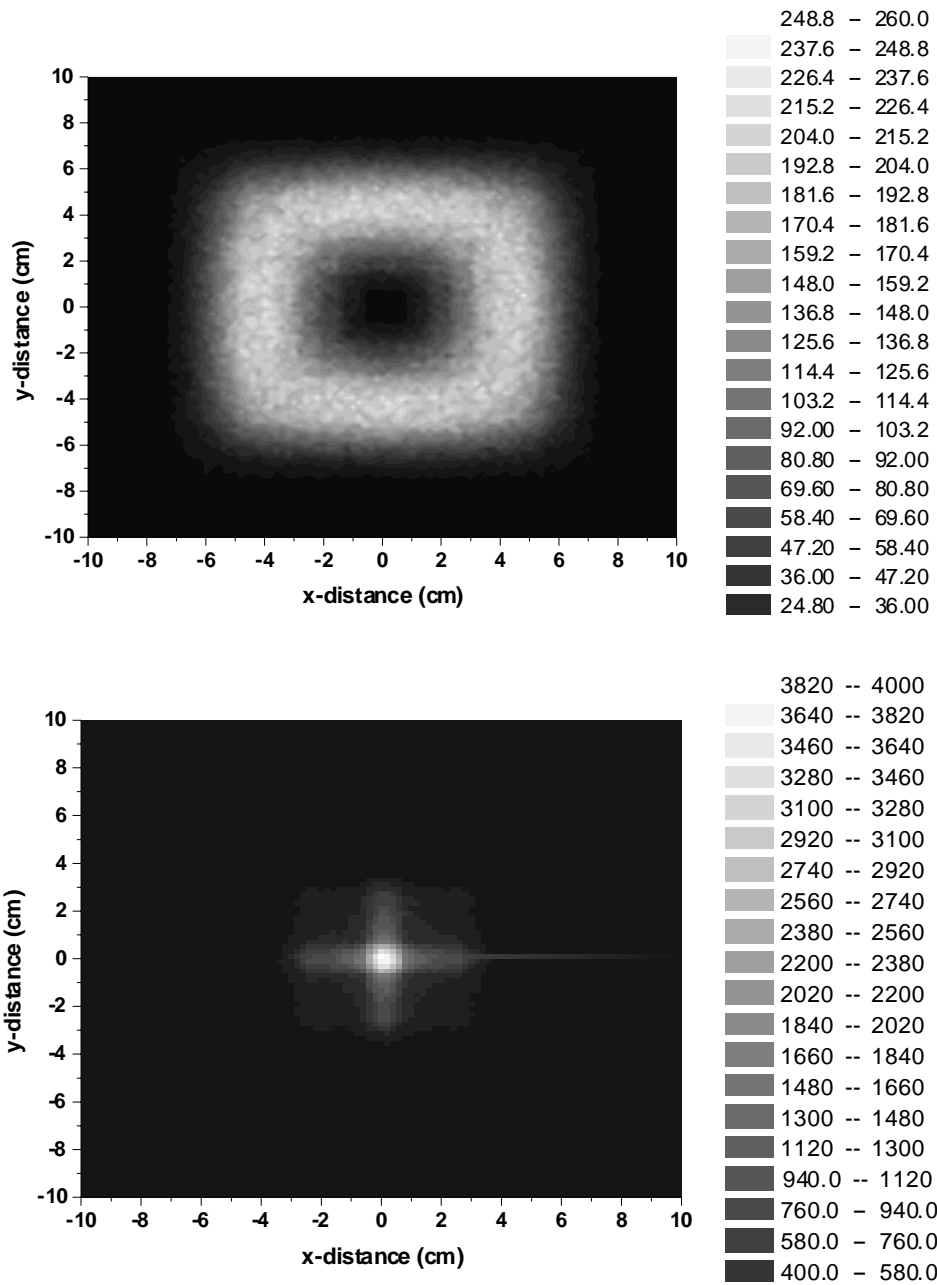


Fig. 2.11. Focusing of neutron beam with a series of rectangular supermirror funnels. The upper panel shows the image without the mirrors in place, and the lower panel shows the image with the mirrors in place. Note: only neutrons that travel through the collimators are simulated.

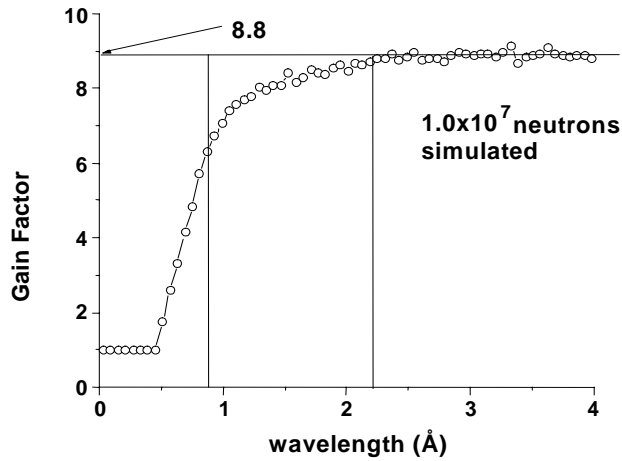


Fig. 2.12. Flux gain calculated with and without the focusing mirrors in place.

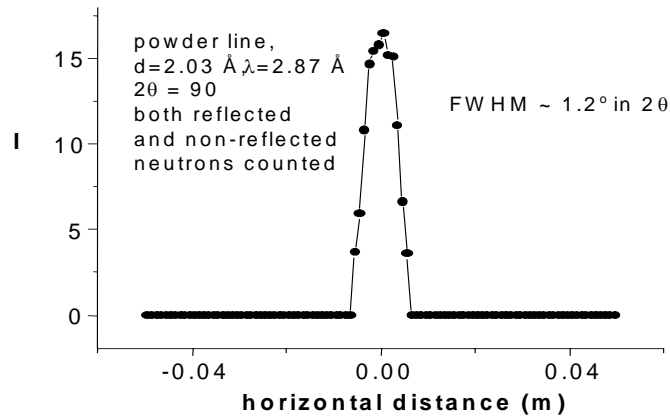


Fig. 2.13. Simulated diffraction peak. Note that as expected the increased divergence created by the focusing device has the effect of slightly increasing the base of the peak. Work continues to reduce the effects of the on-sample divergence.

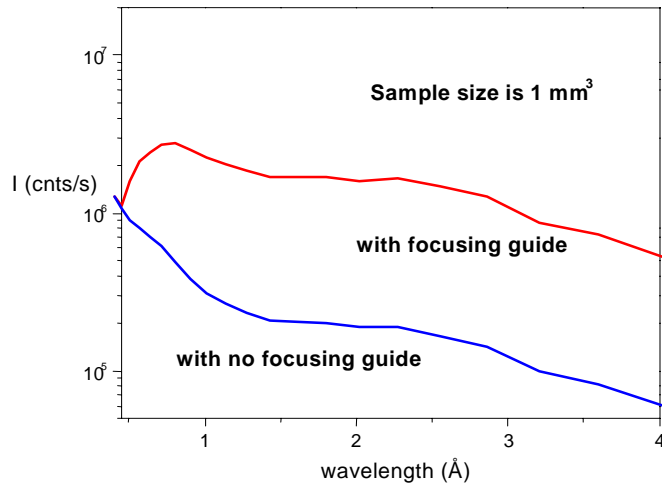


Fig. 2.14. Neutron flux on sample with and without supermirror funnel system in place.

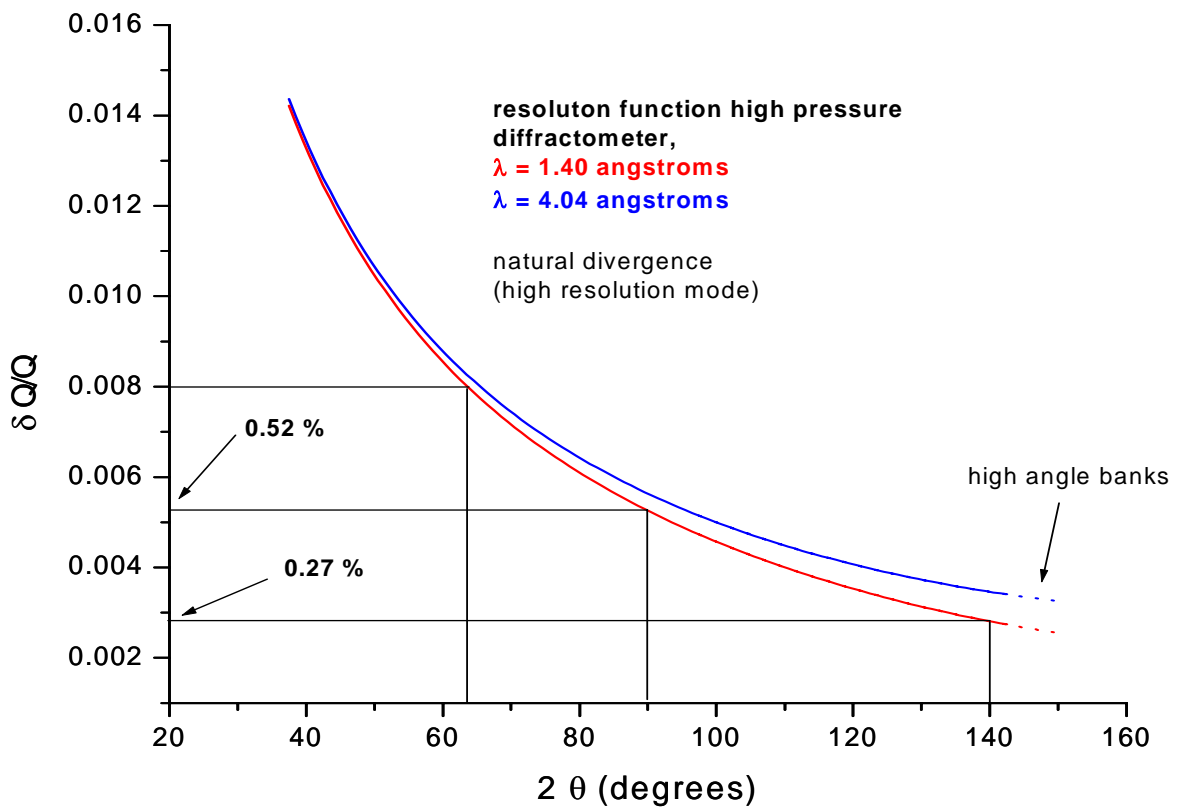


Fig. 2.15. Analytical form of the resolution function for selected wavelengths in the first frame. In the current geometry the high angle banks are shown on the +2 θ side of the instrument.

Beam line 3 views the top upstream poisoned decoupled hydrogen moderator at an angle of 13.75° off the normal. This introduces an asymmetry into the resolution function of the instrument because of to time focusing (i.e., for a given wavelength, the resolution at $+2\theta_i \neq -2\theta_i$). To investigate the magnitude of this effect, an MC simulation program has been written to simulate Bragg peaks at a given d-spacing and at various scattering angles. This information was then used to determine the orientation of the high-pressure cell with respect to the incident beam and to determine the optimal position for the detector banks. Figure 2.16 illustrates two simulated Bragg peaks, both centered on $d = 2.00 \text{ \AA}$ and both with similar resolution—one collected using a detector element placed at $2\theta = -90^\circ$ on the high-resolution side and the other collected using a detector element placed at $2\theta = +150^\circ$ on the low-resolution side. Note that these two peaks are both collected in the first frame.

The simulated resolution function ($\Delta d/d \%$) as a function of d-spacing between 2.0 and 5.5 \AA for a series of detector elements in Bank 1, the high resolution bank, is illustrated in Fig. 2.17. Again, all neutrons start at T_0 .

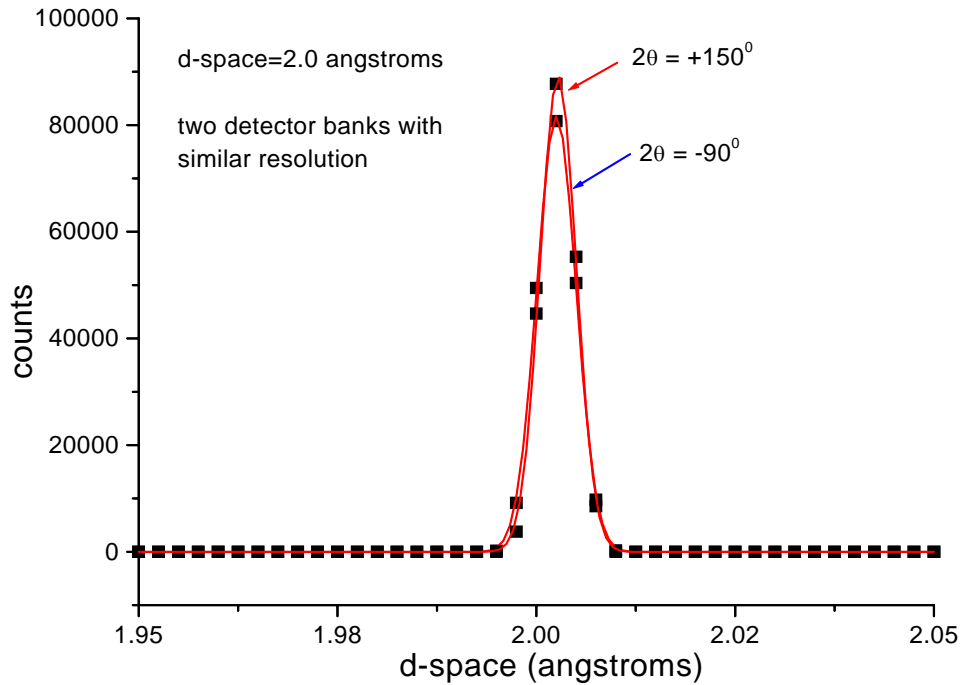


Fig. 2.16. Simulated Bragg peak indicates asymmetry in the resolution function.

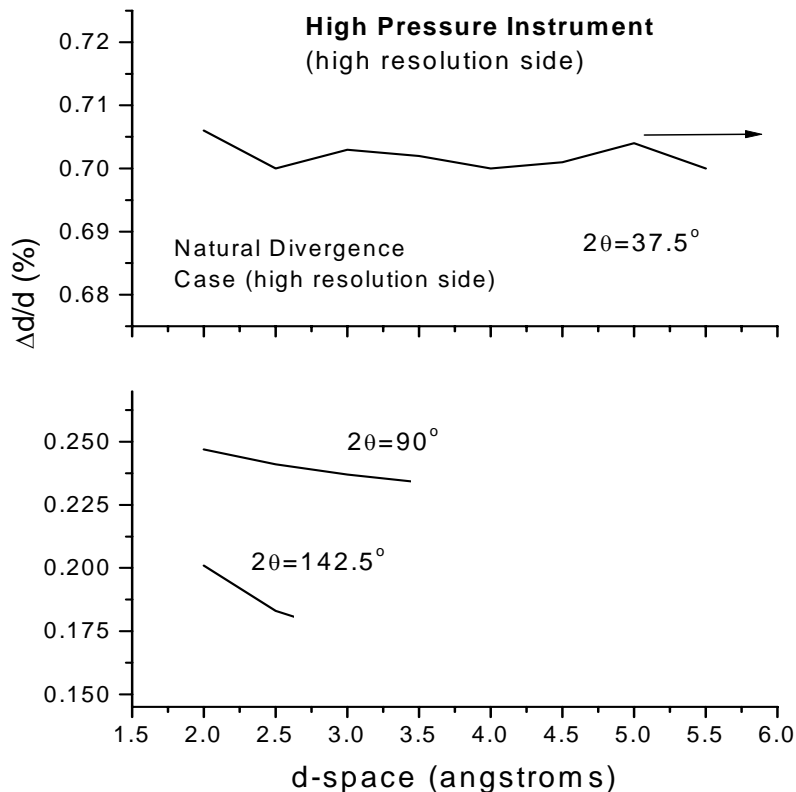


Fig. 2.17. Simulated resolution as a function of d-spacing at various angles in the large high-resolution bank. The range shown indicates the upper limit of the first frame.

2.3 POSITION-SENSITIVE DETECTORS

2.3.1 Introduction

The following is a brief description of a possible detector technology that has been demonstrated to meet the specification for SNAP. It is presented as an option only; of course, other options are being actively pursued.

2.3.2 Key Requirements

- High efficiency in the 1- to 4-Å wavelength range (in the first frame)
- Ultralow sensitivity to γ background
- Position resolution of 1.5-mm FWHM at end of 0.37-m sample-to-detector flight path
- Count rate capability of 10 kHz on a single peak, global rate of order 10^6 s^{-1}
- Timing resolution on the order of $1 \mu\text{s}$
- Stability of absolute position readout (to about $250 \mu\text{m}$)
- SNAP high-pressure cell and detector design integration, two detectors (one oriented vertically, $\pm 34^\circ$ by 30° , one horizontally, $\pm 52.5^\circ$ by 30°) are presented. Note that this is preliminary and is

meant to illustrate the possible level of pressure cell-detector integration. The final design can be modified to better match the solid angle of the final high-pressure cell design.

2.3.3 Choice of Detector Technology

The most effective detector technology for this application is based on ^3He -filled proportional chambers. All of the preceding requirements can be achieved, particularly with respect to the critical characteristics of neutron efficiency and insensitivity to γ background. Figure 2.18 shows the absolute efficiency of a 15-mm gas depth (the gas thickness in standard BNL detectors) with 6 atm of ^3He . The efficiency is 50% at 1 Å and rapidly increases to more than 90% for 4 Å and beyond. Neutron conversion in ^3He results in a substantial primary ionization deposit of about 25,000 electron/ion pairs. This permits virtually full rejection of background events based purely on threshold. It is difficult to achieve such low sensitivity to gamma background with any other detection technology.

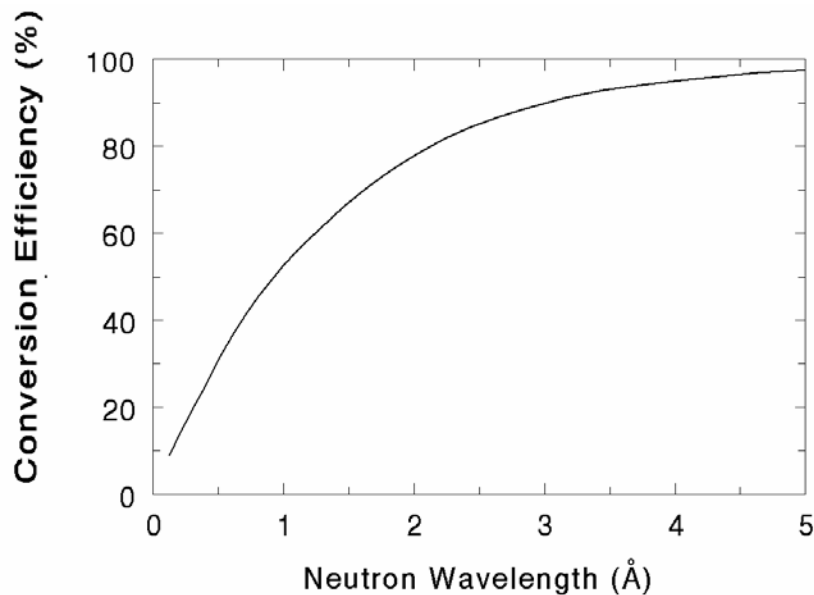


Fig. 2.18. Detection efficiency for thermal neutrons in 15-mm gas depth @ 6 atm ^3He .

PEARL, located at the ISIS neutron user facility in the United Kingdom, is presently one of the foremost high-pressure diffractometers. This instrument uses lithium-doped ZnS scintillators, which are readout with fiber-optic-coded arrays. ^3He -based detectors will fulfill the performance requirements of SNAP significantly better than scintillator technology. For example, while a greater ZnS scintillator thickness increases neutron conversion efficiency, output signal is ultimately diminished because ZnS is absorbing to its own scintillation light. This tradeoff in thickness is not associated with ^3He -based detectors. In addition, the pulse height spectrum of the scintillator output signal is relatively flat, making threshold discrimination between neutrons and gamma background less precise and the neutron detection efficiency more susceptible to drift (less stable) than with ^3He .

2.3.3.1 Proposed Detector Design

At the heart of this detector will be a specially designed curved wire segment of approximately 20×20 cm. This is a “building block” that can be repeated as necessary inside a common gas volume. The

principle of curved wire segments has recently been established. An edge view of one part of such a segment is shown in Fig. 2.19. Accurate position information is obtained from the crossed wire cathodes, each of which are subdivided into nodes, or fiducial points, about 10 mm apart. The nodes are fixed reference locations that help maintain absolute position stability, while resistive charge division between nodes permits encoding with electronic accuracy better than 1 mm. Neutron position resolution is ultimately determined by ranges of the proton and triton, which are the reaction products from neutron conversion. A resolution of 1.5 mm can readily be achieved by use of a quench gas such as propane.



Fig. 2.19. Edge view of curved, wire segment. Curvature eliminates parallax error (in horizontal plane in this example); position readout yields electronic accuracy better than 1 mm.

An outline of detector vessels for the diffractometer is shown in Fig. 2.20. The smaller one on the left, subtending $\pm 34^\circ$ in the vertical plane, contains two curved segments, and the larger one on the right, subtending $\pm 52.5^\circ$ in the horizontal plane, contains three curved segments, thus it can be seen that these detectors can be highly integrated with the high-pressure cell design. Each segment is read out independently by its own encoding electronics, located in the hermetic containers atop each minor flange. Furthermore, the segment design permits them to be positioned adjacent to each other in their common gas volume, providing a seamless position readout at each boundary. This advanced performance is important in the high-pressure application, where a continuous position response is particularly crucial in the equatorial and vertical plane.

2.3.3.2 Recently Fabricated Instrument

This detector has recently been designed and commissioned for protein crystallography at the Los Alamos Neutron Science Center (LANSCE). This is a curved detector that successfully encapsulates the general requirements outlined in Section 2.3.2 and the principles described in Section 2.3.3. The

completed instrument is shown in Fig. 2.21, on a goniometer of a protein crystallography station at LANSCE. This detector is an eight-segment wire chamber with a radius of curvature of 0.7 m.

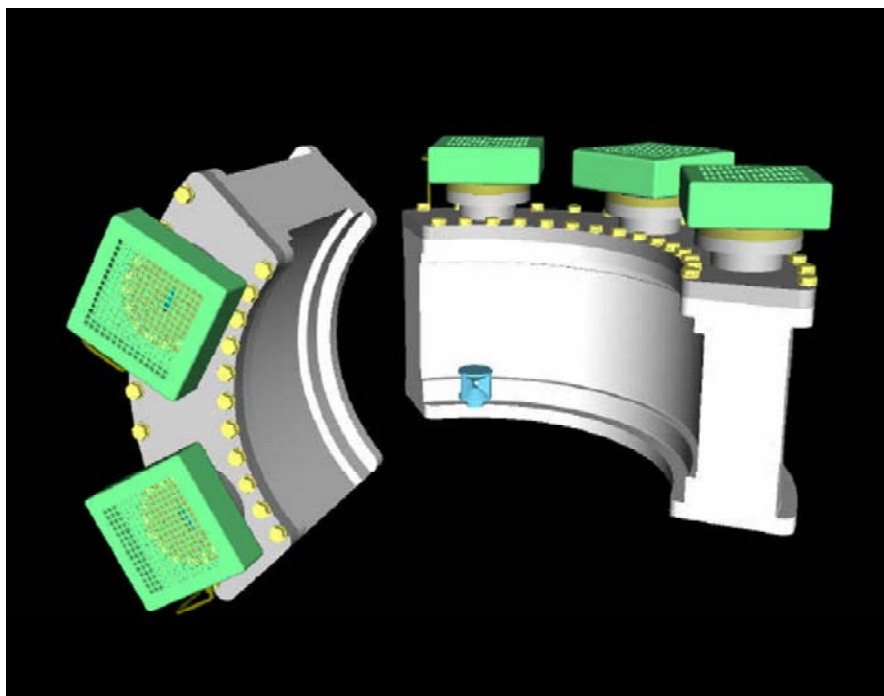


Fig. 2.20. Arrangement of two of the proposed detectors, with significant angular coverage within the restrictions imposed by the gem anvil pressure cell. The panoramic cell is shown in blue. Examples of detector geometry are shown by the grey panels. The left-hand detector, curved in the vertical plane, subtends ($\pm 34^\circ$ by 30° in 2θ), and the right-hand detector, curved in the horizontal plane, subtends ($\pm 52.5^\circ$ in 2θ by 30°). Each detector has a radius of curvature of 0.37 m in this rendition.

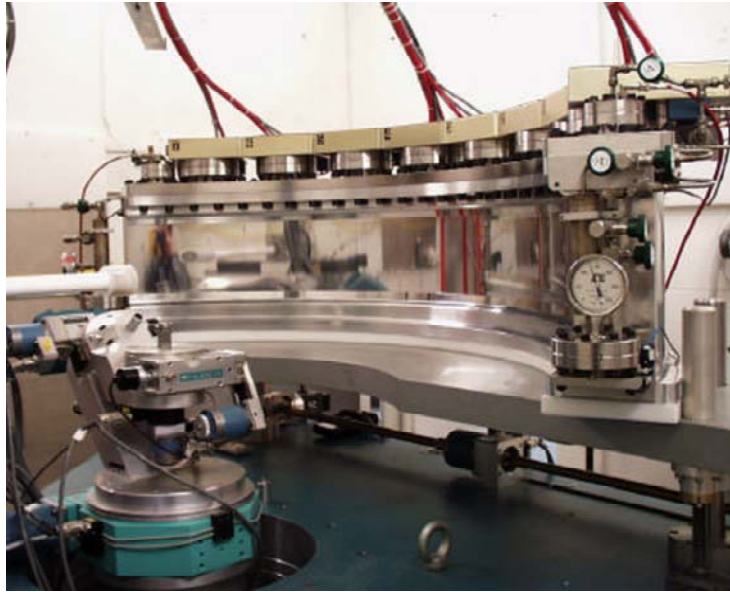


Fig. 2.21. A curved detector, covering $120 \times 15^\circ$ with a radius of curvature of 0.7 m that has recently been commissioned for protein crystallography at LANSCE. It is shown mounted on the beam line's goniometer. Based on wire proportional chamber technology with a ^3He filling, its operating principle and performance characteristics are quite similar to those required for SNAP.

The LANSCE instrument has been in operation since September 2001. During this time, a number of biological samples have been studied. The experience gained has established the validity of the design and construction philosophy.

3. HIGH-RESOLUTION CHOPPER SPECTROMETER (SEQUOIA)

3.1 SEQUOIA INSTRUMENT OVERVIEW

The high-resolution chopper spectrometer instrument (SEQUOIA) is a direct geometry spectrometer that will be positioned on SNS beam line 17. A three-dimensional rendering of the instrument is shown in Fig. 3.1. Figure 3.2 shows a schematic diagram labeling the components described subsequently. The proximity between SEQUOIA and the high-resolution chopper spectrometer (ARCS), on beam line 18, means that the two projects must integrate portions of their design. For example, the incident flight path shielding is contiguous between these two instruments. SEQUOIA is described in Sections 3.2 through 3.4. Section 3.2 describes the incident flight path, including everything upstream of the sample position. Section 3.3 details the area around the sample. Everything downstream of the sample, including the detectors, is covered in Section 3.4.

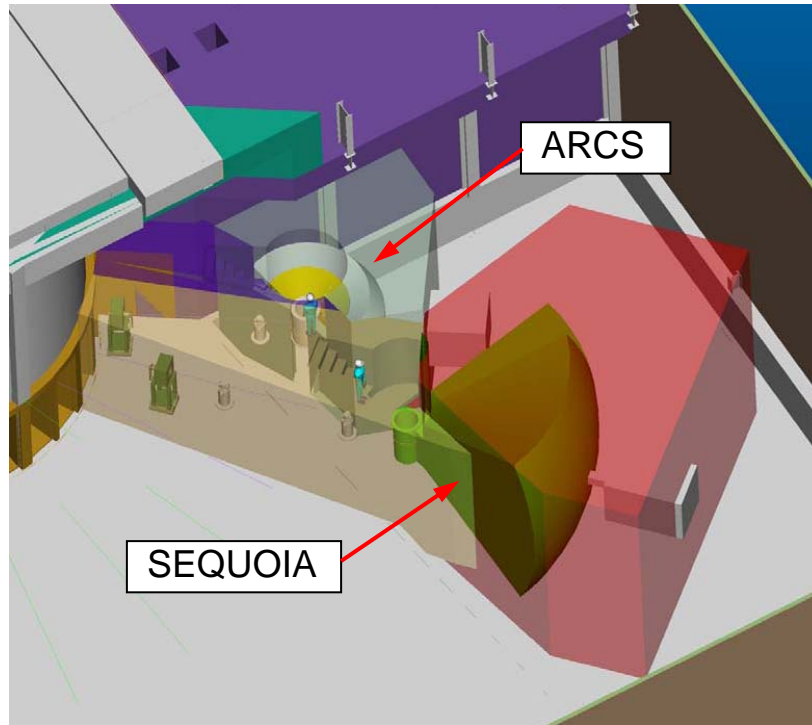


Fig. 3.1. Three-dimensional rendering of SEQUOIA. ARCS is also shown.

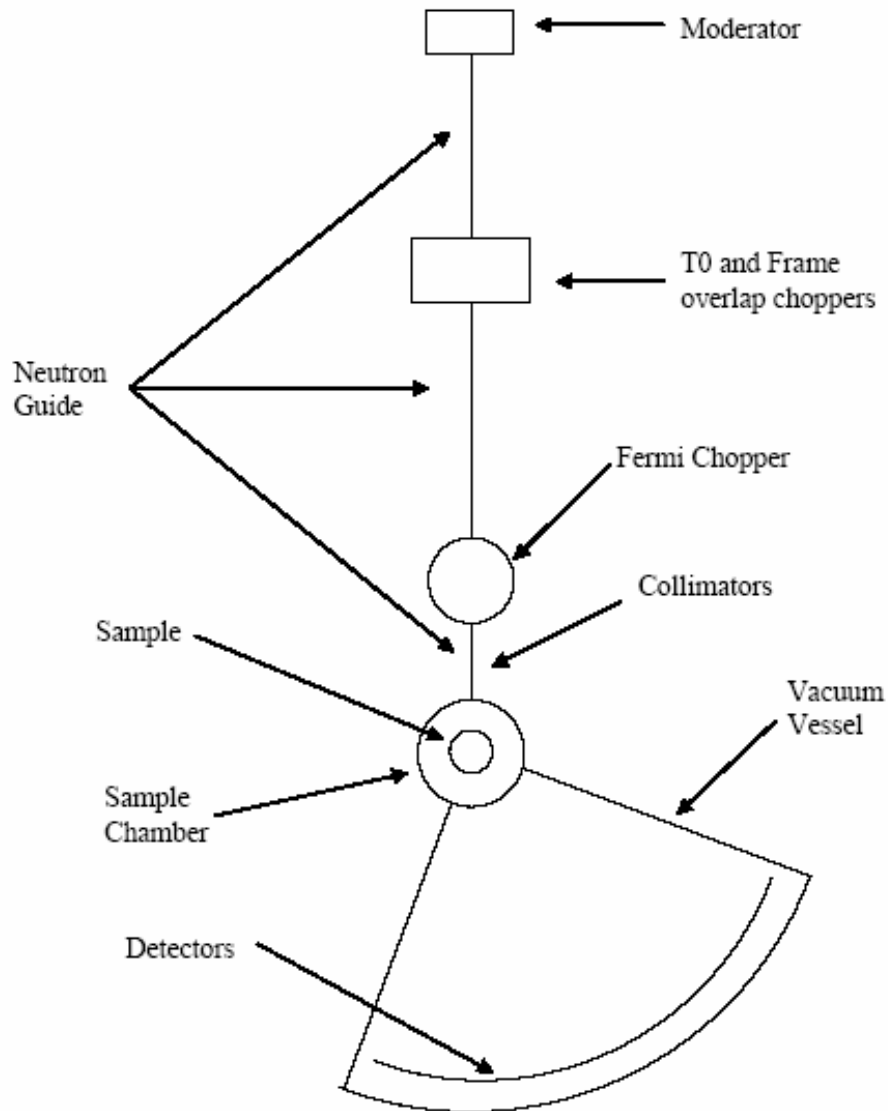


Fig. 3.2. Schematic diagram of SEQUOIA with the components described in Sections 3.2 through 3.4 labeled.

3.2 INCIDENT FLIGHT PATH

3.2.1 Moderator

The poisoned decoupled water moderator, as viewed by beam line 17, was chosen for SEQUOIA. This moderator provides a short time pulse with an energy range appropriate for the design of this spectrometer. Beam line 9 was also considered. However, the increased space, at distances closer to the moderator when the two-chopper concept of D. Abernathy¹ is used, makes beam line 17 the location of choice for this instrument.

3.2.2 T₀ Chopper

The purpose of the T-zero (T₀) chopper, which will be located about 10 m from the moderator, is to suppress the prompt pulse of fast neutrons produced when the proton beam strikes the target. A thick blade of the alloy Inconel is rotated at the source frequency of 60 Hz and is phased to block the beam line when this background radiation is produced. The maximum transmitted energy depends on the blade width and radius, rotation speed, and position along the beam line. For SEQUOIA, this maximum energy is 500 meV. If an experiment requires an incident energy higher than 500 meV, the T₀ chopper will be able to rotate at twice the source frequency (120 Hz) to pass neutrons of energies up to ~1.5 eV.

SEQUOIA will benefit from the prototyping efforts under way in the SNS Chopper Development Group at Argonne National Laboratory (ANL). A 60-Hz T₀ chopper has been installed in the general purpose powder diffractometer (GPPD) at ANL's Intense Pulsed Neutron Source (IPNS) and has been operating without incident for more than a year. The GPPD will continue to run to help identify design flaws that are apparent only after extended usage. The further development of T₀ choppers, capable of spinning at 120 Hz, will be a joint development effort of ARCS, SEQUOIA, and the SNS Chopper Development Group.

3.2.3 Neutron Guide

Many experiments on SEQUOIA would benefit from increased flux at the sample position obtained by accepting a larger angular divergence. This can be accomplished for modest incident energies (for E < 100 meV) using a supermirror neutron guide. Three sections of guide will be used in this spectrometer. First, there will be a 2-m section in the shutter. Second, a 12.5-m segment will span the distance between the shutter and the Fermi chopper. This segment will have cutouts for the T₀ chopper and a frame overlap chopper. Third, a 2-m section will span the distance between the Fermi chopper and the sample position, where a portion can optionally be replaced by a collimator. The whole guide system is tapered to continuously compress the beam from its 10- × 12-cm size emitted by the moderator to a 5- × 5-cm size at the sample position. To obtain a flux gain over the broadest range of energies, the guide will be coated with the state of the art m = 3.6 coating.

The guide-mounting scheme must be designed carefully to minimize background from the target. The guide multilayers will be deposited on thin glass substrates held within steel jackets, allowing maximum shielding close to the reflecting layers. Neutron-absorbing fixed apertures of B₄C will be placed as needed to suppress the neutrons scattered where the beam hits the shield jacket. The guide sections will be evacuated for efficient transport of lower-energy neutrons.

3.2.4 Frame Overlap Chopper

The high rotational frequency of the Fermi chopper causes it to open many times between neutron pulses. One consequence is that neutrons of different velocities pass through the Fermi chopper at its different openings. In addition, fast neutrons from the next pulse may arrive at the detectors before the slowest neutrons from the present pulse are counted. An additional chopper rotating at a lower frequency will suppress both of these sources of spurious neutron pulses. One option for this chopper is the standard SNS frame overlap disc chopper. However, it is not clear whether disk choppers will be sufficiently opaque to the most energetic neutrons. So we might use a rough pre-monochromator consisting of a coarse Fermi chopper, similar to the T₀ choppers on the HRMECS and LRMECS spectrometers at IPNS. By spinning this chopper at a lower multiple of the source frequency than the Fermi chopper, only neutrons of the correct energy will pass to the sample in the desired data acquisition time frame. Simulations will be undertaken to determine whether this type of chopper will improve the pulse shape by cutting out more of the moderator pulse tail or whether a simpler disk chopper is sufficient.

3.2.5 Fermi Chopper

The Fermi chopper produces a monochromatic burst of neutrons with energy dependent on the chopper phase. This chopper will be located at 17.5 m from the moderator position. Both the intensity and resolution at the sample position are controlled by the chopper rotation speed and the width, length, and curvature of the neutron paths through the chopper. The rotation speed will be any multiple of 60 Hz up to 600 Hz. The slit dimensions will be changed by replacing the slit package. Although the precise set of slit packages required for the instrument will require detailed design, four or five slit packages should be sufficient to cover the energy and resolution ranges of this instrument. The choice of packages will be made taking the capabilities of the ARCS instrument into consideration to ensure that the correct and complementary balance of energy and resolution ranges is available. A program is currently under way to develop a carbon fiber wrapped slit package for the HRMECS Fermi chopper instrument at IPNS. This collaboration has fostered a Small Business Innovation Research (SBIR) Grant for the manufacturing company to develop this technology further for SNS instruments. SEQUOIA will take advantage of these new developments.

3.2.6 Collimators

The interchangeable set of collimators between the Fermi chopper and the sample allows the user to control the angular divergence of the neutrons incident on the sample and thus the Q resolution of the instrument. The natural divergence from the guide system is $\sim 1^\circ$ at the lowest energies. Therefore, collimators with more than 1° divergence are superfluous. The angular width of a detector at 5.5 m is $15'$, and this value sets the lower limit of usable collimation. Therefore, we plan on using three boron-coated stretched film collimators passing divergences of $15'$, $30'$, and $45'$. A fourth option, where guide will be in this position, will be available for those experiments that can benefit from putting the maximum available divergence on the sample. To ease the interchange of these collimators, a rotating carousel developed for the SNS SANS instrument will be used.

3.2.7 Biological Shielding

The high power of the SNS source requires massive shielding to protect the instrument staff and users and to reduce the background observed in the detectors. The shielding must also allow access to beam line components such as the Fermi chopper and sample area. The SNS shielding groups have completed calculations for typical instrument configurations. From these calculations and the geometrical constraints of the SEQUOIA and ARCS spectrometers, neither instrument should be a biological concern for itself or neighboring instruments. Nevertheless, detailed calculations are under way for the exact configuration of the ARCS instrument. Because of the proximity to the ARCS instrument, these calculations also include the expected incident beam line of SEQUOIA. Therefore, much of the design of the incident beam line shielding will be completed in the ARCS design. Nevertheless, calculations for areas where no overlap exists will still be required.

3.3 SAMPLE CHAMBER

3.3.1 Vacuum Isolation

Inelastic neutron-scattering experiments inherently measure small signals. Therefore, to optimize measurements, background signals must be reduced to as low a level as possible. One demonstrated method of reducing background is to evacuate the sample chamber. This requires either a contiguous vacuum with the detector tank or a thin aluminum window between the detector tank and sample area. The best practice for inelastic neutron-scattering measurements with chopper spectrometers is to eliminate

any windows between the sample area and the detector flight path [as has been done for the multi-angle chopper spectrometer (MAPS) spectrometer at ISIS, for example]. However, the contiguous vacuum option means that the detector tank vacuum must be cycled each time a sample is changed. Therefore, to eliminate fatigue problems from frequent cycling of the vacuum in the main part of the vessel, and to save time in restoring a cryogenic vacuum at the sample (the internal neutron shielding, “crispy mix,” is somewhat hygroscopic), a method for isolating the sample area vacuum from the rest of the tank will be developed. Sample changes will occur while the main vessel remains under vacuum, but the sample space will be opened to the main vacuum after the sample space is evacuated.

3.3.2 Sample Manipulation

Much of the science to be done on ARCS involves single-crystal samples. For these experiments, it is necessary to orient a particular direction in the reciprocal lattice of the sample, \mathbf{q} , with respect to the wave vector transfer, $\mathbf{Q} = \mathbf{k}_i - \mathbf{k}_f$, probed by the spectrometer. Figure 3.3 shows a case where the scattering of the (red) neutron beam involves a change in wave vector of \mathbf{Q} , which lies on a cone around the center of the sample. In many cases, a vector in the sample, \mathbf{q} , can be made to intersect this cone by a simple rotation by ω about a vertical axis. This degree of freedom is particularly simple to implement with a rotation stage. On the other hand, to probe several directions of \mathbf{q} simultaneously, such as mapping full dispersions, additional degrees of freedom for sample tilt will be required.

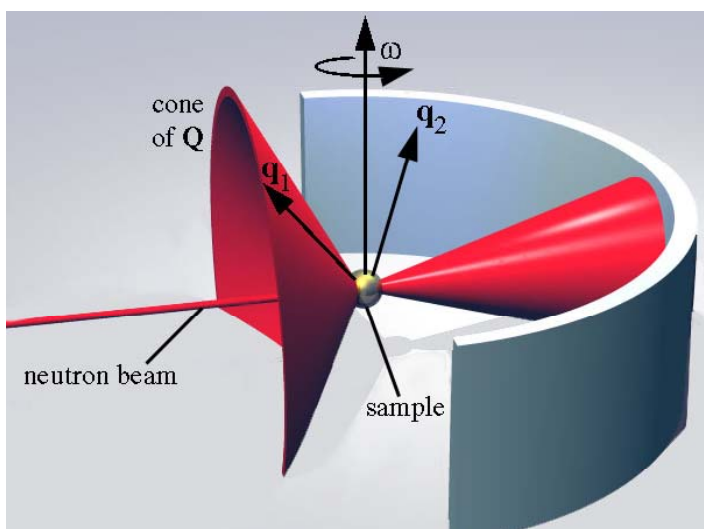


Fig. 3.3. One degree of freedom allows \mathbf{q}_1 to intersect \mathbf{Q} by rotation of ω . Another degree of freedom is required for both \mathbf{q}_1 and \mathbf{q}_2 to simultaneously intersect \mathbf{Q} . (Here, \mathbf{q}_i points along the incident beam, and \mathbf{q}_f lies along the red cone at right.)

The rotation stage for the vertical rotation will include the flange for mounting the sample environment units atop the vacuum vessel. This requires the design of a rotating vacuum feed-through. The diameter of the SNS standard bolt circle will set the size of the sample environment units. The sample rotation stage will be based on a commercial rotation table. A stepping motor and associated controller connected to the data acquisition software will control the angular setting of the rotation stage to within an accuracy of ~ 0.01 degrees. Mounting of this rotation stage on SEQUOIA with a flexible bellows coupling to the chamber will be investigated. Having all sample motions on the spectrometer itself seems most practical for the standardization of data collection and subsequent analysis.

3.4 FINAL FLIGHT PATH

3.4.1 Vacuum Vessel

The vacuum vessel serves three purposes. It provides an evacuated secondary flight path, its shielding provides a low-background environment for the detector bank, and its vacuum provides thermal insulation for some sample environments. The inner volume of the vessel will be approximately 89 m^3 , a massive structure that will require careful engineering for safe and reliable operation.

Currently, we anticipate that the detectors will be mounted in vacuum within the vessel. This eliminates thin aluminum windows, used in most currently operating spectrometers that must withstand many cycles of differential pressure between zero and one atmosphere. This is a safety issue because the evacuated structure stores 9 MJ of mechanical energy. Furthermore, separation of the vessel structural elements from the detector and window mounting enhances the available continuous detector coverage. This is a prime consideration for single-crystal spectroscopy. The SNS detector and data acquisition groups, in collaboration with the ARCS project, are developing preamplifier and digitization electronics needed to operate linear-position-sensitive ^3He tubes in vacuum, and we expect the SEQUOIA project to use these developments. The plan is to digitize the signals from 8 or 16 detector packs in vacuum, reducing the need for complex vacuum feed-throughs of analog detector signals. Vacuum sensors will shut off the detector high voltage if the pressure in the vessel approaches a range where arcing could occur.

The design of the detector and sample tank will permit the use of large cryomagnets and possible future use of polarizing elements. To meet these requirements, the vacuum vessel should be constructed of nonmagnetic materials within 1 or 2 m of the sample to avoid interactions with fringing fields of magnets in the sample region and to reduce stray fields that affect polarizing elements. One promising technology for producing high-energy polarized neutrons is polarized ^3He filters, which are extra sensitive to these stray magnetic fields. The spectrometer design will be consistent with future installation of incident beam and analyzing filters so they can be installed once their design and usage becomes mature.

3.4.2 Detectors

The detector array on SEQUOIA will consist of 1458 1.2-m-long by 2.5-cm-diam ^3He tubes. Each tube will be position sensitive along its length, with pixels of 2.5 cm in length. Therefore 69,984 pixels will be available for neutron detection. Each pixel will cover an angle of 0.25° in the horizontal and vertical direction, corresponding to 2×10^{-5} steradians. For this instrument, the best possible Q resolution is partially limited by the width of the detectors. However, reducing the size of the detectors would either reduce the efficiency of the detector bank and/or become cost prohibitive. The achievable Q resolution will be optimal for the vast majority of experiments. Therefore, we do not think we would benefit from smaller tubes. For powder samples, software will re-bin the detector data into Debye-Scherrer rings. Angles from -30 to $+60^\circ$ in the horizontal plane and $\pm 30^\circ$ vertically will be accessed with even spacing of the detectors to the extent possible, while maintaining the structural integrity of the vacuum vessel. To simplify removal for maintenance purposes and to efficiently use the associated electronics, detectors will be grouped in packs of 8 or 16. The detector array and associated electronics are the single most expensive component of SEQUOIA, but they are required to produce a world-class instrument.

3.4.3 Shielding

To improve dynamic range and sensitivity, the SEQUOIA detector banks will be shielded from neutrons that would otherwise enter from outside the instrument. One possible way to shield from these external neutrons is to surround the detector tank with 30-cm shell, thin-walled steel containers filled with

a mixture of wax and borax ($\text{Na}_2\text{B}_4\text{O}_7$) for moderation and absorption. Alternative solutions such as borated concrete will also be considered.

Another source of background neutrons is scattering off the tank walls into detectors. To eliminate this background contribution, the entire inside of the tank will be coated with boron-loaded epoxy (crispy mix).

The SNS Instrument Systems Group is conducting a series of tests at IPNS to determine the thickness and composition of shielding for SNS instruments. SEQUOIA will take advantage of the results of this study. In anticipation of future proton current upgrades and taking into account previous incidents where shielding requirements were underestimated, we will tend to be generous with shielding material.

3.5 COMPUTER HARDWARE AND DATA ACQUISITION

The data acquisition and analysis systems will be built from commercially available components, following the standards under development at the SNS.² The system will consist of four computers: a control computer, a data analysis computer, a chopper control computer, and a sample environment computer. The control computer will send commands to the chopper control and sample environment computers to control the experiment. The data will be stored in a RAID array. Both the control computer and the data analysis computers will have access to the RAID array, so the control computer can be isolated for control purposes only and all analysis features will be handled on the data analysis computer. Depending on the rate of information transported between these computers, either high-speed Ethernet or fiber channel communications will be used. Both the data analysis computer and the control computer will be accessible from external computers via the Internet using the standard SNS security protections. Only systems that can be modified without compromising safe operation will be remotely controllable, although all relevant machine parameters should be viewable. Between the detector and the control computer, a modular system of hardware will digitize the position and time of each neutron event.

The SEQUOIA instrument will use the data acquisition software provided by SNS. Data analysis software for SEQUOIA will be developed in collaboration with the ARCS instrument. SNS is developing software for data visualization in a generic form, making it suitable for time-of-flight data obtained at any facility. By adhering to the standard SNS data format being developed, portability of SEQUOIA data to this (or any other) analysis package will be ensured. The user interface to the data acquisition system will be through a web browser, decoupling the location and operating system of the spectrometer from those of the user. These attributes for the data acquisition system are already among the specifications for the SNS data acquisition system, and SEQUOIA will take advantage of software systems currently under developments by SNS.

3.6 SAMPLE ENVIRONMENT

3.6.1 Closed Cycle Refrigerator (9–350 K)

Many experiments that will be performed on SEQUOIA will need temperatures between 9 K and room temperature. A closed-cycle helium refrigerator is well suited to this temperature range. Furthermore, ease of operation makes this device ideal for the user program.

3.6.2 Cryo-Furnace (2–700 K)

Most experiments that require a greater temperature range than provided by the closed-cycle refrigerator could be performed in a device that provides a range of 2 to 700 K. This would require fills of cryogenic fluids by qualified SNS personnel. However, this inconvenience is much less than that created by the extended cooldown times of any currently available closed-cycle device.

3.7 INSTRUMENT PERFORMANCE

An instrument's performance is basically determined by how fast and with what accuracy properties of the user's sample are measured. In the field of inelastic neutron scattering, there are a vast number of phenomena in many varied samples to investigate. Nevertheless, there are a few sample independent quantities that characterize an instrument and can be optimized for a specific subset of experiments. These parameters are flux on sample, incident energy (E) range, energy transfer resolution (ΔE), momentum transfer (\mathbf{Q}) range, and momentum transfer resolution ($\Delta \mathbf{Q}$). The E range is largely selected by moderator choice. Therefore, inelastic instruments and their optimized experiments naturally separate into two groups—those that use cold-to-thermal neutrons and those that use thermal-to-epithermal neutrons. At SNS, the backscattering and cold neutron chopper spectrometers will provide wide ranges of ΔE , \mathbf{Q} , and $\Delta \mathbf{Q}$ resolution to the community served by cold neutrons. For the community that needs access to thermal and high-energy neutrons, the ARCS instrument will provide a large \mathbf{Q} range, a reasonable minimum $\Delta \mathbf{Q}$, and plenty of intensity for moderate ΔE . The large \mathbf{Q} range of ARCS is essential for the community interested in lattice vibrations and the phonon density of states. However, investigations of magnetic excitations, especially in single crystals, demand finer $\Delta \mathbf{Q}$ and ΔE with correspondingly higher flux than is provided by ARCS. SEQUOIA is optimized to meet these needs. This paragraph describes the performance of SEQUOIA and illustrates the complementarity between the fine \mathbf{Q} resolution of SEQUOIA and the large \mathbf{Q} range of ARCS.

3.7.1 Intensity and Energy Resolution

In previous documents¹ the energy resolution and flux considerations have been explained in great detail. Therefore only an overview of the energy resolution and predicted flux values will be presented in this document. The energy resolution is efficiently modeled by analytical methods and has been discussed in great detail by D. Abernathy.¹ For the present discussion we use the model of J. Carpenter³ in which the energy resolution is given by

$$\Delta E = m \left[\left(\frac{v_1^3}{L_1} + \frac{v_3^3 L_2}{L_1 L_3} \right)^2 \Delta t_p^2 + \left(\frac{v_1^3}{L_1} + \frac{v_3^3 (L_2 + L_1)}{L_1 L_3} \right)^2 \Delta t_c^2 + \left(\frac{v_3^3}{L_3} \right)^2 \Delta t_d^2 \right]^{\frac{1}{2}}, \quad 3.1$$

where m is the mass of the neutron; L_1 , L_2 , and L_3 are the distances between moderator and chopper, chopper and sample, and sample and detector, respectively; v_1 is the initial velocity v_3 and is the final velocity; Δt_p is the time width produced by the moderator; Δt_c is the time width produced by the chopper; and Δt_d is the timing uncertainty caused by the sample size and detector width. The Δt_c term is given in terms of the Fermi chopper parameters⁴ by

$$\Delta t_c = \frac{1}{4\pi f} \frac{d}{R}, \quad 3.2$$

where d is the slit width, R is the chopper radius (design value 5.0 cm for both ARCS and SEQUOIA), and f is the frequency. The best (or finest) energy resolution is given by the maximum value of f (600 HZ for ARCS and SEQUOIA) and the minimum value of slit width. The latter is chosen as the realistic value of 1.5 mm for the purposes of this document. Calculations using these values, showing the best energy resolution (FWHM) at zero energy transfer for ARCS (blue) and SEQUOIA (red), are shown in Fig. 3.4a. A 1-cm-thick sample was assumed for these calculations. The plot shows that SEQUOIA will have a resolution of better than 1.5% for $E_i < 250$ meV.

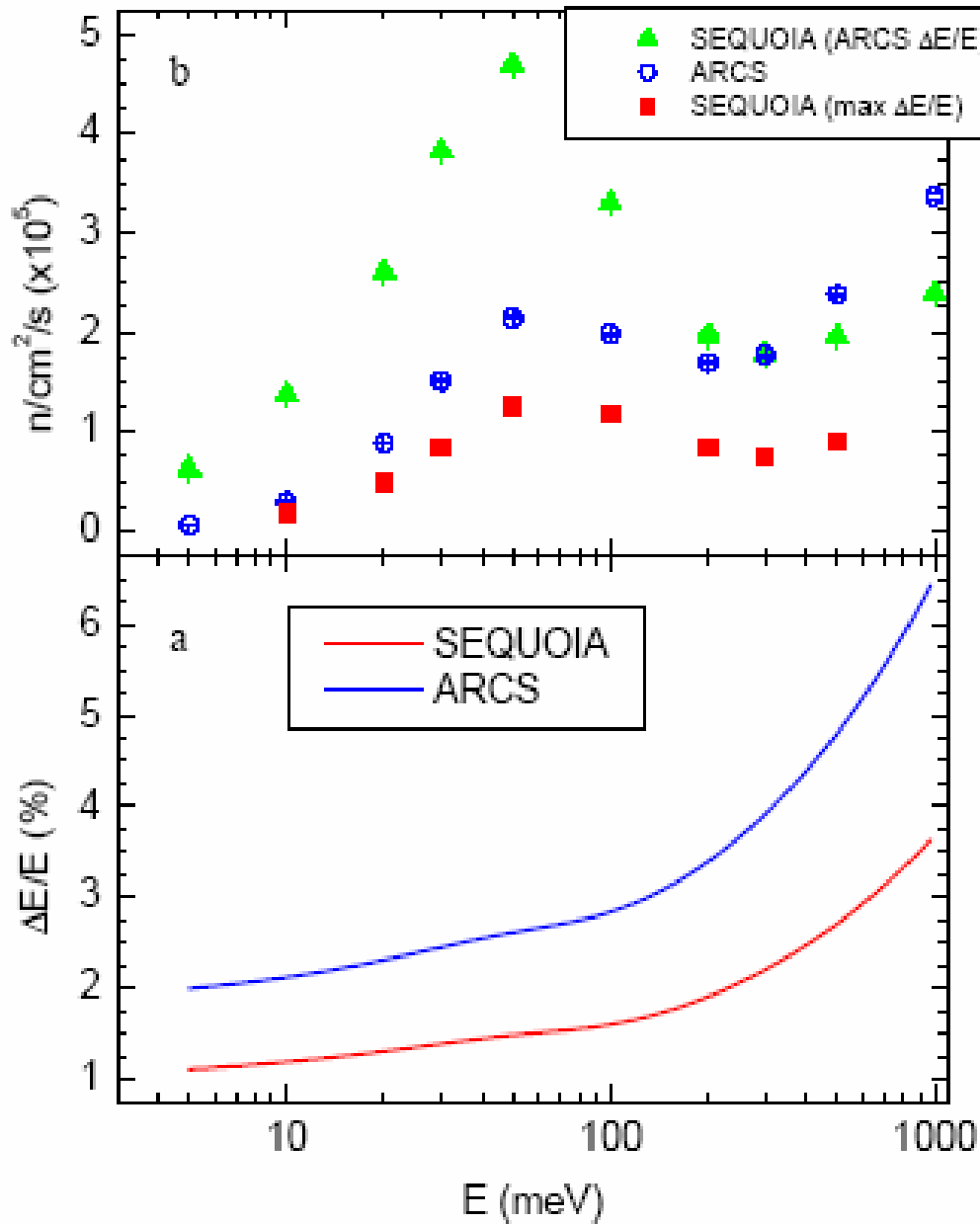


Fig. 3.4. Flux on sample and energy resolution for the SEQUOIA spectrometer. For comparison, similar flux values are plotted for the ARCS spectrometer and for the SEQUOIA spectrometer when the resolution is the same as ARCS. Resolution for the ARCS spectrometer (upper resolution curve) is also shown for comparison.

The neutron flux on sample is a useful quantity that provides a reasonable indication of relative intensities for the comparison of different instrument designs. The McStas Monte Carlo package⁵ has proved useful in calculating the flux on sample for several different instrument configurations. Complete instrument simulations, with the components as described in Sections 3.2 through 3.4, have been performed. More specifically, the source component produces neutrons according to the MCNPX calculated distributions provided by E. Iverson.⁶ The Fermi chopper is a slit package of curved absorbing blades spaced at 1.5 mm that is spun at 600 Hz. The curvature of the blades was optimized for each E .

The neutrons are counted with a pixilated detector at the sample position to determine the flux. Specifically, integration over a 4×4 -cm area of this detector is performed to obtain the flux on sample.

The red and blue points in Fig. 3.4b (upper panel) show the corresponding flux on sample at the resolution shown in Fig. 3.4a. The energy resolution on SEQUOIA can be relaxed by increasing the chopper slit width. The green triangles show the flux obtained on SEQUOIA when its resolution is adjusted to match the finest achievable resolution of ARCS. In this resolution regime, SEQUOIA will deliver more flux on sample than ARCS, except for very high incident energies.

Figure 3.5 further illustrates the flux comparison between these two instruments by examining the flux, calculated by MC, as a function of the resolution given by Eq. 3.1. Note that for an incident energy of 50 meV, relaxing the energy resolution from 1.2 to 5% can gain as much as an order of magnitude more flux on SEQUOIA. Corresponding gains are observed for the ARCS instrument. These results illustrate the tradeoff between flux and resolution. For moderate incident energies, the SEQUOIA instrument puts more flux on sample than ARCS for equal ΔE . There are two primary reasons for the greater flux of SEQUOIA. First, the neutron guide transports the low-energy neutrons very efficiently. Therefore, SEQUOIA does not suffer a loss of low-energy neutron flux by being farther away from the moderator. Second, as seen in the second term of Eq. 3.1, the longer final flight path (L_3) of SEQUOIA means that Δt_c can be relaxed when compared to ARCS under the same resolution condition. Increasing Δt_c means increasing the energy bandwidth, and hence the flux, of neutrons incident on the sample. These effects were described in detail using analytical calculations by D. Abernathy¹ and are illustrated by the 50-meV curves. At sufficiently large energies ($E > 100$ meV), the guide no longer assists in transporting the neutrons.

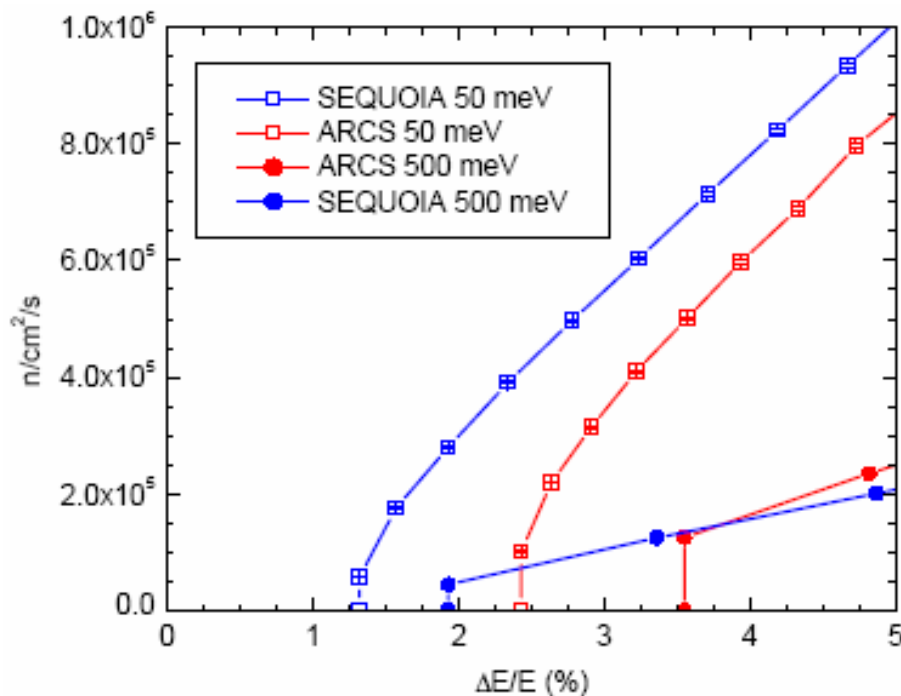


Fig. 3.5. Flux on sample for ARCS (red) and SEQUOIA (blue) as a function of energy resolution, for incident energies of 50 and 500 meV.

The bandwidth advantage arising from a longer flight path also decreases as the incident energy is increased. Under the conditions of sufficiently large E and coarse ΔE , ARCS puts more flux on sample than SEQUOIA. This effect is illustrated by the crossover of the 500-meV curves in Fig. 3.5 and similarly explains the crossover observed for the green and blue curves in Fig. 3.4b.

3.7.2 Q Resolution and Range

Two additional parameters that characterize the performance of SEQUOIA are the **Q** resolution ($\Delta\mathbf{Q}$) and range. The **Q** range is largely controlled by the angular coverage. Analytical calculations, after J. Carpenter,³ provide the needed insight to describe $\Delta\mathbf{Q}$. There are two cases to consider: the first is the powder case where only the magnitude of **Q** (Q) can be determined and therefore only the uncertainty in **Q** (ΔQ) is important. The second case assumes a single crystal, and in this case the uncertainties in the components of **Q** parallel (Q_x) and perpendicular (Q_y) to the beam will be considered.

For the powder case Q is given by

$$Q = \frac{m}{\hbar} \sqrt{(v_1)^2 + (v_3)^2 - (v_1)(v_3)\cos(\phi)}, \quad 3.3$$

where ϕ is the scattering angle. The resulting uncertainty, taking into account the cross correlations between Δt_c and Δt_p (see the aforementioned definitions) are then

$$\Delta Q = \left(\frac{\left(\frac{m}{\hbar} \right)^2}{2Q} \right) \sqrt{ \left[\left(2 \frac{v_3^3}{L_3} \frac{L_2}{L_1} - 2 \frac{v_1^3}{L_1} + v_3 \frac{v_1^2}{L_1} \cos(\phi) - L_2 \frac{v_1}{L_1} \frac{v_3^2}{L_3} \cos(\phi) \right)^2 \Delta t_p^2 + \left(2 \frac{v_3^3}{L_3} \frac{L_2}{L_1} - 2 \frac{v_1^3}{L_1} + v_3 \frac{v_1^2}{L_1} \cos(\phi) - L_2 \frac{v_1}{L_1} \frac{v_3^2}{L_3} \cos(\phi) \right)^2 + \left(v_1 \frac{v_3^2}{L_3} \cos(\phi) - 2 \frac{v_3^3}{L_3} \right)^2 \right] \Delta t_c^2 + (v_1 v_3 \sin(\phi))^2 (\Delta\phi^2 + \Delta\alpha^2) + \left(2 \frac{v_3^3}{L_3} - v_1 \frac{v_3^2}{L_3} \cos(\phi) \right)^2 \Delta t_d^2 }, \quad 3.4$$

where $\Delta\phi$ is the uncertainty in the scattering angle and $\Delta\alpha$ is the incident divergence. The results of these calculations for the instrument described in Sections 3.2 through 3.4 are shown in Fig. 3.6. The Δt_c was determined assuming a Fermi chopper with 1.5-mm-blade spacing spinning at 600 Hz. A sample size of 1 cm was assumed. The main point to take away from this plot is that SEQUOIA has significantly finer **Q** resolution, while ARCS covers a greater range in **Q**.

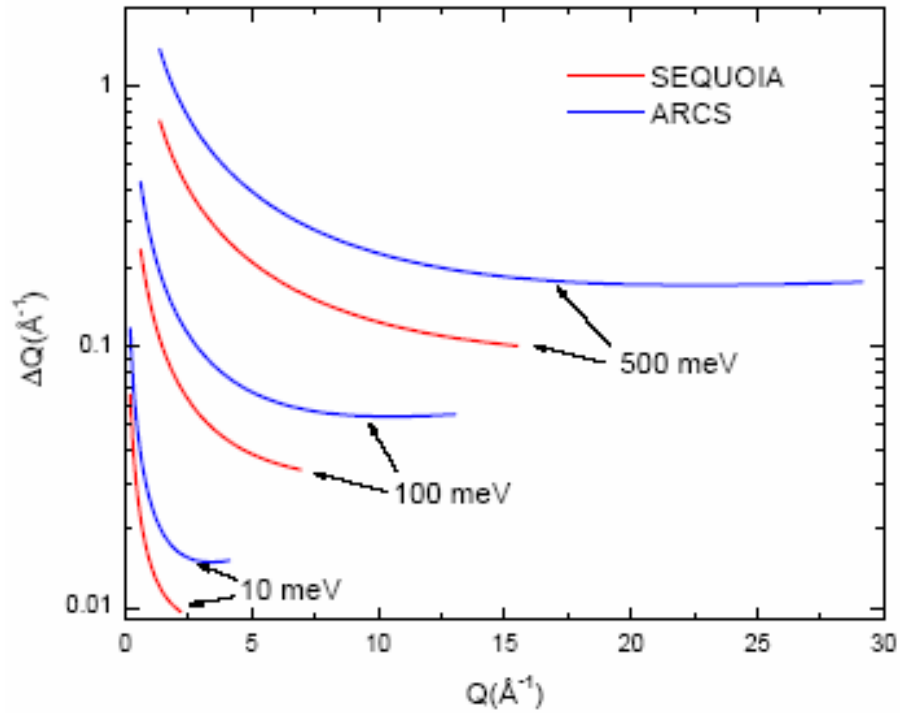


Fig. 3.6. Finest possible Q resolution for the SEQUOIA instrument for elastic scattering for several different incident energies. For comparison, similar curves are also shown for the ARCS instrument (upper curve in each set).

For single-crystal experiments, a specific sample orientation is defined with respect to the incident beam. Therefore, both the magnitude and direction of \mathbf{Q} can be determined in an experiment. For the purposes of our discussion, following Carpenter,³ we consider components of \mathbf{Q} parallel (Q_x) and perpendicular (Q_y) to the incident beam (Fig. 3.7).

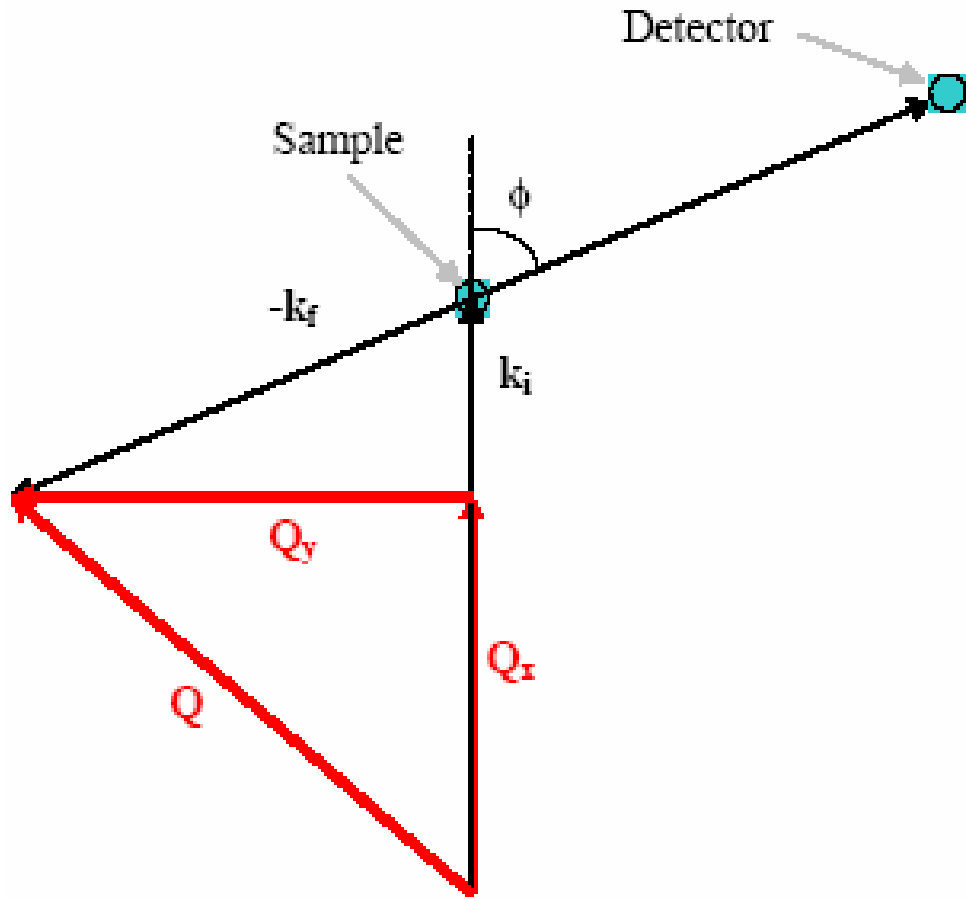


Fig. 3.7. The components of \mathbf{Q} defined by the instrument geometry.

The two components are given by

$$Q_x = \left(\frac{m}{\hbar}\right) [v_1 - v_3 \cos(\phi)] , \quad 3.5$$

and

$$Q_y = -\left(\frac{m}{\hbar}\right) v_3 \sin(\phi) . \quad 3.6$$

The locus of \mathbf{Q} components for elastic scattering at selected incident energies is illustrated in Fig. 3.8 for SEQUOIA and in Fig. 3.9 for ARCS. The larger angular coverage of the ARCS detector bank results in a correspondingly larger range of wave vector being measured.

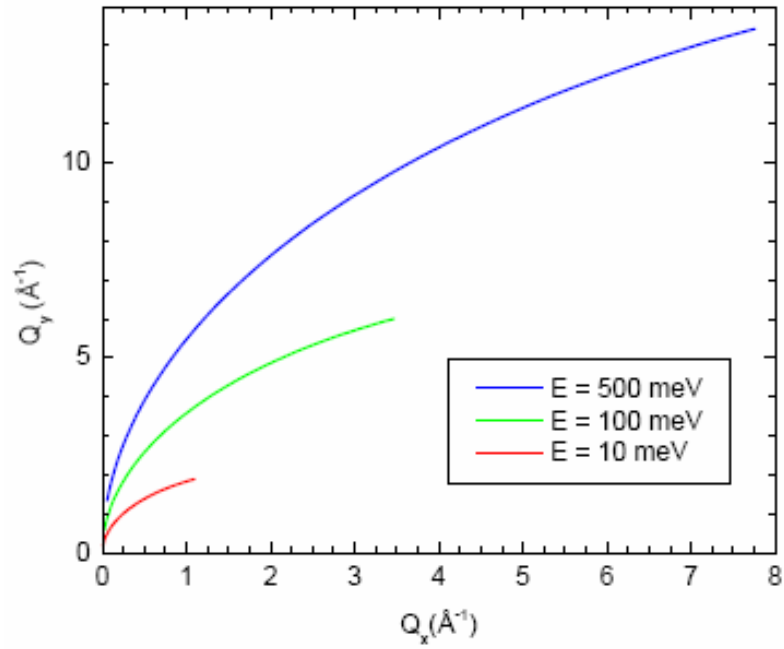


Fig. 3.8. Locus of Q components for SEQUOIA.

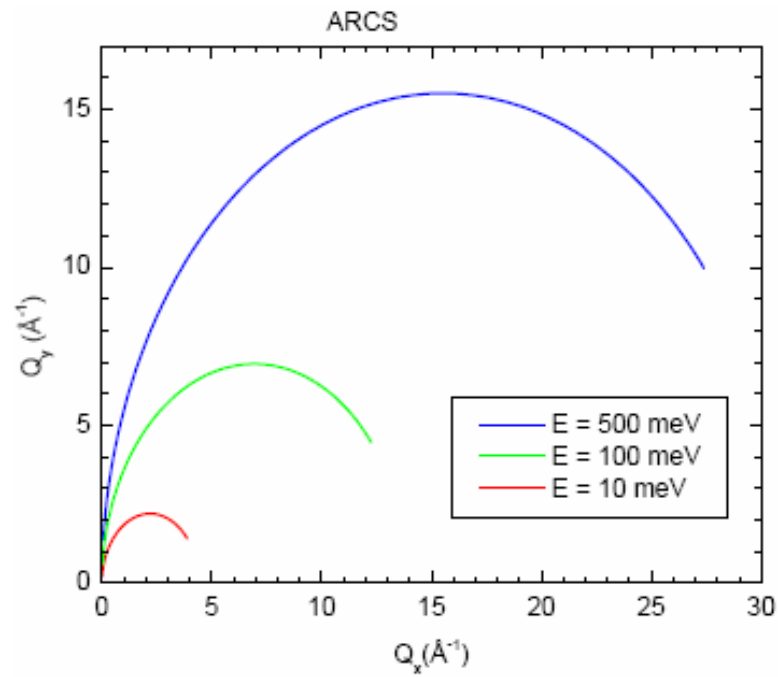


Fig. 3.9. Locus of Q components for ARCS.

The uncertainty in \mathbf{Q} along each direction is then calculated by differentiation; again one must remember to consider the correlated terms. The resulting equations are:

$$\Delta Q_x = \frac{m}{\hbar} \left[\frac{1}{L_1^2} \left(v_1^2 + v_3^2 \frac{L_2}{L_3} \cos(\phi) \right)^2 \Delta t_p^2 + \frac{1}{L_1^2} \left(v_1^2 + v_3^2 \frac{L_1 + L_2}{L_3} \cos(\phi) \right)^2 \left(\Delta t_c^2 + \left(\frac{\Delta \alpha}{\omega} \right)^2 \right) \right. \\ \left. + \left(\frac{v_3^2}{L_3} \cos(\phi) \right)^2 \Delta t_d^2 + (v_3 \sin(\phi))^2 \Delta \phi^2 \right]^{\frac{1}{2}} \quad 3.7$$

and

$$\Delta Q_y = \frac{m}{\hbar} \left[\left(\frac{v_3^2 L_2}{L_1 L_3} \sin(\phi) \right)^2 \Delta t_p^2 + \left(\frac{v_3^2}{L_1} \frac{L_1 + L_2}{L_3} \sin(\phi) \right)^2 \Delta t_c^2 + \left(\frac{v_3^2}{L_3} \sin(\phi) \right)^2 \Delta t_d^2 \right. \\ \left. + (v_3 \cos(\phi))^2 \Delta \phi^2 + \left(v_1 + \frac{v_3^2}{L_2 \omega} \frac{L_1 + L_2}{L_3} \sin(\phi) \right)^2 \Delta \alpha^2 \right]^{\frac{1}{2}} \quad 3.8$$

where ω is the angular frequency of the chopper.

Figures 3.10 and 3.11 show ΔQ_x and ΔQ_y as a function of Q_x and Q_y , respectively, for elastic scattering. Again, SEQUOIA provides significantly finer resolution for both Q_y and Q_x . One other detail shown in Fig. 3.11 is that for ARCS a minimum in ΔQ_x is observed. This minimum corresponds to $\phi = 90^\circ$, where several terms in Eq. (3.7) go to zero. This minimum is not observed for SEQUOIA because the detector bank does not extend to 90° . Preliminary MC results are consistent with these analytical calculations.

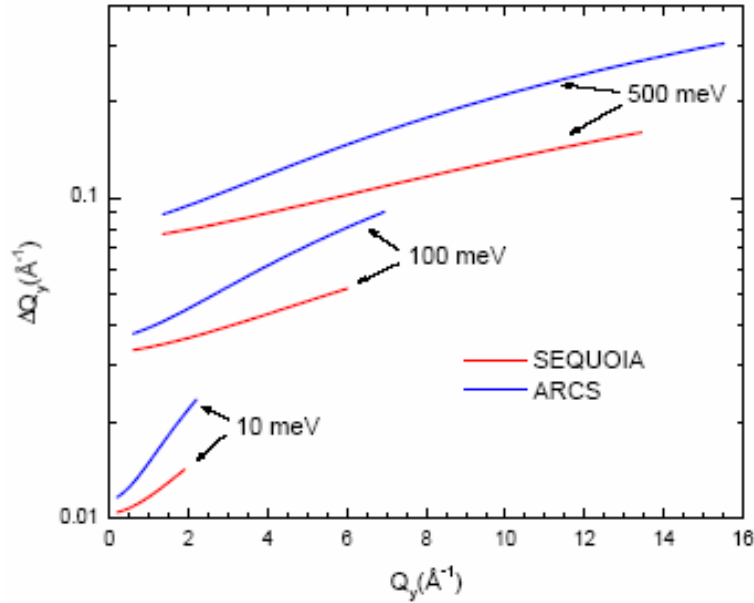


Fig. 3.10. Finest possible Q resolution perpendicular to the incident beam direction. The expected performance for both the SEQUOIA and ARCS instruments are shown for several different incident energies.

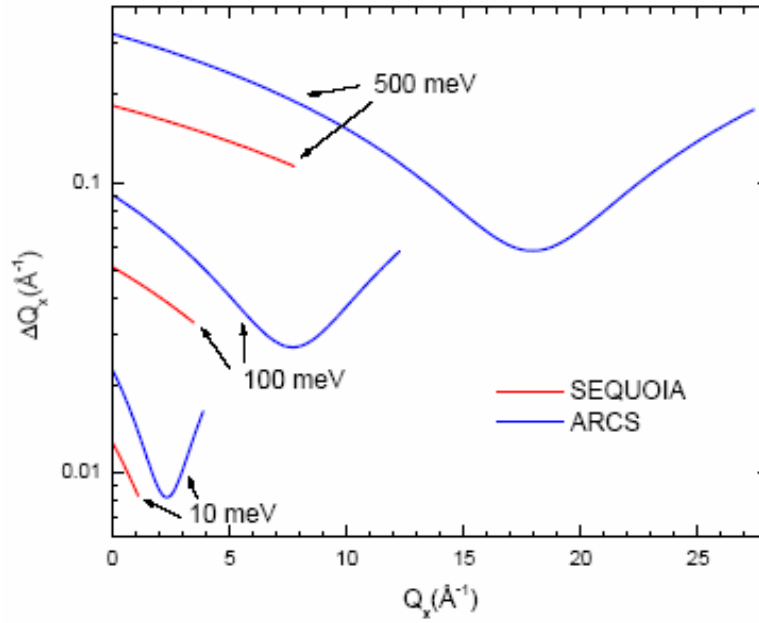


Fig. 3.11. Finest possible Q resolution parallel to the incident beam direction. The expected performance for both the SEQUOIA and ARCS instruments are shown for several different incident energies.

4. SINGLE-CRYSTAL DIFFRACTOMETER (SCD)

This design document is an updated extension based on an earlier report.⁷

4.1 SCD OVERVIEW: CURRENT TREND

For a next-generation, single-crystal diffractometer, a fast and complete data collection of a full diffraction pattern data set is necessary to attain state-of-the-art performance. Currently existing instruments at time-of-flight neutron facilities [e.g., IPNS (ANL) and ISIS (Rutherford Appleton Laboratory, U.K.)] have led the trend to considerably shorten data collection times. The recently updated single-crystal diffractometer, SXD, at the ISIS facility features greatly expanded coverage, from three two-dimensional area detectors (2D detectors) in the horizontal plane to eleven 2D detectors arranged on a half-sphere with radius of ~19.2 cm around the bottom half of the instrument.⁸ With this updated arrangement, nearly 50% of reciprocal space is covered for any given crystal setting, allowing the measurement of data in about three settings for structures that crystallize with monoclinic or higher symmetry. The ability to simultaneously collect as many data points in reciprocal space as possible is a critical feature of the proposed single-crystal diffractometer for SNS (SNS SCD).

4.2 INSTRUMENT DESCRIPTION

The Instrument Oversight Committee gave the following recommendation for the design of the SNS SCD:

“The single-crystal diffractometer could revolutionize single-crystal neutron diffraction. The important thing with this machine is to enable scientists to obtain complete diffraction patterns in a matter of minutes. Thus this machine should incorporate large area detectors with small pixel sizes. The use of toroidal mirrors and other focusing optics should be investigated in order to maximize the intensity. This instrument should be capable of energy discrimination in order to separate elastic diffuse scattering from thermal diffuse scattering. These requirements present a significant design challenge, but if they are met, this instrument would be unique in the world.”

The SNS SCD will employ area detectors and the time structure of the pulsed-neutron source to measure Laue diffraction patterns. The efficiency of sampling the reciprocal lattice simultaneously in both direction (area detection) and wavelength (time resolution) of the probe wave vector q is a powerful advantage of pulsed-source diffractometers.⁹ The current generation of instruments can generally accumulate sufficient data at 10 to 50 sample orientations over a period of several days to determine structures of moderate complexity. Each sample orientation could require several hours for data collection. Using the enhanced flux of SNS, increasing the detector coverage, and employing focusing optics should reduce data collection times in most cases to a matter of minutes. Perhaps most importantly, the vastly increased flux on sample will make possible measurements on smaller samples and more complicated structures. In addition, the ease of carrying out parametric studies investigating structural changes as a function of temperature, pressure, etc., is expected to approach that for powder experiments. To collect data on large atomic/molecular structures, it will be important to use focusing optics to capture as many neutrons as possible to enhance the flux on sample.

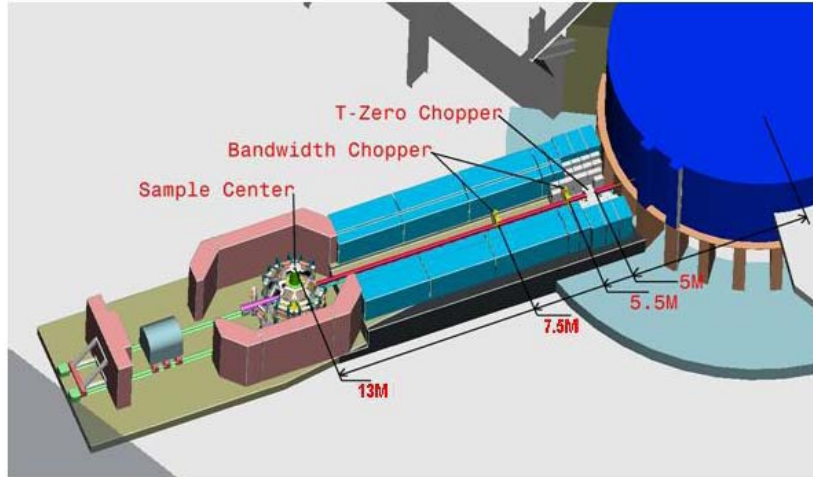


Fig. 4.1. Schematic view of the SNS SCD. Three choppers are shown positioned 5.0, 5.5, and 7.5 m from the source. The T_0 chopper at 5.0 m conditions the incident beam and can be set to cut out the epithermal neutron flux at wavelengths from 0.2 to 0.5 Å and below. This is followed by bandwidth choppers at 5.5 and 7.5 m. The sample chamber is accessible from the top for loading and unloading samples and for positioning sample chambers. The shielding behind the beam stop and the beam stop itself are on casters to permit easy access for maintenance.

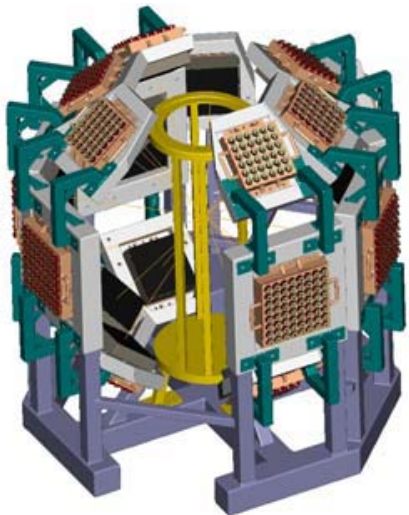


Fig. 4.2a.

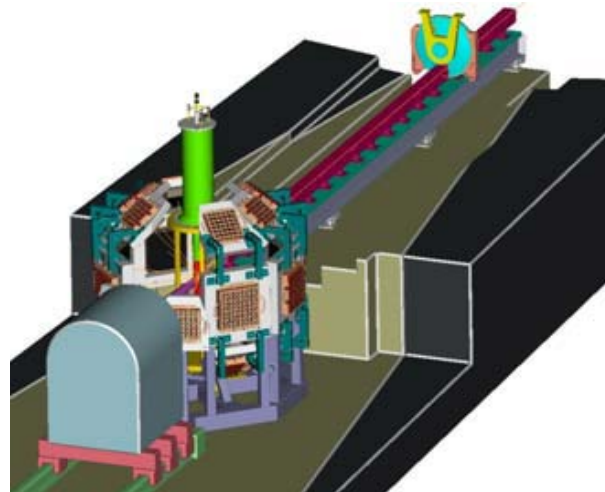


Fig. 4.2b.

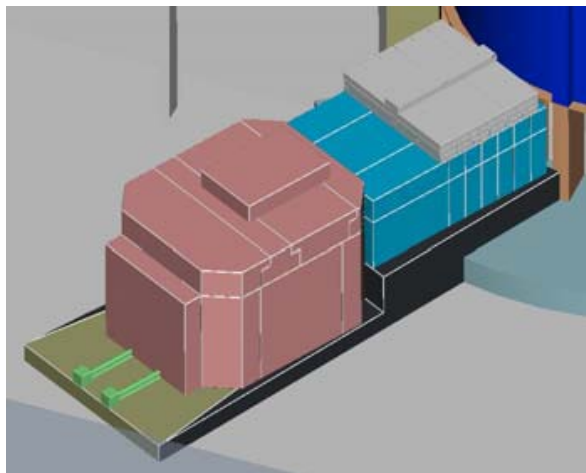


Fig. 4.2c.

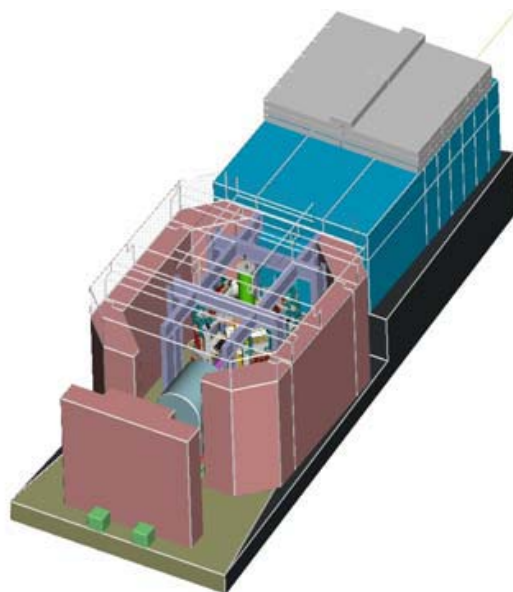


Fig. 4.2d.

Fig. 4.2. Figures 4.2a through 4.2d show further instrument details. The proposed detector mounting frame with detectors (4.2a); the instrument viewed along the beam line with beam stop (4.2b); instrument shielding options with top loading of the sample environment and samples (4.2c and 4.2d). Lifting the top shielding blocks will also give the option of lifting the entire detector array frame for maintenance.

The SNS SCD instrument shown in Figs. 4.1 and 4.2, and with parameters as summarized in Table 4.1, exhibits the following features:

1. The SNS SCD is a general-purpose, single-crystal diffractometer for rapid data collection on small samples.
2. The instrument views a parahydrogen poisoned, decoupled moderator, with an overall neutron flight path of $l_{MD} = 13$ m and with $\delta t / t \sim 0.003$, which places a lower limit on $\delta d / d$.
3. The primary flight path from the source to the sample position is currently 12 m. For resolution gains, the primary flight path length could be extended up to 20 m.
4. A doubly tapered guide is used to provide a maximum incident-beam divergence of $\delta\theta_i = 1.6^\circ$ FWHM for $\lambda \geq 1.5$ Å. Absorbing apertures will be available to reduce this divergence as needed.
5. A portion of the guide segment upstream from the detector array frame (1–2 m) will be removable for insertion of focusing optics.
6. Area-detector coverage exceeds 50%, on a sphere of radius 1 m, with an opening at the top for the insertion of magnets, cryostats, etc. Detector spatial resolution is targeted for 1 mm. The exact number of detectors remains to be determined, based on the sizes and shapes that become available.
7. The large sample-detector distance l_{SD} ensures that scintillation-detector photomultiplier tubes are not adversely affected by magnetic fields applied at the sample position.
8. The sample goniometer has ω and χ motions to enable complete coverage of reciprocal space and access for magnets, furnaces, and cryostats.
9. A portion of the guide segment upstream from the detector array frame (1–2 m) will be removable for insertion of focusing optics.
10. Although the feasibility of implementing this option is still under evaluation, space is available for insertion of a chopper in the incident beam for energy analysis of thermal-diffuse scattering.
11. Typical total data collection times are expected to be on the order of a few hours or less for samples of moderate complexity.

Table 4.1. SNS SCD instrument parameters

Component	Parameter	Value
Moderator	Beam line	tu_12
	Moderator	Liquid-H ₂ , decoupled, poisoned
Pulse width	FWHM	7 μ s at 1 \AA
Geometry	Source sample	12.0 m
	Sample detector	1.0 m
T ₀ chopper	Type	Horizontal axis
	Radius to beam center	250 mm
	Length	300 mm
	Distance from moderator	5.0 m
	Frequency	60 Hz
	Beam width at chopper	71 mm
	Wavelength range to open or close	0.30 \AA @ 60 Hz
Incident beam polarizer	TBD	
Bandwidth chopper 1	Type	Disk
	Radius to beam center	250 mm
	Length	10 mm
	Distance from moderator	5.5 m
	Frequency	60 Hz
Bandwidth chopper 2	Beam width at chopper	70.6 mm
	Type	Disk
	Radius to beam center	250 mm
	Length	10 mm
	Distance from moderator	7.5 m
Fermi chopper	Frequency	60 Hz
	Beam width at chopper	67 mm
	Wavelength range to open or close	0.28 \AA @ 60 Hz
	TBD	
First guide segment	Tapered guide	4 θ_c^{Ni} coating
	Distance from moderator	2.5 m $\leq l \leq$ 5.0 m
	Initial aperture	100 \times 120 mm ²
Second guide segment	Final aperture	71 \times 84 mm ²
	Tapered guide	4 θ_c^{Ni} coating
	Distance from moderator	5.7 m $\leq l \leq$ 7.5 m
Third guide segment	Initial aperture	68 \times 79 mm ²
	Final aperture	56 \times 64 mm ²
	Tapered guide	4 θ_c^{Ni} coating
Collimation and beam line	Distance from moderator	7.7 m $\leq l \leq$ 11.0 m
	Initial aperture	55 \times 63 mm ²
	Final aperture	30 \times 30 mm ²
Beam-line shielding	Upstream ($l < 2.5$ m)	Standard apertures
	Before sample	Variable apertures
	Beam line ($l < 4.5$ m)	He-filled tube
	Beam line ($l \geq 4.5$ m)	Evacuated $< 10^{-2}$ Torr
Beam stop	Steel radial thickness around beam	0.7 m
	Paraffin radial thickness around steel	0.2 m
	Channel for guide	200 \times 220 mm ²
Sample	Length	3.0 m
	Steel	1.6 \times 1.6 \times 2.6 m ³
	Paraffin radial thickness around steel	0.2 m
Position-sensitive detector	Reentrant hole in steel	0.2 \times 0.2 \times 0.5 m ³
	Width and height	0.1–3.0 mm
	Type	Scintillation
Data acquisition	Area	TBD
	Distance from sample	1 m
	Position resolution	≤ 1 mm
	Quantity	TBD
Scattering chamber	Standard system	
	Geometry	Shielded room
	Height	TBD
	Width	TBD
Sample chamber	Length	TBD
	Goniometer, external to chamber	2 circle
	Resolution	0.003 FWHM
	δ / t	0.5–1.6° FWHM
	$\delta(2\theta)$	

4.3 PERFORMANCE ESTIMATES AND DESIGN CHOICES

The performance of the IPNS SCD instrument⁹ will be used here as a basis for comparison. SCD has a 9.5-m moderator-sample flight path viewing a $10 \times 10\text{-cm}^2$ liquid-methane moderator with a set of collimating apertures near the sample. The diffracted intensities are collected with a single, 3-mm resolution, position-sensitive detector located 32 cm from the sample and centered on $2\theta = 90^\circ$. The sample is mounted on a four-circle goniometer.

The effect of the increased source flux available at SNS relative to IPNS will be discussed first by taking into account target neutron production, source repetition rate, and $1/r^2$ flux reduction, as indicated in Table 4.2 (see Section 4.4 for additional details).

Table 4.2. Flux ratios for SNS relative to IPNS

Parameter	SNS	IPNS	Ratio
Target neutron production	4.04×10^{15} n/pulse	5.16×10^{13} n/pulse	78
Source frequency	60 Hz	30 Hz	2
Flux reduction	$1/(12.0\text{ m})^2$	$1/(9.5\text{ m})^2$	0.63

The ratios in Table 4.2 combine to yield an approximate gain factor of 100 in flux on sample at SNS. The contribution of guide and focusing systems is not taken into account for this exercise. Comparing the effects of the moderators is more difficult. The pulse shape of the parahydrogen is desirable over that of the methane moderator, as it provides better peak separation and better resolution.¹⁰

To estimate counting times, the factor of 100 is applied to IPNS SCD data collection. In a recent measurement, a full data set was collected from an organic crystal (β -ARAF), of unit cell volume $V_c = 767 \text{ \AA}^3$, using 17 sample orientations and with a total counting time of 136 hours (5.6 days).¹¹ Placing the IPNS instrument at SNS would allow the same data to be collected in 1.36 hours.

Increasing the detector coverage will further enhance instrument performance. The $30 \times 30\text{-cm}^2$ IPNS SCD detector located 32 cm from the sample intercepts about 2% of reciprocal space. In a recent proposal to upgrade the ISIS SXD instrument, the authors claim to be able to collect a full data set in as few as 2 sample orientations by employing 11 detectors with 2π coverage.¹² Adding a comparable array of detectors to SNS SCD yields an additional factor of five, thereby reducing data collection time to 20 min for a crystal such as β -ARAF considered previously.

4.3.1 Choice of Moderator

Moderator choices at the SNS for the single-crystal diffractometer are the ambient water moderator with deep or shallow poisoning or the liquid hydrogen moderator. Simulations of the moderator performance were calculated by E. Iverson¹³ and are shown in Figs. 4.3 through 4.5. The choice of moderator is crucial for the SNS SCD performance, as the peak shape influences the resolution of $\Delta t/t$ and also the spatial resolution. A narrow peak shape is desirable for high-precision, single-crystal diffraction data.

For the SNS SCD, the decoupled poisoned hydrogen moderator was chosen. As can be seen in Fig. 4.3, the FWHM of the hydrogen moderator is narrower than that of the water moderator at wavelengths between 0.5 and 3 \AA , which is where the bulk of Bragg diffraction data for most experiments will be obtained. The total intensity, though, is lower than that of the decoupled poisoned water moderator with deep or shallow poisoning depth (Figs. 4.44a-c). The maximum peak flux for the hydrogen moderator is at 2.8 \AA , rather than 1.3 \AA for the ambient water moderator, which will benefit

magnetic and diffuse scattering experiments. The peak time widths in Fig. 4.5 also show favorable hydrogen moderator behavior. Because of these considerations, beam line tu_12 at the hydrogen moderator was chosen for the SNS-SCD. (The characteristics of beam line tu_12 are very similar to those of tu_02, for which our simulations were performed.)

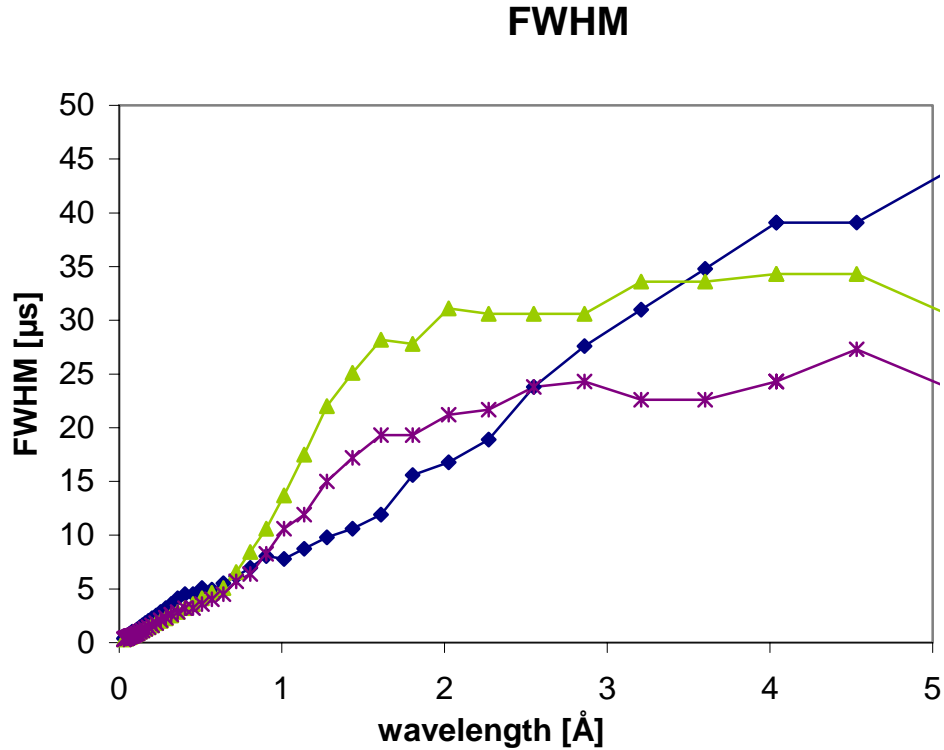


Fig. 4.3. FWHM for the hydrogen moderator (blue), the water moderator face with deep poisoning (green), and the water moderator face with shallow poisoning (red). The hydrogen moderator shows a narrower FWHM in the region between 1 and 3 Å, where the water moderator FWHM jumps considerably. This will be important for magnetic and diffuse scattering measurements and for larger structures.

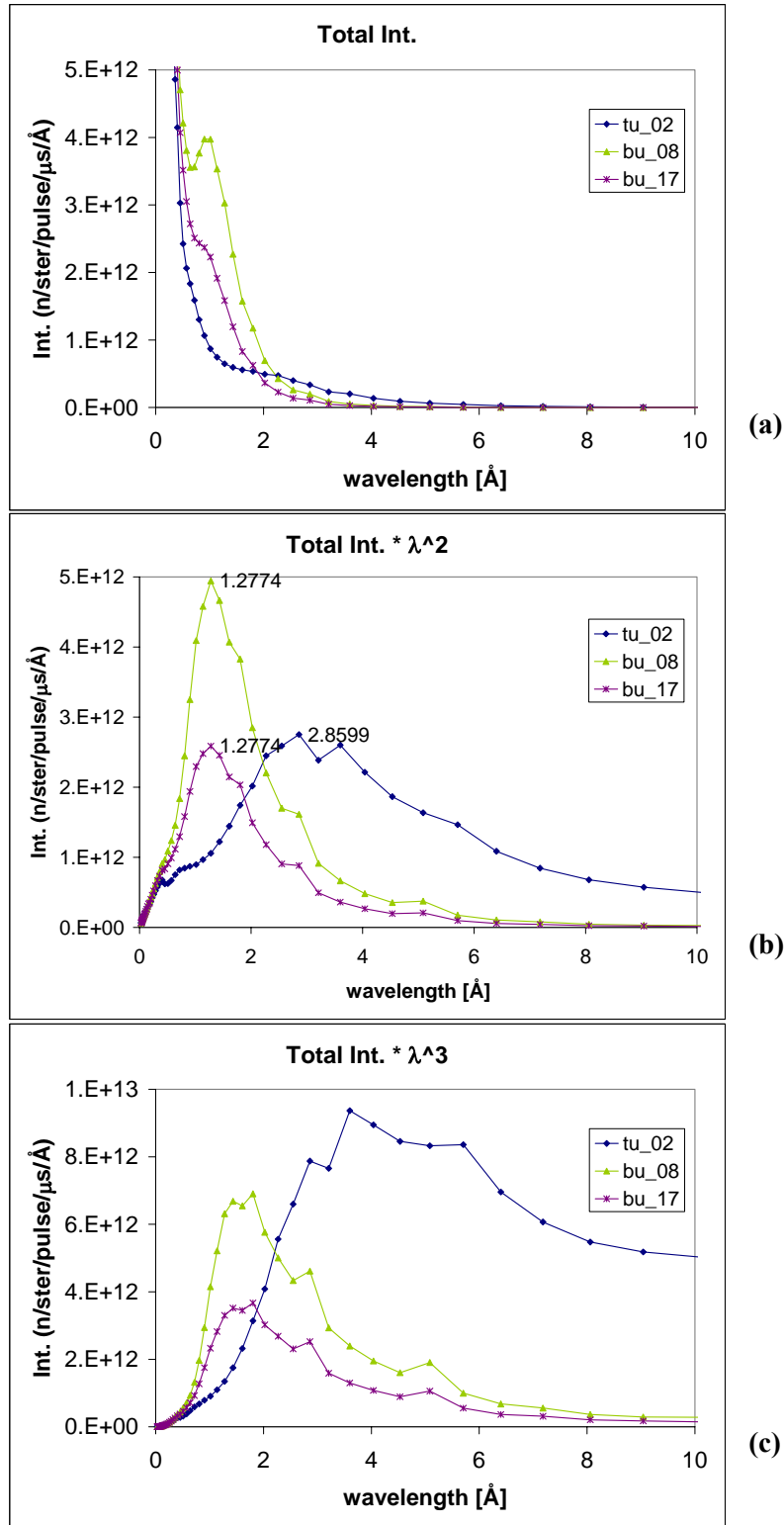


Fig. 4.4. Simulated total peak flux intensity: (a) intensity $\times \lambda^2$, (b) intensity $\times \lambda^3$, and (c) for the hydrogen and the two water moderator faces.

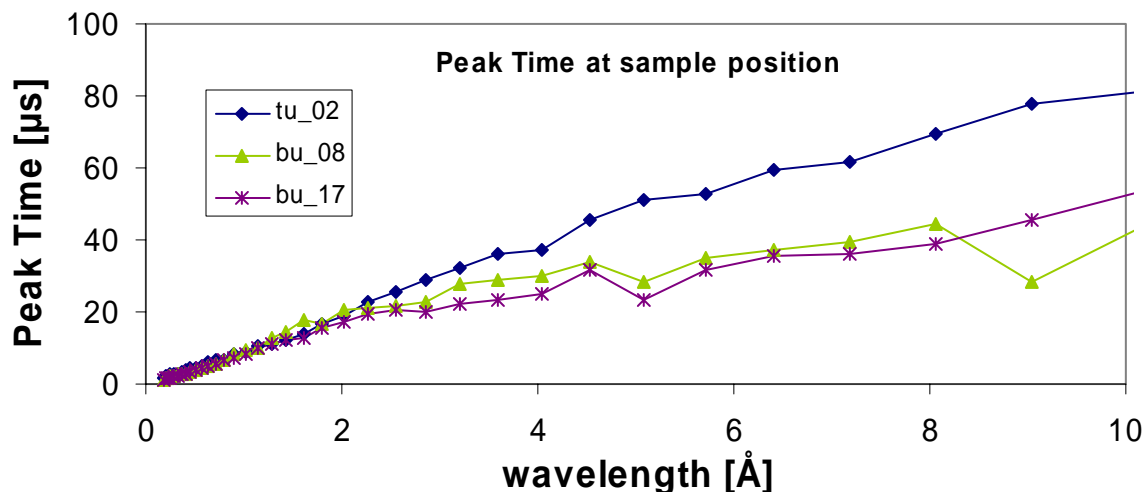


Fig. 4.5. The peak time-width comparison shows a favorable profile for the hydrogen moderator, increasing linearly with wavelength.

4.3.2 Beam Guide or Beam Tube

The SNS SCD has a rather short incident flight path, to preserve maximum flux, and a wide wavelength band in the first frame desirable for Laue diffraction measurements. The gains to be expected from a supermirror guide with a reflectivity of $m = 4$ have been calculated analytically, and a flux gain is predicted for wavelengths above 0.7 \AA (see Section 4.5 for details).

4.3.3 Chopper Arrangement

The incident beam is conditioned using a T_0 chopper to cut off the epithermal neutron flux at wavelengths from 0.2 to 0.5 \AA and below, depending upon the experimental setup and data collection requirements. A beam bender was not considered here since, having a fixed bending radius, it would provide no flexibility for different measurement setups. The T_0 chopper is currently placed close to the source at 5.0 m (see also Section 4.6 for time distance diagrams for the first and second frames).

4.3.4 Inelastic Discrimination Through Beam Conditioning

For most experiments to be carried out at the SNS SCD, the fully elastic scattering is of primary interest. In the case of Bragg scattering, the integrated intensity is high compared with the inelastic background, which therefore is not of major concern. The major contributions of inelastic scattering lie in the diffuse scattering component. These include thermal diffuse scattering (TDS) and kinetically induced inelastic diffuse scattering. To distinguish the elastic and inelastic scattering contributions experimentally, beam conditioning with velocity selective additions as implemented on inelastic spectrometers can be used. Velocity selective beam conditioning with choppers leaves a number of options to be explored:

1. High speed counter-rotating disc chopper.
2. Fermi chopper.
3. Correlation chopper or statistical chopper.

The chopper options for detailed energy analysis to distinguish between elastic and inelastic contributions to the total scattering intensity will be discussed in a separate document. Generally, it can be

noted that crude energy discrimination with the three mentioned options is possible at the cost of flux and therefore measurement time.

4.3.5 Instrument Functions and Performance

The spatial resolution requirements of the detectors are calculated from the instrumental resolution function, derived from Bragg's law using the Gaussian approximation.

$$\begin{aligned} \frac{\delta d}{d} &\approx \sqrt{\left(\frac{\delta\lambda}{\lambda}\right)^2 + \left[\frac{1}{2}\cot(2\theta/2)\delta(2\theta)\right]^2} \\ &\approx \sqrt{\left(\frac{\delta t}{t}\right)^2 + \left[\left(\frac{\delta\theta_i}{2}\right)^2 + \left(\frac{w_D}{2l_{SD}}\right)^2\right]\cot^2(2\theta/2)}, \end{aligned} \quad 4.1$$

where the second line expresses the equivalence of wavelength and flight-time uncertainty and decomposes $\delta(2\theta)$ into incident angular divergence ($\delta\theta_i$) and detector pixel size (w_D) components; l_{SD} is the sample-detector distance. Rearranging this equation, one can express w_D in terms of the other variables and so determine what pixel size is required to achieve a given $\delta d/d$. For example, Fig. 4.6 shows w_D plotted vs 2θ , for $\delta\theta_i = 0.5^\circ$ and $\delta d/d = 0.005$. The less-stringent requirements on detector pixel size for large 2θ are offset by the increasing density of Bragg spots in this region. In fact, Fig. 4.7 shows that the high-angle performance is considerably increased by decreasing the pixel size. Calculated is the percent increase in resolution in d achieved by decreasing the pixel size. A gain of up to 1.5% in d resolution at $90^\circ 2\theta$ is shown, increasing to 5% gain at $170^\circ 2\theta$, for 0.5 mm as compared with 5-mm pixels (Fig. 4.8). To achieve high-angular resolution, for large structures and for high-accuracy measurements, high pixel resolution at all diffraction angles is therefore required.

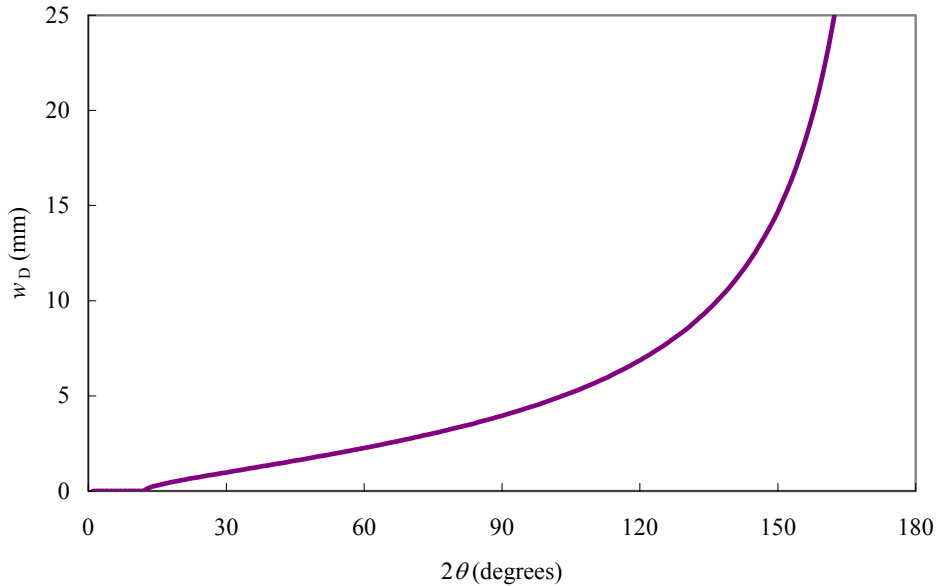


Fig. 4.6. Detector pixel size w_D vs diffraction angle 2θ for incident angular divergence $\delta\theta_i = 0.5^\circ$ and $\delta d/d = 0.005$. Although at relatively large diffraction angles, a given $\delta d/d$ places fewer demands on detector pixel size, the effect is mitigated by the increasing density of Bragg points requiring smaller $\delta d/d$.

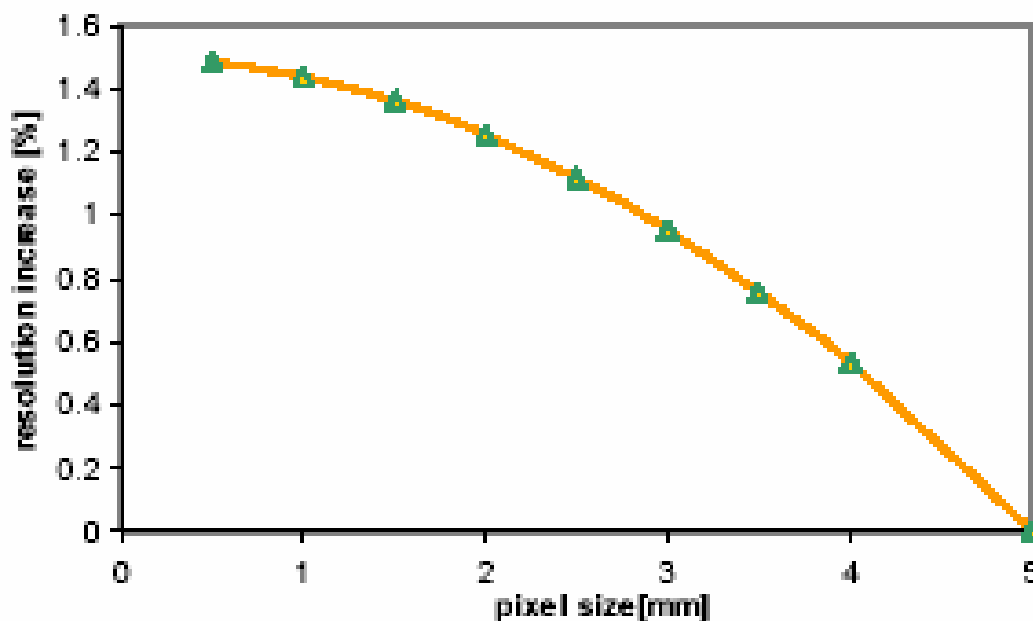


Fig. 4.7. Resolution increase in d for pixel sizes between 0.5 and 5 mm, for $d_{\min} = 0.3 \text{ \AA}$.

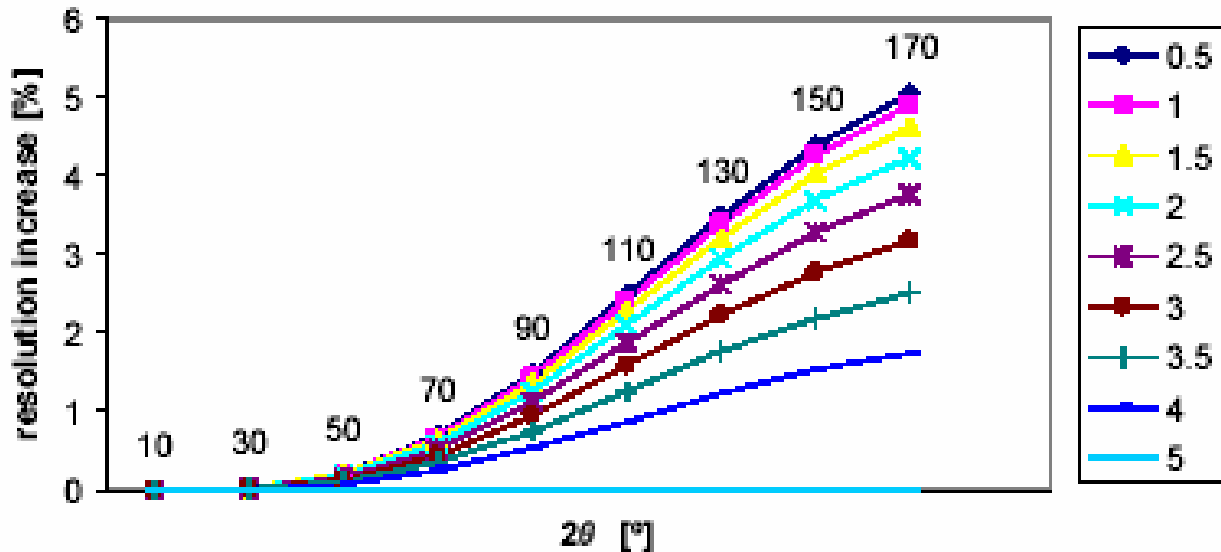


Fig. 4.8. Resolution increase in d , as a function of 2θ , for 0.5-, 1-, 1.5-, 2-, 2.5-, 3-, 3.5-, and 4-mm pixel sizes compared to that for 5-mm pixel size.

The utility of incident-beam focusing depends on the amount of angular divergence that one can tolerate in a given experiment. For example, Fig. 4.9 plots $\delta d/d$ as a function of $2\theta_i$ for $2\theta = 90^\circ$, with $w_D = 1$ -mm detector pixels. In this geometry, $\delta d/d \approx \delta\theta_i/2$, so that 2° (0.035 radian) of incident angular divergence allows better than 2% resolution. The IPNS SCD instrument, viewing a 10-cm source at a distance of 9.5 m, accepts 0.6° of angular divergence, while the SNS SCD, at 12.0 m, accepts less than

0.5°. By replacing the beam tube with a tapered guide coated with $m = 4$ supermirror, we can increase the intensity in both horizontal ($\times 3$) and vertical ($\times 2.5$) directions for $\lambda \geq 1.5 \text{ \AA}$, at the cost of increasing the angular divergence to 1.6° (see Figs. 4.12 and 4.13, Section 4.5 for a treatment of guide gains). Those experiments not requiring resolution better than 1.4% can take full advantage of this added flux.

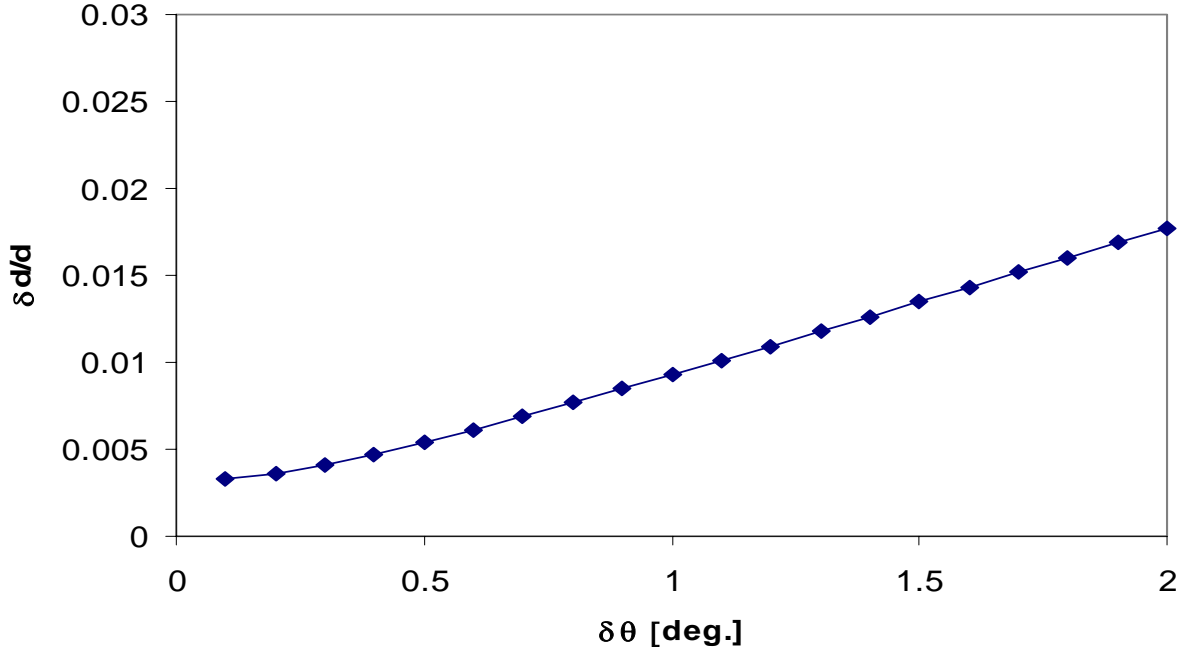


Fig. 4.9. Instrumental resolution $\delta d/d$ plotted vs incident angular divergence $\delta\theta$, assuming $2\theta = 90^\circ$ and detector pixel size $w_D = 1 \text{ mm}$.

To evaluate the suitability of this instrument for large structures, the requirements for a high-resolution data set can be calculated analytically. It was of interest to calculate whether the chosen sample distance, 12 m from the source, is long enough to allow data collection for samples with unit cell sizes of 50 \AA and larger. A cubic unit cell was assumed for the calculations. The reflections along the principal axes (i.e., $h00$) are critical, in the case of both time and spatial resolution. The direct unit-cell dimensions can therefore be used for calculating the resolution.

In detail, the instrumental resolution can be derived by calculating the uncertainty contributions along the \mathbf{Q} vector and its horizontal and vertical components. The instrumental resolution is derived by calculating the relative variance parallel to \mathbf{Q} ($\mathbf{Q}_\parallel = \mathbf{Q}_x$), and in the horizontal (\mathbf{Q}_y) and vertical (\mathbf{Q}_z) directions, and then multiplying this variance by the Gaussian FWHM approximation of $\Delta = 2.355 \sigma$.

It is assumed that the source and the detector resolution can be described by a rectangular distribution. The incident angular divergences (collimation) are α_0, β_0 , and the reflected angular divergences are α_1, β_1 . $\Delta\mathbf{Q}_x/\mathbf{Q}$ can be described as

$$\Delta = k \frac{\sigma_{Q_x}}{Q} = k \sqrt{\left(\frac{\sigma t}{T}\right)^2 + \left(\frac{\left(\frac{\alpha_0^2}{\sqrt{12}} + \frac{\alpha_1^2}{\sqrt{12}}\right)}{4} \cot^2 \theta\right)}, \quad 4.2$$

with

- σt = time uncertainty of the moderator
- T = neutron travel time [$T = 505.6[\mu\text{s}/\text{\AA}] d \sin\theta (L_0+L_1)$]
- L_0 = incident flight path
- L_1 = scattered flight path
- α_0 = incident beam divergence ($\alpha_0 = w_M/L_0$)
- w_M = moderator width
- α_1 = scattered beam divergence ($\alpha_1 = w_D/L_1$)
- w_D = detector pixel size
- k = Gaussian FWHM/ $\sigma = 2.355$

Figure 4.10 shows the maximum resolvable unit-cell repeat at different diffraction angles using the preceding formula. To estimate the maximum resolution, the Gaussian FWHM ($k = 2.355$) was assumed (10a); a more conservative approach uses the Gaussian full width, $k = 5.056$ (10b). Both plots show results for $0.3 \text{ \AA} \leq d_{min} \leq 1.2 \text{ \AA}$.

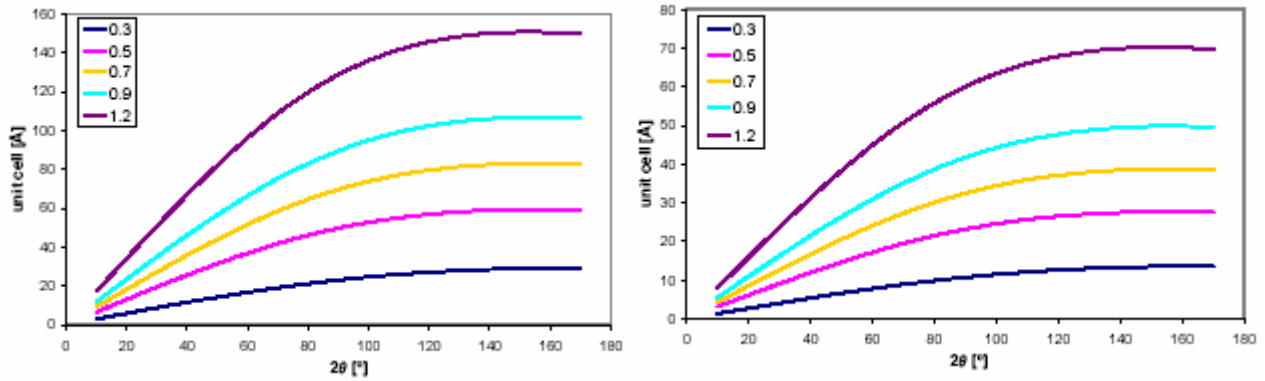


Fig. 4.10. Maximum resolved unit-cell repeat, as a function of diffraction angle 2θ , computed for $d_{min} = 0.3, 0.5, 0.7, 0.9,$ and 1.2 \AA .

Assuming the Gaussian FWHM, the instrument should be capable of resolving unit-cell repeats of more than 100 \AA for d_{min} of 1.2 \AA . Using the conservative approach, assuming the Gaussian full width, unit-cell repeats of up to 70 \AA are resolved for d_{min} of 1.2 \AA .

Extending the instrument comparisons, Table 4.3 considers the two concrete examples of integrating the full peak intensity with a mosaic spread of 0.1° , λ_{min} values of 1.5 and 2 \AA , and d_{min} of 0.9 and 1.2 \AA , at a scattering angle 2θ of 56° , to obtain the maximum unit-cell repeats that can be separated under these assumptions on the single-crystal diffractometers at ISIS, IPNS, and SNS. In both examples, the maximum resolvable repeat at SNS will be more than double those calculated for the instruments at ISIS and IPNS. Figure 4.11 compares the maximum resolvable unit-cell repeats for the SNS SCD with ISIS SXD and IPNS SCD at $2\theta = 90^\circ$ and shows that the SNS SCD will have at least twice the resolving power of the other two instruments for d_{min} values above 0.6 \AA .

Table 4.3. Comparison of the ISIS, IPNS, and SNS instruments. The SNS SCD will benefit from its sharper moderator peak and will resolve considerably larger unit-cell repeats.

		ISIS	IPNS	SNS
Inc. beam [L_0]	(m)	8	9.5	12
Diffracted beam [L_1]	(m)	0.5	0.32	1
Det. resolution [w_D]	(mm)	2	3	1
Moderator width [w_M]	(cm)	10	10	10
Largest unit cell resolved {mosaic = 0.1° , $\lambda_{\min}=1.5\text{\AA}$, $d_{\min}=0.9$, $\theta=56^\circ$ }	(\AA)	20	23	53
Largest unit cell resolved {mosaic = 0.1° , $\lambda[\min]=2\text{\AA}$, $d[\min]=1.2$, $\theta=56^\circ$ }	(\AA)	34	39	92

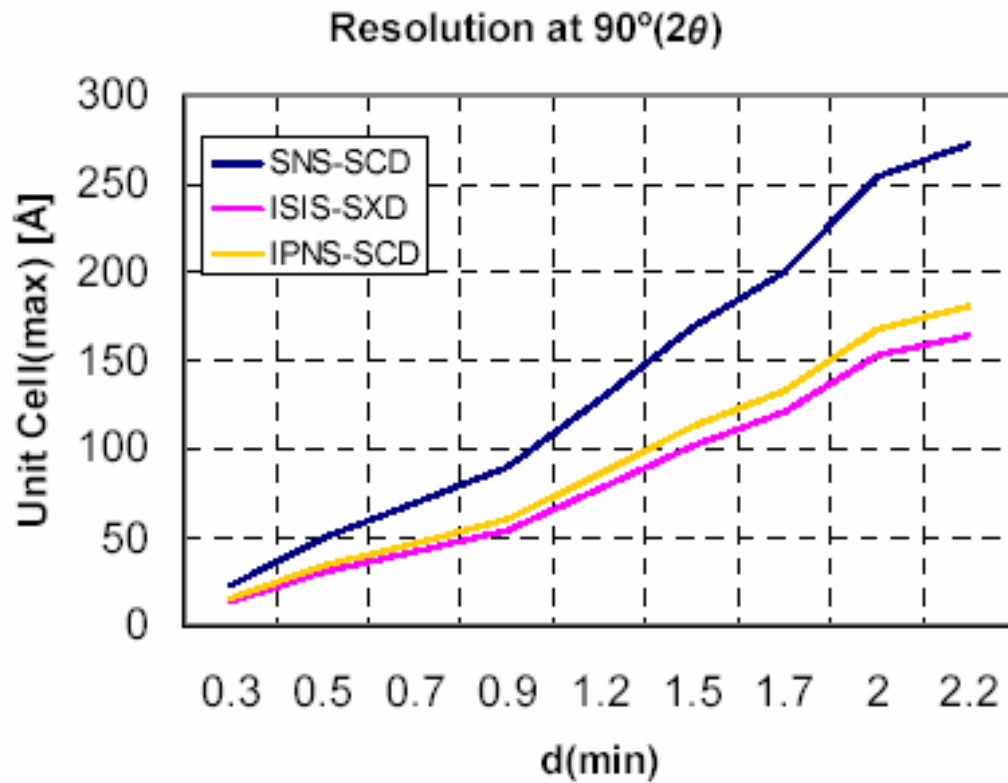


Fig. 4.11. Comparison of maximum resolvable unit-cell repeats for the SNS SCD with ISIS SXD and IPNS SCD at $2\theta = 90^\circ$.

The expected data collection time is also an important factor in the evaluation of the SNS SCD performance. The time required to collect a high-resolution data set is a critical limiting factor at all currently existing neutron sources. Table 4.4 compares the data collection times estimated assuming $d_{\min} = 1.2\text{\AA}$, and an average interplanar spacing of $d = 1.6\text{\AA}$, for unit-cell repeats spanning a range of 5 to 100 \AA in one base vector direction of a cubic unit cell. The desired intensity precision is taken to be 5%. The

calculations are based on the assumption that the ratio between background and average intensity is derived through

$$\frac{I_{inc}}{\langle I \rangle} \leq 0.5 \frac{d_{min}^3}{d^3} \frac{N_H}{N} \frac{b_{inc}^2}{\langle b^2 \rangle} \exp[B/(2d^2)] . \quad 4.3$$

The estimated measurement time neglecting the background error can be calculated to be

$$t = \frac{1}{\varepsilon^2 I} \frac{1 + I_{inc}}{I} \quad \text{with} \quad \varepsilon = \frac{\sigma(I)}{I} . \quad 4.4$$

The average scattering ratio (N_H/N) is assumed to be 0.4 for an average 50% H/D exchange hydrocarbon sample. B is set to 10 \AA^2 , while the sample mosaic spread is taken to be 0.1° . The number of atoms per unit cell is taken to be 10,000 for a $(50 \text{ \AA})^3$ unit cell and is extrapolated up to the $(100 \text{ \AA})^3$ unit cell and down to the $(5 \text{ \AA})^3$ cell size. ($b_{inc}^2 / \langle b^2 \rangle$) reflects an average scattering strength for a hydrogenous sample.

Table 4.4. Estimated measurement times for hydrogenous samples with unit-cell repeats of 5, 10, 15, 20, 25, 50, 75, 100 \AA

	ISIS-SXD	IPNS-SCD	SNS-SCD
5 \AA , $d = 1.6$, $d_{min} = 1.2$	11 min	1 h	1 min
10 \AA , $d = 1.6$, $d_{min} = 1.2$	1 h	8 h	7 min
15 \AA , $d = 1.6$, $d_{min} = 1.2$	5 h	1 days	24 min
20 \AA , $d = 1.6$, $d_{min} = 1.2$	11 h	3 days	1 h
25 \AA , $d = 1.6$, $d_{min} = 1.2$	22 h	5 days	2 h
50 \AA , $d = 1.6$, $d_{min} = 1.2$	7 days	39 days	15 h
75 \AA , $d = 1.6$, $d_{min} = 1.2$	25 days	133 days	2 days
100 \AA , $d = 1.6$, $d_{min} = 1.2$	58 days	314 days	5 days

The values in Table 4.4 show that data collection times for the SNS SCD are estimated to be about an order of magnitude less than for the ISIS SXD and more than a factor of 50 less than for the IPNS SCD. For example, for a representative chemical crystallography problem with a $(15 \text{ \AA})^3$ cell size, data collection for this resolution at the SNS SCD would be completed in less than 30 min. This type of performance is expected to revolutionize single-crystal neutron diffraction as we know it, especially from the viewpoint of the practicing synthetic chemist.

4.3.6 Further Issues

Several technical developments could impact the performance of the SNS SCD and alter the aforementioned design parameters.

1. The doubly tapered guide proposed here serves as a starting point in considering other focusing devices, such as toroidal mirrors, capillary optics, and refractive lenses. Recent work using X-ray capillary focusing for protein crystallography¹⁴ looks particularly promising, with adequate diffraction spot separation apparently possible even with as much a $2\theta_f = 2^\circ$ divergence. The ability to

study extremely small samples could prove revolutionary. The current design carries the tapered guide to the edge of the detector mounting frame. We envision having the last 1 m be removable to allow the insertion of different optical components.

2. Efforts to design the appropriate beam focusing devices leading to smaller increases in beam divergence are desired. The current focusing devices, such as multicapillary lenses and supermirror-coated bent crystals, impose a large increase on the incident beam divergence.
3. The data rates expected at SNS place great demands on detectors, particularly in terms of count rate. Instantaneous count rates of 1 MHz per panel and 300 kHz per pixel are expected. Such values lie at the outer edge of current scintillator detector capabilities. We must also determine the optimum configuration of detector panels in consultation with the user community. Some preliminary detector arrangement evaluations are presented in Section 4.7.
4. It would be desirable to provide a polarized beam option for the SNS SCD, provided that a suitable beam polarizer becomes available. ³He polarizer technologies appear to be particularly promising and are undergoing rapid development.
5. Reducing the sensitivity of the detectors to magnetic fields would allow reduction of the sample-detector radius, at the cost of increased pixel-resolution requirements. The optimum radius of the detector array must be determined with this constraint in mind.
6. Details of Fermi-chopper operation and placement remain to be worked out, and the user community must be consulted as to its utility.

4.4 RELATIVE FLUX COMPARISON BETWEEN SNS AND IPNS

The following treatment is adapted from work done by K.W. Herwig.

Estimate of target yields is taken from Ref. 15.

$$\begin{aligned} \text{Yield} &= 0.1 (E_{\text{GeV}} - 0.120) (A + 20) && \text{for all non-fissile materials} \\ &= 50.0 (E_{\text{GeV}} - 0.120) && \text{for } ^{238}\text{U} \end{aligned}$$

The expected ratio in neutron yields may then be taken as

$$\begin{aligned} \text{SNS:} & \quad 0.1 (1.0 - 0.120) (200 + 20) = 19.4 \text{ neutrons/proton} \\ & \quad \text{(SNS is a 1 GeV source with a mercury target)} \\ \text{IPNS:} & \quad 50.0 (0.45 - 0.120) = 16.5 \text{ neutrons/proton} \\ & \quad \text{(IPNS is a 450 MeV source with a depleted uranium target)} \end{aligned}$$

The next step is to input the number of protons/pulse.

IPNS uses a 0.015-mA source with a repetition rate of 30 Hz and so has

$$(0.015 \times 10^{-3} \text{ A}) (1 \text{ proton}/1.6 \times 10^{-19} \text{ C}) (1/30 \text{ s}) = 3.125 \times 10^{12} \text{ protons/pulse}$$

Then

$$\begin{aligned} (16.5 \text{ neutrons/proton})(3.125 \times 10^{12} \text{ protons/pulse}) &= 5.16 \times 10^{13} \text{ neutrons/pulse} \\ \text{equivalent proton power on target} &= (450 \times 10^6 \text{ eV})(1.6 \times 10^{-19} \text{ J/eV})(0.015 \times 10^{-3} \text{ A}) \\ & \quad (1 \text{ proton}/1.6 \times 10^{-19} \text{ C}) = 6.75 \text{ kW} \end{aligned}$$

SNS will use a 2-mA source with a repetition rate of 60 Hz and so has

$$(2 \times 10^{-3} \text{ A}) (1 \text{ proton}/1.6 \times 10^{-19} \text{ C}) (1/60 \text{ s}) = 2.084 \times 10^{14} \text{ protons/pulse}$$

Then

$$(19.4 \text{ neutrons/proton})(2.084 \times 10^{14} \text{ protons/pulse}) = 4.04 \times 10^{15} \text{ neutrons/pulse}$$

$$\begin{aligned} \text{equivalent proton power on target} &= (1.0 \times 10^9 \text{ eV})(1.6 \times 10^{-19} \text{ J/eV})(2 \times 10^{-3} \text{ A}) \\ &(1 \text{ proton}/1.6 \times 10^{-19} \text{ C}) = 2 \text{ MW} \end{aligned}$$

4.5 GUIDE GAINS

We have modeled optical components and determined guide gains using acceptance diagrams^{16,17} implemented on Excel spreadsheets. The acceptance diagram plots the neutron spatial coordinate x vs angular divergence γ , giving a phase-space picture of neutron flux through various optical components. Figure 4.12 shows the horizontal acceptance diagram for a 2.5-m, 10-cm aperture viewing the moderator, with neutrons passing into an 8.5-m-long guide ($4\theta_c^{Ni}$) that tapers from a 10- to a 3-cm aperture. The beam exits the guide, travels 1 m and strikes a 1-mm sample. The interior of the red rectangle represents the population of neutrons striking the sample that have not been reflected from the walls of the tapered guide. The interior coordinates of the orange polygons describe neutrons that bounced once in the guide. The areas of these polygons are proportional to the neutron flux. In return for a bit more than a factor of three increases in angular divergence, one gains a factor of three in flux on sample. We achieve a factor of 2.5 increases in flux from vertical focusing, for a net gain of 7.5 for $\lambda \geq 1.5 \text{ \AA}$. The wavelength dependence of the guide gain is plotted in Fig. 4.13.

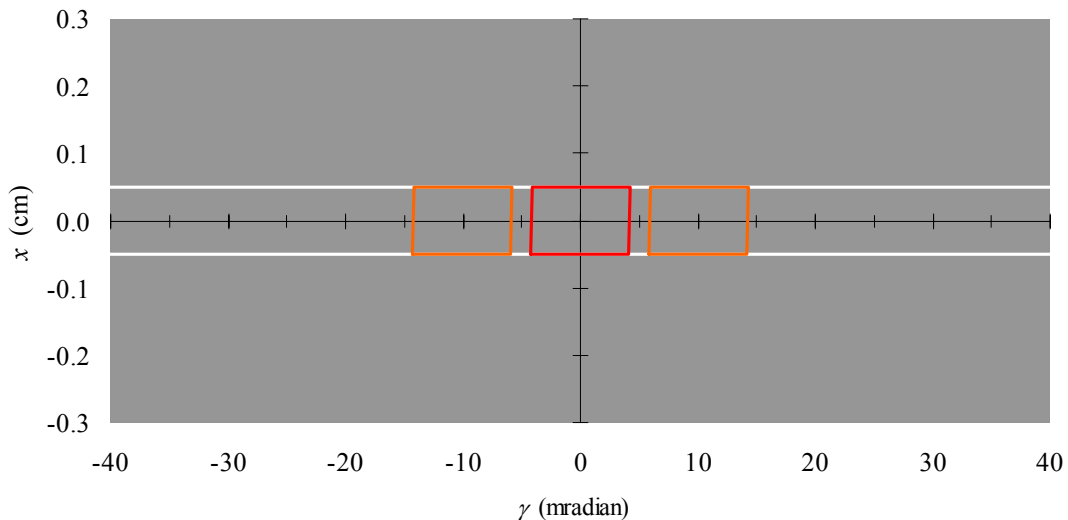


Fig. 4.12. Acceptance diagram for 1.5-Å neutrons incident on a 1-mm sample from a tapered 40_c^{Ni} guide. The red area represents neutrons not striking the guide wall, while neutrons within the orange areas (centered on 10 mradian) have bounced once. Flux is proportional to enclosed area, so the guide produces a factor of three improvements in flux on sample, at the cost of about a factor of three increases in angular divergence.

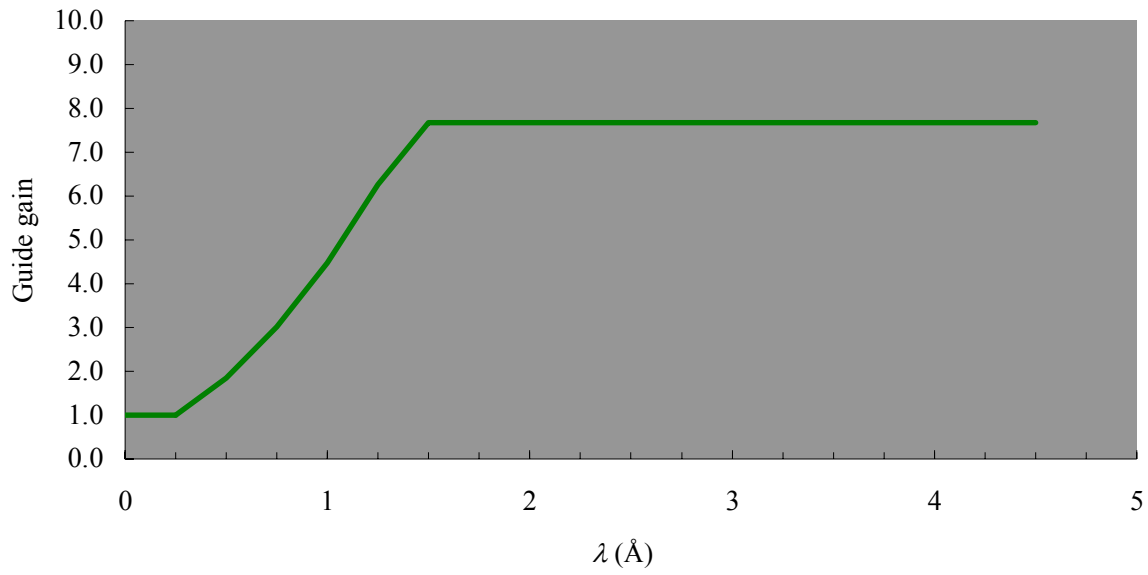


Fig. 4.13. Gain from a doubly tapered guide (rectangular funnel) for intensity on 1- mm^2 sample. The gain is constant at about 7.5 for $\lambda \geq 1.5 \text{ \AA}$.

4.6 TIME-DISTANCE DIAGRAMS FOR CHOPPER CHOICES

A number of choppers are required to define the frame width for a collected data set and to avoid frame overlap. A set of three choppers is proposed here: A T_0 chopper for frame definition at 5 m from the source, followed by a bandwidth chopper at 5.5 m (T1) and a second bandwidth chopper at 7.5 m (T2). Chopper timing diagrams for the first and second frame are shown in Fig. 4.14. Chopper settings are calculated for 60 Hz. Two bandwidth choppers are used—the second chopper serves to stop neutrons that are able to pass through the first chopper.

Preliminary optimizations of the chopper locations and settings were done on spreadsheets to determine the opening and closing times and to select the wavelengths that are passing through one or more choppers while open.

The ability to vary the chopper opening and closing times, and therefore the wavelengths and the bandwidth, gives the instrument increased versatility and makes it possible to tune to specific wavelengths for different samples and materials.

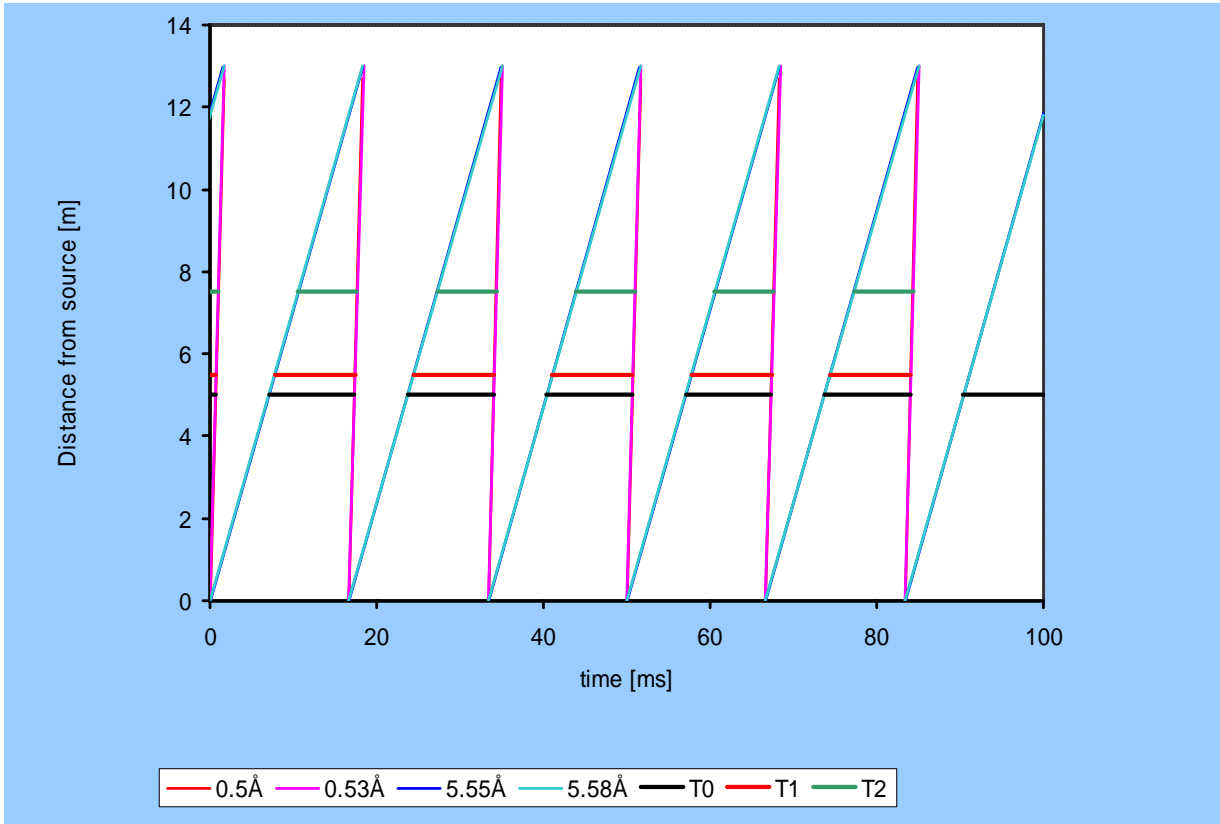


Fig. 4.14a. Time-distance diagram for the first frame (0.5–5.07 Å).

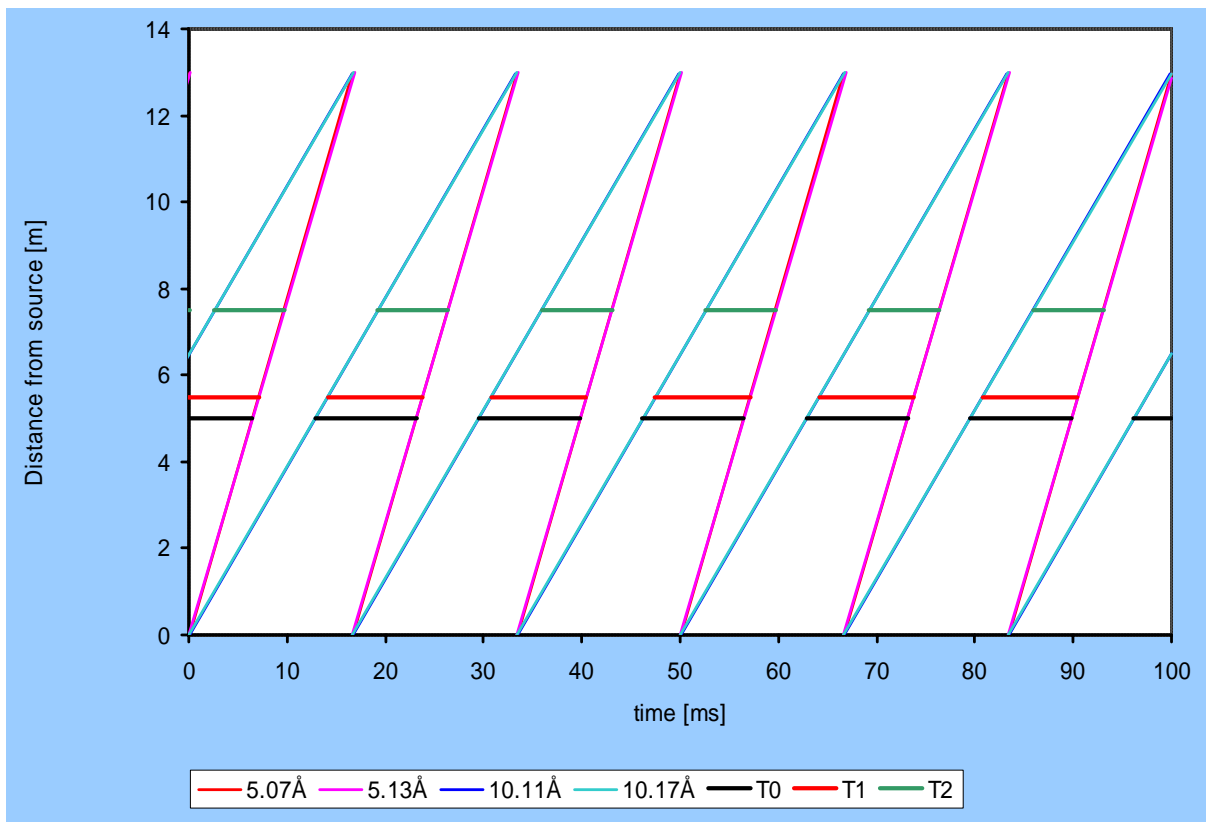


Fig. 4.14b. Time-distance diagrams for the second frame (5.07–10.14 Å).

4.7 PRELIMINARY DETECTOR ARRANGEMENT EVALUATIONS

A major goal of the SNS SCD will be to measure full diffraction data sets in minutes. To achieve short data collection times, the number of settings, or rotations about a goniometer axis to sample different scattering directions, needs to be minimized. This can be achieved by maximizing the detector coverage, which will add to the instrument cost but will also considerably increase the throughput. Preliminary calculations to evaluate measurement times were performed using the Ewald2 program.¹⁸ The current IPNS SCD setup was chosen as a baseline for the calculations. Here, the single 30- × 30-cm² detector is positioned in the horizontal plane, at a distance of 32 cm from the sample, centered at $2\theta = 90^\circ$. This arrangement provides 2% coverage of reciprocal space. For a sample with low symmetry, 44 crystal settings are necessary to collect a complete data set. For each setting, approximately 4 h of counting time is needed, adding up to 176 h (7.3 d) for a complete data collection. Figure 4.15 shows the 44 different crystal settings.

Using three 2D detectors of the same dimensions, the number of settings is reduced from 44 to 7 (Fig. 4.16). The time required to measure a complete data set would thus be reduced from 176 to 28 h (1.2 d).

If the detector coverage is expanded to ten 2D detectors, three crystal settings would suffice for a complete data set. In this event, a measurement would require only 12 h to complete on IPNS SCD (see Fig. 4.17).

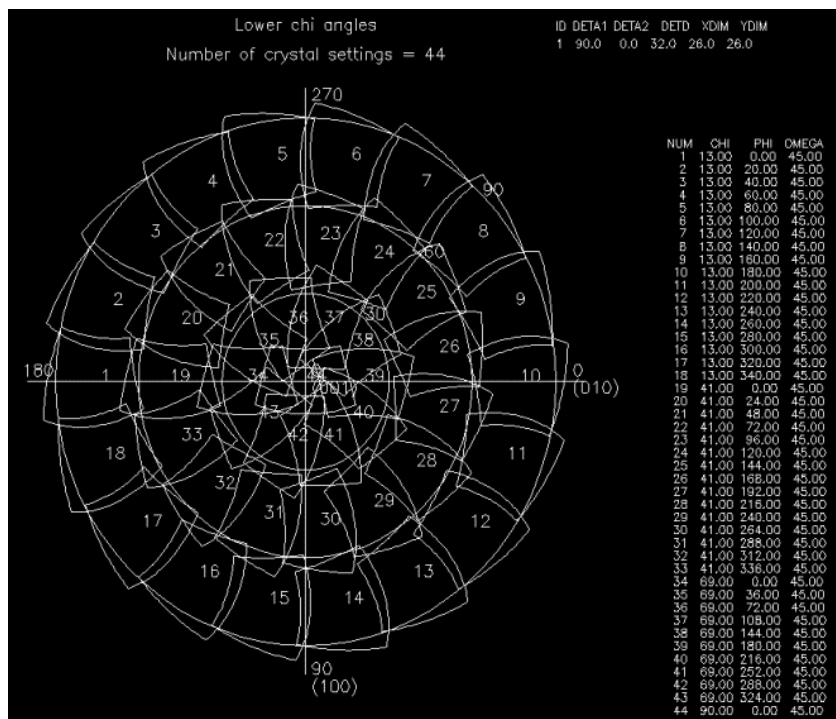


Fig. 4.15. The 44 crystal settings required to measure a full set of diffraction data on IPNS SCD.

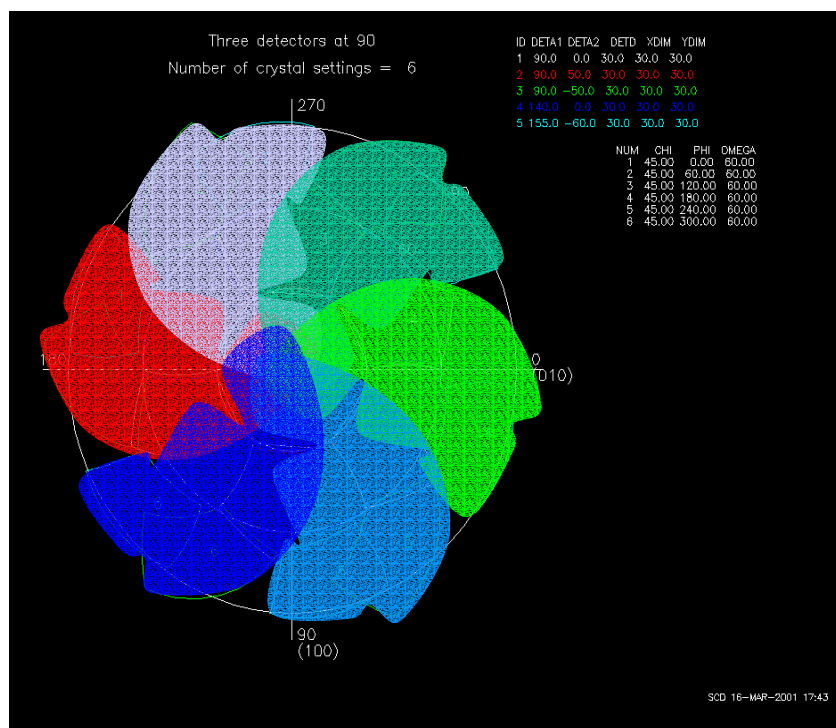


Fig. 4.16. The seven crystal settings that would be required on IPNS SCD with three 2D detectors.

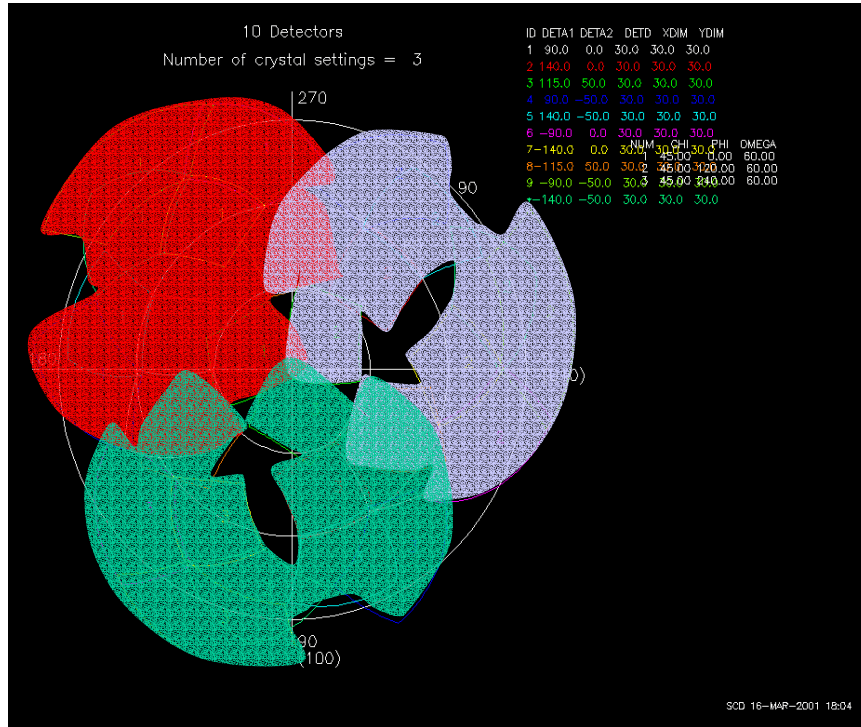


Fig. 4.17. Ten 2D detectors can shorten the measurement time from 44 to three settings. The measurement would be finished in 12 h.

The desired design parameters for the SNS SCD detectors chosen are shown in Table 4.5.

Table 4.5. Detector design parameters

Spatial pixel area (mm ²)	1
Total no. of pixels	5,000,000
Time of flight precision (μ s)	1
Max. instantaneous (rate/pixel)	3.8×10^4
Total no. of channels per data set	5×10^9

5. DISORDERED MATERIALS DIFFRACTOMETER (NOMAD)

5.1 NOMAD INSTRUMENT OVERVIEW

Design features to be developed for NOMAD will enable the broadest range of science on nanoscale and locally ordered systems, as outlined previously. It is fully expected that science needs will direct instrument design, and extensive additional input from the user community is anticipated through the conceptual design, review, and engineering process. In this section, we outline the general instrument parameters that have been developed based on the scientific needs of the user community and that have been reviewed by the SNS EFAC in tentatively assigning a beam line for NOMAD. It is recognized that additional details will be added, and final instrument configurations will change, during the design and review process. Additional details on the instrument features outlined in this section are available in a recent SNS report.¹⁹

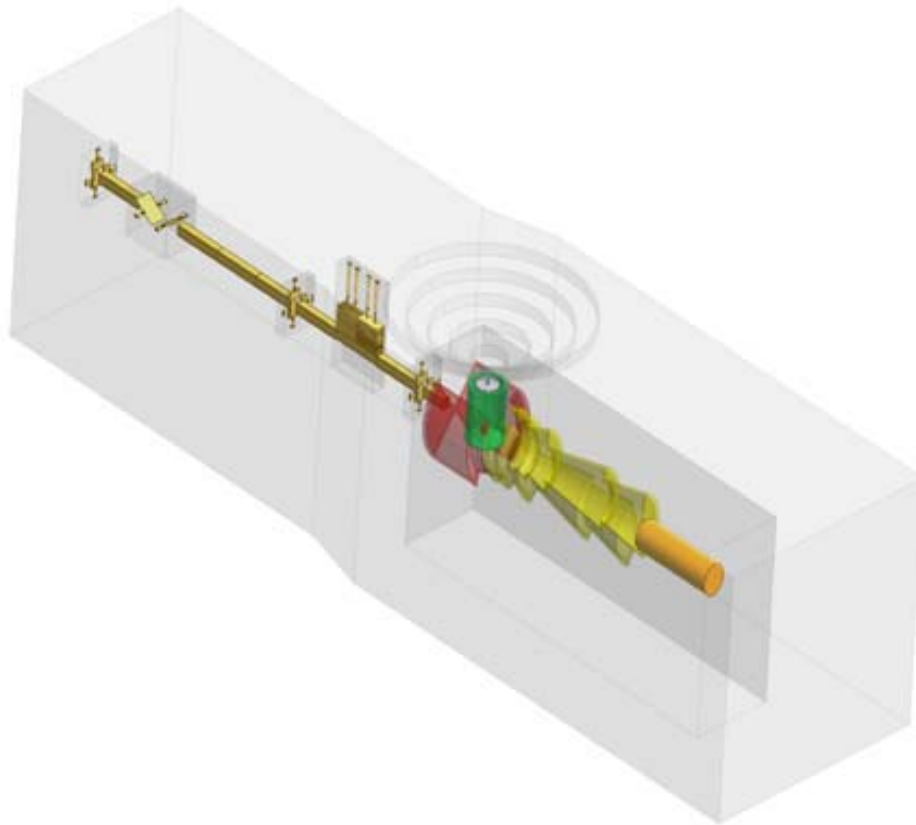


Fig. 5.1. Overall view of NOMAD, showing extensive detector coverage (red and yellow) around the sample position (green).

General features of NOMAD that are critical to its performance include the following:

- **High intensity.** A number of systems (e.g., biological and some polymeric molecules; NDIS for solutions with low concentrations, and/or small differences in scattering length) have inherently low contrast in scattering or depend on small differences in scattering between “matched” samples. In addition, the best use of NOMAD for investigation of new nanomaterials by neutron scattering will, particularly at the outset, involve experiments on rare and/or expensive samples. Minimizing sample volume will be important for these experiments, and coupling the inherently high flux of the SNS with optimal instrument capabilities will permit high-quality results to be obtained from small samples.
- **High stability.** As with intensity considerations, low-contrast samples, difference experiments, and small sample sizes will require extended measurement of scattering from individual samples in order to attain reliable statistics for extracting structure from scattering data.
- **Minimized, consistent background.** Pushing the limits of the science enabled by NOMAD will require careful consideration to give low and stable background readings with a wide range of sample environments.

5.2 INCIDENT BEAM CONSIDERATIONS

The needs of the science are clear in the choice of moderator for NOMAD. Good resolution in high-angle and backscattering detector banks is needed for studies of local disorder in crystalline materials and for investigation of nanoparticulate crystalline systems. This requirement precludes the use of the coupled hydrogen moderator because of its long pulse time and concomitant low timing resolution. For studies of systems with light atoms (e.g., hydrogenous liquids and polymers), corrections for inelastic scattering are simplified by considering a large range of scattering vector attained by scattering relatively short-wavelength neutrons through a small scattering angle. It has also been noted that cooled moderators provide an increased region of useful wavelengths as compared with ambient-temperature moderators.²⁰ Investigation of nanoscale structures in disordered materials (e.g., polymeric species in solution) depends on the availability of usable flux of longer-wavelength neutrons in the moderator spectrum. For such studies, the poisoned decoupled hydrogen moderator has significant advantages over a water moderator, as shown in Fig. 5.2. Finally, overall neutron beam stability can be expected to be improved through the use of a cooled moderator as compared with one subject to changes in ambient temperature. For its resolution, stability, and high flux over a wide range of neutron wavelength, the poisoned decoupled hydrogen moderator is the clear choice for NOMAD. The recommendations of EFAC and space considerations within the target building have led to a tentative location of NOMAD on beam line 1.

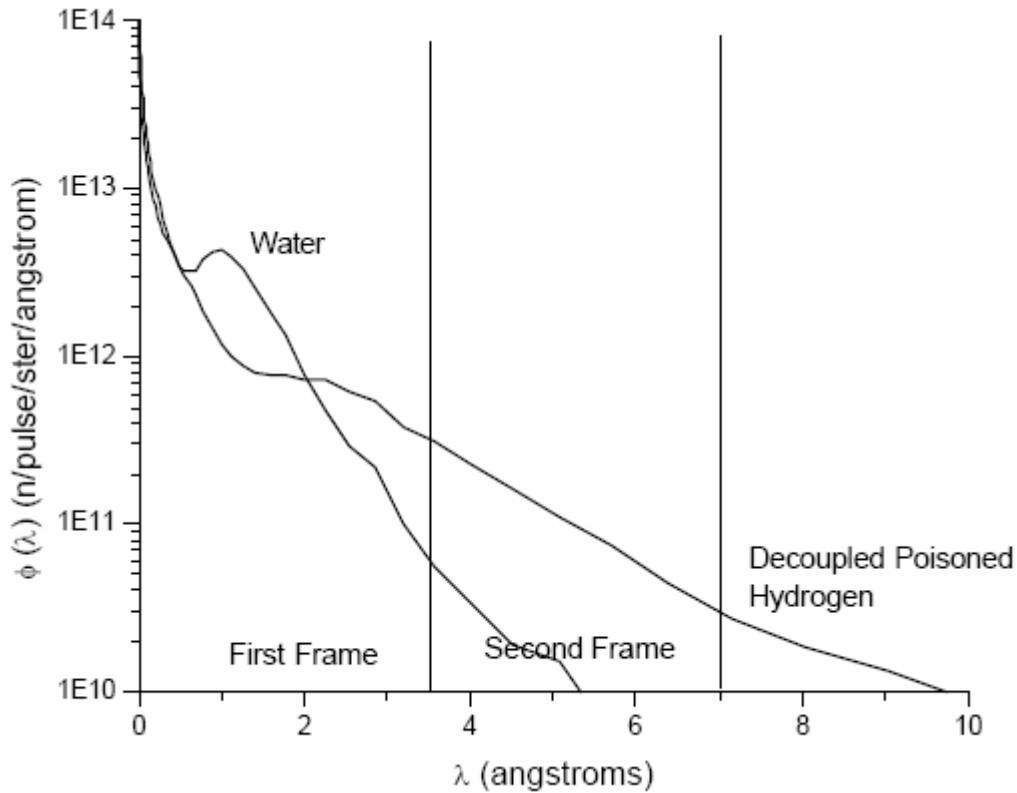


Fig. 5.2. Flux characteristics of water and decoupled poisoned hydrogen moderators at SNS.

To accommodate the anticipated wide range of sample configurations and environments as outlined in previous sections, the current design concept calls for the inclusion of a series of continuously variable jaws spaced along the beam line, defining a rectangular beam of variable geometry. Operating at 60 Hz with a short total flight path creates frame overlap at $\lambda = 3.5 \text{ \AA}$ in the low-angle detector banks and at $\lambda = 3.98 \text{ \AA}$ in the 90° and backscattering detector banks. Frame overlap (or bandwidth) choppers are needed to extend the range of momentum transfer and decrease background, as needed for investigation of nanoscale features and low-contrast samples. It is anticipated that at least two frame overlap choppers will be incorporated into the instrument. For choppers located 6 and 11 m from the moderator, the first contamination from longer-wavelength neutrons occurs for $12.3 < \lambda/\text{\AA} < 14.8$ when operating in the first frame and for $15.2 < \lambda/\text{\AA} < 17.5$ when operating in the second frame. Long-wavelength neutrons in the second frame will extend the accessible range of scattering vector to $Q \approx 0.015 \text{ \AA}^{-1}$. Current plans include a T_0 chopper at 12 m from the moderator to reduce background scattering from the prompt neutron pulse. It is noted that this chopper will not be used for all experiments, particularly for those which need coverage of a wide range of scattering vector at low scattering angles.

Given the importance of high intensity (high flux of neutrons on the sample), both the position of the sample relative to the moderator and the use of guides have been considered. The sample position currently under consideration is at 15 m from the moderator. This position is essentially as close to the moderator as possible, allowing for the size of the shielding monolith and the requirements for incident beam equipment (choppers, jaws, and shutters). Extension of this distance by even 20%, to 18 m, is calculated to reduce the flux on sample by 30%, albeit with a modest increase in resolution, particularly in backscattering. Incorporating a neutron guide could significantly increase the flux of longer-wavelength neutrons, particularly for $\lambda > 1.5 \text{ \AA}$. However, this increase in flux comes at the expense of increased divergence of the beam; it is currently anticipated that no guides will be incorporated in NOMAD. Beam divergence can be minimized through the use of Soller collimators, and current assumptions include these

collimators in the incident beam. Given the advances anticipated in neutron optics as a result of the overall SNS program, these baseline assumptions will continue to be reviewed through the early stages of design on this project.

5.3 SAMPLE AND DETECTOR CONSIDERATIONS

The science needs described in the preceding section will require a range of sample environments. The sample chamber will be designed to accommodate sample environments ranging from simple ambient-temperature, thin-walled cells through furnaces, cryostats, pressure cells, and containerless (levitated) samples. Close coordination with the SNS Sample Environment Group is anticipated to permit the efficient use of ancillary equipment developed for other instruments on NOMAD.

In view of the importance of scattering statistics needed to unravel the challenging problems of atomic-level and nanoscale structure in systems with minimal long-range order, the arrangement and type of detectors will be primary performance (and cost) drivers for NOMAD. Specific needs for high stability and high count rates are central factors in choosing and arranging detectors for this instrument. Detectors currently envisioned for NOMAD may be separated into three general sets of banks: (1) a series of banks at low scattering angles ($1 \leq 2\theta \leq 50^\circ$) with secondary flight paths ranging from 0.5 to 4 m; (2) banks near 90° ($70 \leq 2\theta \leq 110^\circ$) with a secondary flight path of 1.5 m at 90° ; and (3) high-angle/backscattering banks ($130 \leq 2\theta \leq 170^\circ$) with a 1.7-m flight path at 150° . This detector arrangement, illustrated in Fig. 5.3, allows each low-angle detector bank to be centered approximately on the axis of the instrument, provides continuous angular coverage from ($1 \leq 2\theta \leq 50^\circ$), and requires a minimum detector area for maximum coverage in scattering solid angle.

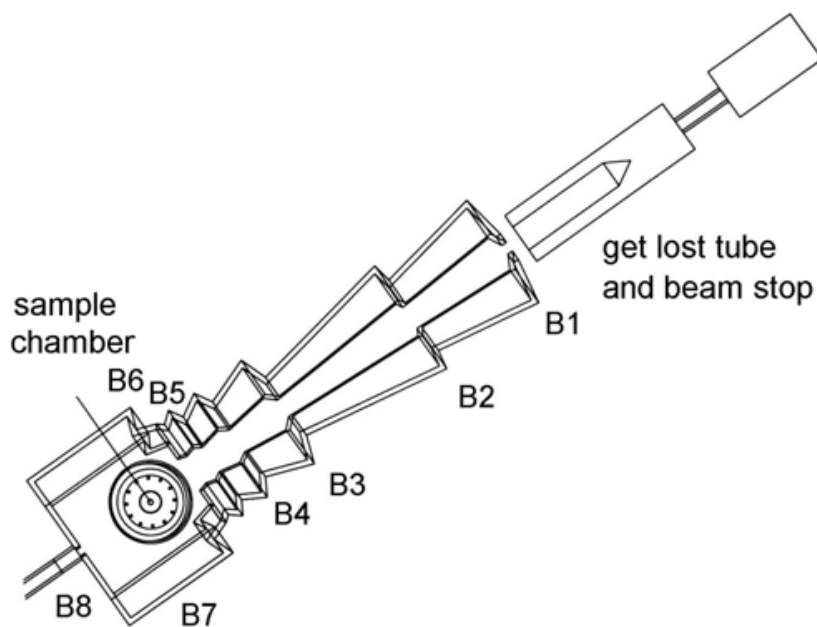


Fig. 5.3. Conceptual arrangement of detector banks on NOMAD.

With the extent of solid-angle coverage needed to provide maximum performance of NOMAD, detectors are expected to be the single largest component of instrument cost. Throughout design and construction, we expect to take full advantage of the advances in detector technology expected as a result of ongoing detector research and development within the SNS project. ^3He detectors require relatively high gas pressures to improve efficiency in detecting short-wavelength neutrons. The reliability and stability of these detectors make them an attractive choice to meet the stability requirements for NOMAD,

but further investigation of the performance of these detectors at higher internal pressure is needed. Currently, the detectors used extensively for detecting short-wavelength neutrons incorporate ${}^6\text{LiF}$ in ZnS screens, as used on the SANDALS instrument at ISIS. However, the screens are opaque to their own light, complicating light collection from thick scintillators, and have shown some instability arising from thermal fluctuations. A new isotopically selected ${}^6\text{LiGd}(\text{BO}_3)_3$ scintillator has shown promise as a transparent, thick scintillator material, but the cost of isotopically enriched gadolinium might be prohibitive. A sol-gel scintillator incorporating ${}^6\text{Li}$ in a cerium-activated lithium aluminoborate glass has been fabricated in thick transparent pieces; this technology appears promising, but more testing is needed. Zinc borate solid-state detectors, which would have universal appeal for scattering instruments, are being developed at ORNL. A decision on the possible use of this detector system must await further development of the technology. A considered decision based on advances in detector technology will be made during the design process.

5.4 COMPARISONS WITH OTHER INSTRUMENTS

Two other instruments that could in principle meet some of the science needs for NOMAD are either under construction or under consideration for SNS. A diffractometer optimized for studies under extreme pressure has been proposed. This instrument will be a high-flux, medium-resolution, highly compact instrument designed specifically around pressure cells. The secondary flight path is very short and the detectors are highly pixilated, thus enabling studies of single crystals. The beam is primarily thermal; that is, high energies are not required as for studies of samples containing light atoms. The detector coverage will likely range from $30 \leq 2\theta \leq 150^\circ$ (centered on 90°), so it does not have the low-angle detector coverage required for optimum glass studies. Including the capability for elevated-pressure sample environments in NOMAD will complement and significantly expand the capabilities of the high-pressure instrument for studies of locally ordered materials over a wide range of pressures; the limited detector coverage and incident-wavelength range of the high-pressure instrument would severely limit its use for the investigations anticipated on NOMAD. A new powder diffractometer (POWGEN3) is also moving toward construction at SNS. The conceptual design of this instrument features high resolution and wide detector area. However, to provide suitable resolution, the incident flight path is significantly longer than anticipated for NOMAD, with correspondingly decreased flux on sample. This lower flux, coupled with the anticipated heavy use of POWGEN3 for its own scientific user base, make it impossible to carry out leading-edge studies of locally ordered systems on this instrument.

The performance characteristics anticipated for NOMAD can be compared with current best-in-class instruments at other world-class spallation source, that is, the SANDALS (liquids) and GEM (crystallography) instruments at ISIS. NOMAD is conceived to incorporate extensive coverage of solid angle at low scattering angles, similar to SANDALS, but with added 90° and higher-angle detector banks for studies of local disorder in crystalline solids and nanoparticulate samples. For these materials, the resolution in high-angle scattering (0.25% at $2\theta = 150^\circ$) is essentially equivalent between NOMAD and GEM. Coupled with the advantages of source flux from SNS, ~ 12 times that of ISIS, Table 5.1 shows the expected strong contributions from NOMAD to the science of local and nanoscale order in condensed-phase samples.

Table 5.1. Comparison of NOMAD characteristics with current benchmark instruments

	NOMAD	GEM	SANDALS
Incident flight path (sample solid angle)	15 m (0.9 mster)	17 m (0.7 mster)	11 m (1.6 mster)
Final flight path (low-angle banks)	0.42–4.0 m	2.9 m	0.75–4.0 m
Final flight path (90° banks)	1.5 m	1.38 m	No detectors
Final flight path (backscattering)	1.5 m	2.0 m	No detectors
Angular detector coverage (low-angle banks)	(1 ≤ 2θ ≤ 50°)	(6 ≤ 2θ ≤ 45°)	(3.8 ≤ 2θ ≤ 40°)
Angular detector coverage (90° banks)	(70 ≤ 2θ ≤ 110°)	(79 ≤ 2θ ≤ 104°)	No detectors
Angular detector coverage (backscattering)	(130 ≤ 2θ ≤ 170°)	(142 ≤ 2θ ≤ 169°)	No detectors
Detector coverage	~6.5 steradians	~3.5 steradians	~2.2 steradians
Resolution (low-angle; 90°; backscattering)	5%, 0.5%, 0.25%	5%, 0.5%, 0.25%	4%, N/A, N/A
Q range	0.015–100 Å ⁻¹	0.15–50 Å ⁻¹	0.05–50 Å ⁻¹

6. HYBRID SPECTROMETER (HYSPEC)

6.1 HYSPEC INSTRUMENT OVERVIEW

The primary objective in formulating the design of the HYSPEC spectrometer was that it delivers the highest possible monochromatic flux to few-cm-sized samples over a broad range of thermal and subthermal neutron energies (5–90 meV). An additional goal was to develop a design that would (1) minimize beam-related background such as that arising from sample environments, (2) provide reasonably good (and easily adjustable) energy and scattering vector resolution ($\delta E/E \sim 0.02 - 0.15$; $\delta Q/Q \sim 0.005 - 0.1$), (3) be readily adapted to polarization analysis, (4) permit rapid alignment of samples and easy installation of specialized sample environments, and (5) allow for straightforward, direct, on-line monitoring and analysis of incoming data. Ultimately these criteria led to the direct geometry, hybrid concept shown schematically in Fig. 6.1. The instrument main design parameters are summarized in Table 6.1.

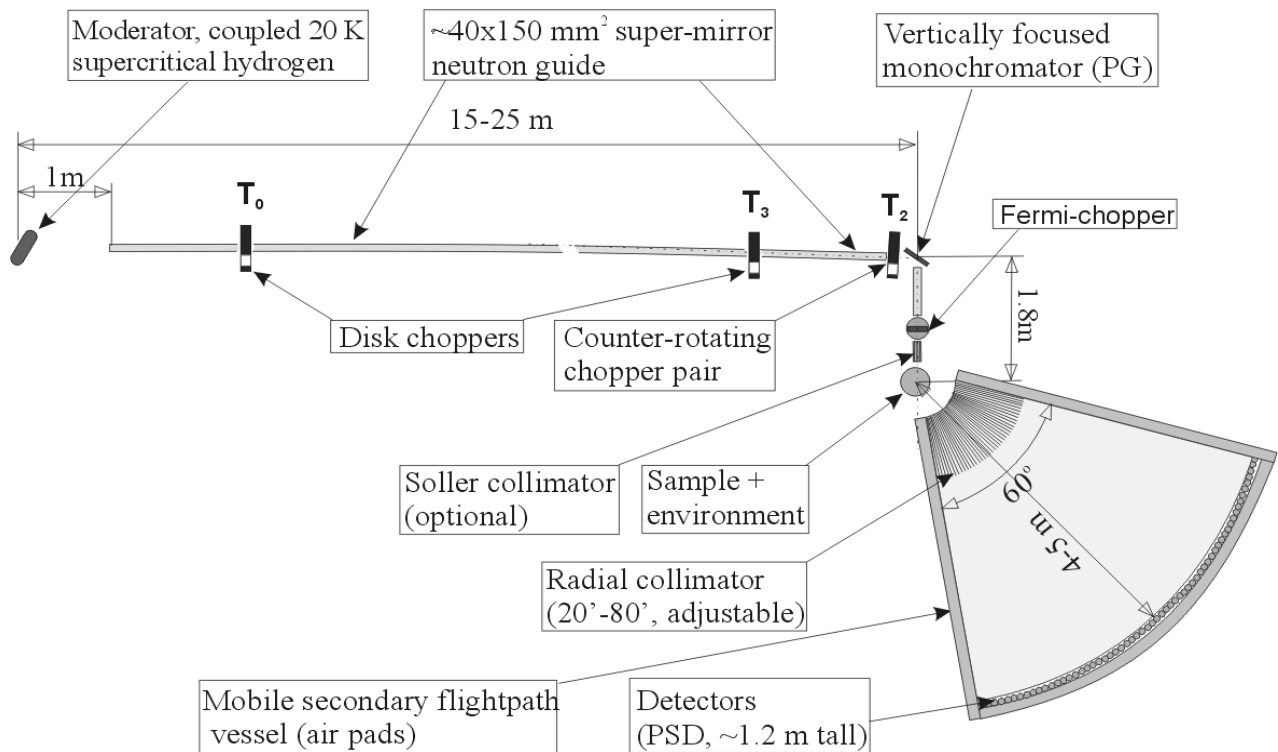


Fig. 6.1. Schematic showing the HYSPEC principle elements.

Table 6.1. Instrument parameters

Moderator	Coupled, 20 K, supercritical H ₂
Incident energy	5–90 meV
Energy resolution	0.02 $\Delta E/E$ <math>< 0.15</math> (for elastic scattering), depending on neutron energy and rotation rates of choppers
Q resolution	$\Delta Q/Q \sim 0.005 - 0.1$
Primary flight path	Guide with expander and compressor sections 20–25 m long
Secondary flight path	4.5 m
Energy defining choppers	Counter-rotating disk and Fermi choppers. Maximum rotation rate, 300 Hz
Frame-overlap/order suppressor choppers	Disk choppers. Maximum rotation rate, 60 Hz
Flux focusing crystal	Segmented, vertically curved pyrolytic graphite and fluorinated mica. Heusler for polarized beam
Sample position	1.8 m from crystal
Beam size at sample (optimally focused)	4 (w) \times 2 (h) cm ²
Detectors	188 2.5-cm–diam, position-sensitive ³ He tubes. Horizontal pixel resolution, 20 min. Vertical pixel resolution, 20 min. Horizontal array acceptance, 60°. Vertical array acceptance, $\pm 7.5^\circ$
Sample environment	Will accept all standard sample environment equipment

6.2 PRIMARY SPECTROMETER (MONOCHROMATOR)

Incident neutron energy will be defined by the time of flight in the primary spectrometer. Reflection from the vertically curved monochromator crystal in most cases will serve only to focus the beam onto the sample. In addition, the monochromator will serve in place of the pulse-shaping chopper, cutting the unwanted high-energy tail of the spectral distribution of the incident neutrons, as shown in Fig. 6.2. The primary spectrometer is envisioned as consisting of a 20- to 25-m-long guide with a center section composed of 40-mm-wide by 150-mm-high, supermirror-coated modules and with 40-mm-wide expander sections at each end, as shown in Fig. 6.1. Whether the guide will be straight or slightly curved is still an open question that will ultimately be resolved by detailed shielding studies. Placed at intervals along the guide would be three disk choppers; the T₀ and frame-overlap choppers—rotating at either the source frequency or a submultiple—and a counter-rotating disk chopper pair, rotating at integral multiples of the source frequency. A rotating drum shield containing a vertically focusing crystal, a beam stop (or, if a straight guide is used, a “get lost” pipe), a vertically tapered guide, a Fermi chopper, and a Soller collimator will be placed at the guide’s downstream end. Attached to the shield—and moving with it—would be a conventional sample rotation stage mounted on air pads, with a 2-axes goniometer capable of supporting large, off-center loads. In such an arrangement, neutron energies are determined both by the beam exit angle (as defined by the crystal and the in-shield collimator), and by the phase of rotation of the counter-rotating chopper pair and/or the Fermi chopper relative to the source. Apart from its energy-defining function, the crystal, together with the section of vertically tapered supermirror guide in the drum shield, also has the important function of efficiently focusing the beam at the sample position.

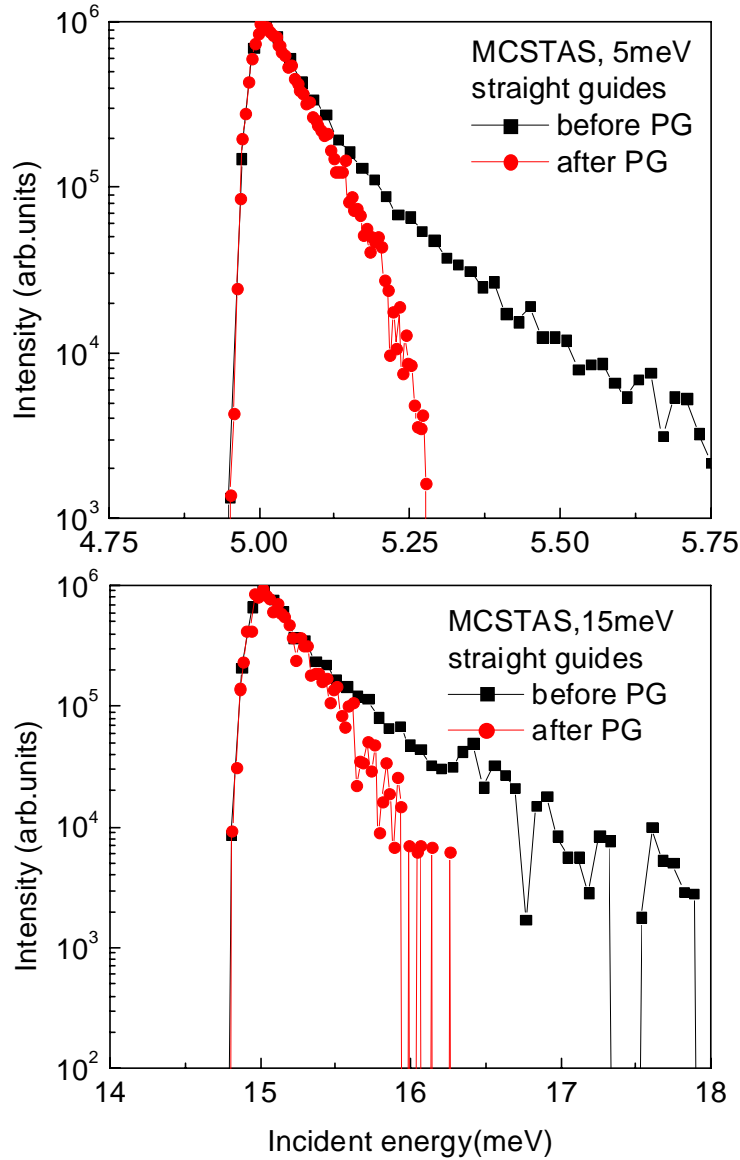


Fig. 6.2. Incident neutron spectrum before and after reflection from a PG monochromator: (a) $E_i = 5$ meV; (b) $E_i = 15$ meV.

Each chopper has a unique role in defining the monochromatic incident beam. The T_0 chopper blocks the gamma rays and high-energy neutrons emitted in the earliest part of the source pulse. The frame overlap chopper (T_3) ensures that unwanted, higher-order (shorter-wavelength) neutrons are removed. Also, its rotation rate can be reduced when necessary to block alternate source pulses in cases where the scattered energy spectrum is so broad that spectral overlap becomes a problem. In the main, medium-resolution, high-data-collection-rate mode of operation, the counter-rotating disk choppers T_2 (together with the crystal) will define both the energy of the beam and the spectral and time width of the pulse at the sample position, the latter being the main factor in determining the energy resolution of the time-of-flight analyzing section. In those cases where higher energy resolution is needed, it is envisioned that the time width of the sample pulse would be further reduced by the addition of a Fermi chopper (T_4). This chopper would have short, straight slots and a vertical axis of rotation and be located in the shield

immediately upstream of the collimator. Like the counter-rotating disk choppers, it would rotate at integral multiples of the source frequency.

For the focusing crystal, we propose using (for nonpolarized applications involving incident neutron energies of 5 meV and higher) individual pyrolytic graphite (PG) plates attached to a segmented holder. This arrangement will provide optimal vertical focusing over the entire 5- to 90-meV neutron energy range. Because a relatively broad horizontal mosaic (probably 1.0°) will be needed for optimum performance, we plan to use sets of three ZYA grade PG plates stacked with spacers to slightly offset the angles between them. This so-called “fanned arrangement” has been demonstrated to expand the horizontal mosaic but leaves the vertical mosaic (and thus the vertical focusing properties of the crystal) unchanged. At incident neutron energies below 5 meV, where high monochromator scattering angles hamper measurements because of the excessively tight resolution introduced by the PG crystal in a near backscattering geometry and space restrictions, we envision substituting an equivalent crystal composed of fanned plates of fluorinated synthetic mica.

6.3 SAMPLE STAGE

As emphasized in Section 6.1 it is important for many of the areas of research for which HYSPEC is intended that specialized sample environments can be easily and quickly installed. Because the collimation upstream and downstream of the sample will restrict the horizontal field of view of the detectors to the sample area alone, the HYSPEC sample axis will not have to be part of the instrument vacuum system as in other planned inelastic instruments. Thus, we expect to be able to employ conventional cryostats, magnets, furnaces, pressure cells, etc., without creating any significant, sample-environment-related background problems. This is another unique feature of HYSPEC.

6.4 SECONDARY SPECTROMETER (ANALYZER/DETECTOR)

Scattered neutron energy analysis would be done by time of flight alone. We propose using a 4.5-m radius array made up of 188 one-dimensional, position-sensitive, tube-type ^3He detectors 2.5 cm in diameter and 1.28 m long, centered at the sample position. A set of radial collimators (with horizontal angular acceptances of 20, 40, 60, and 80 min) interposed between the sample and detectors would restrict their horizontal field of view to the sample area alone. Horizontal and vertical resolutions of an individual pixel are envisioned as being, respectively, 20 and 20 min of arc. Additionally, the array would span a 60-degree arc horizontally and have a vertical acceptance of ± 7.5 degrees with respect to the scattering plane. It would be mounted on air pads on a “tanzboden” so that it could both move with the drum shield and be rotated about the sample axis to permit accurate positioning with respect to the monochromatic beam incident on the sample. The detector area would most likely be gas filled and located in a fixed, well-shielded housing.

6.5 POLARIZATION ANALYSIS

One of the particularly attractive features of the HYSPEC concept is that it can quickly and easily be adapted to polarization analysis. All that is required is that the focusing crystal used for nonpolarized studies be replaced by a crystal that both focuses and polarizes the monochromatic beam incident on the sample and that polarization analyzers be installed between the sample and detectors. The crystal we propose using for polarized applications and the selection of a polarization analyzer will be addressed in the following sections.

6.5.1 The Polarizing Crystal

Polarizing crystals are crystals of ferromagnetic materials with low index Bragg peaks in which the nuclear and magnetic contributions to the coherent scattering add for one of the two neutron spin states and subtract and cancel for the other when the atomic magnetic moments are fully aligned by an external magnetic field. Of those investigated to date, the consensus view is that the Heusler alloy crystal Cu_2MnAl is the best choice in terms of both reflectivity and polarizing efficiency. Detailed studies, such as those made, for example, by A. Freund et al,²¹ have shown (1) that well-annealed Cu_2MnAl crystals have (111) Bragg reflecting efficiencies that can approach those expected for ideally imperfect crystals, (2) that the polarization of the reflected neutrons is in excess of 95% in crystals in which the manganese moments are fully aligned in an external field produced by permanent magnets, and (3) that there is no significant loss of polarization when individual crystal plates are mounted so as to form a cylindrically curved, vertically focusing array.

We are aware that Cu_2MnAl crystals, like all polarizing crystals, are not without problems. One problem is that the procurement of crystals of good quality has been difficult in the past. We have been advised, however, that they can now be obtained from the Institute Laue-Langevin (ILL). A second problem is that the nuclear and magnetic contributions to the (222) Bragg reflection are not well matched and second-order contamination of the reflected beam can significantly reduce the polarizing efficiency. Fortunately, this is ruled out as a potential problem for HYSPEC because the upstream choppers will deliver a higher-order-free, monochromatic beam to the crystal. A third problem is the issue of parasitic Bragg reflections that are known to have a non-negligible impact on both the polarizing efficiency and reflectivity and are likely to impair performance at certain neutron energies. The time-honored way to side step this difficulty is simply to choose a crystal orientation that gives optimal performance at the energy at which the spectrometer will most often be used, in this case 15 meV, and incorporate messages into the operating software that warn experimenters about operating at those incident neutron energies where the polarizing efficiency and/or reflectivity is significantly affected by parasitic reflections. Because this will somewhat limit experimental flexibility, it is our intention to explore the feasibility of fabricating the individual plates in the vertical focusing array from stacks of 0.5-mm thick wafers cut from Cu_2MnAl single crystals. There are two potential advantages of this so-called “composite crystal” approach. One is that composite wafer stacks are not as spatially coherent as monolithic crystals, which reduces parasitic reflections. The other advantage is that introducing mosaic into the wafers by single-axis deformation before they are bonded together creates a highly anisotropic mosaic that improves the reflectivity without impacting the vertical focusing.

6.5.2 The Polarization Analyzers

Signal and background are typically of comparable intensity in polarization analysis measurements. Translated into practical terms, this means that definitive determination of the signal polarization will only be possible if both the polarizer and polarization analyzer have polarizing efficiencies in the 0.80–0.95 range. Heusler alloy polarizer crystals, which produce polarizations on the order of 0.90–0.95, easily meet this standard over the neutron energy range in which HYSPEC will operate. Because they are of comparable efficiency and are both well tested and maintenance free, our choice for analysis of the polarization of the scattered neutron beam is the supermirror-bender polarization analyzer. Reduced to essentials, this type of analyzer is nothing more than a short, curved multichannel guide with magnetically aligned, polarization-selective Fe-Si supermirror films on the channel walls. Because the angles of total reflection of the + and – spin states differ by more than a factor of three in such films, neutrons of one spin state tend to follow the curved channels, while those of the other continue in their original direction. The incident beam is thus divided into divergent beams of opposite polarization. When the beam is well collimated and the bender optimally curved and tilted, polarization analyzing efficiencies in the 0.80 to 0.95 range are easily achieved. Moreover, at sufficient analyzer-to-detector distances, the two beams become spatially separated and both polarizations can be observed at the same time.²²

To make the most effective use of the extended angular acceptance of the HYSPEC detector array, an equivalent array of bender analyzers would need to be installed, each directly downstream of a 20-min angular acceptance collimator. Like all such analyzers currently in use, we envision that the bender channels would be formed by single-crystal silicon wafers with surface coatings of Fe-Si supermirror film. For HYSPEC, the wafers would be 0.25 mm thick, 5 cm long and 14 cm high. To perform optimally at 15 meV, they would be horizontally bent to a radius of about 5 m. Packed in groups of 80 into 3-cm exterior width, thin-walled aluminum alloy containers, the wafer packs would form 2-cm-wide, 80-channel benders. Room-temperature, single-crystal silicon, it should be noted, is sufficiently transparent to neutrons in the energy range of interest that scattering and absorption losses would not exceed 10%. Permanent magnets would be used to align the iron moments in the Fe-Si films. Assuming the closest possible packing of the containers along an arc 55 cm from the sample axis, 19 such bender analyzers could be positioned within the (60 degree horizontal and 15 degree vertical) solid angle subtended by the detector array.

From the MC simulation shown in Fig. 6.3, it is evident that the spatial profiles of the two oppositely polarized beams would be completely separated at the detector bank 4.5 m from the sample axis. It is also evident from the figure that the undeflected beam will spread over two (2.5-cm-diam) detectors and the oppositely polarized (somewhat wider) beam following the curved channels and will fall on the adjacent three detectors. Considering that each bender analyzer unit would be centered on a group of 10 detectors, 50% of the detector array would be actively collecting data in this arrangement (which is very nearly optimum from the standpoint of maintaining adequate spatial separation of the beams from adjacent analyzers). Note that although each of the 19 analyzers is limited to a specific scattering angle, rotation of the detector bank around the sample axis will make it possible to cover—sequentially—the full scattered neutron angular range. No more than ten rotational steps of the detector would be needed to monitor both the flipped and unflipped spin intensities over the full 60-degree angular range covered by the detector array. It is also clear from Fig. 6.3 that the flipping ratio measured in some detectors is higher than that in the others (in which the peak of the “wrong” polarization occurs). Therefore, if the signal is sufficiently strong, it is possible to enhance the polarization sensitivity by restricting the counting to the detectors with the highest flipping ratios. This is equivalent to tightening the beam collimation after the bender polarizer but could be accomplished with the experiment analysis software without repeating the actual measurement. Such flexibility is another attractive feature of the supermirror-bender polarization analysis scheme proposed for HYSPEC.

Figure 6.4 shows a MC simulation of bender analyzer performance over a range of energies on either side of 15 meV. From this it is evident that benders designed for optimum polarizing efficiency at 15 meV will operate with little loss of efficiency over an energy range extending from roughly 8 to 18 meV. A second set of essentially identical bender analyzers configured for optimum performance at 5 meV would cover the energy range from about 3 to 8 meV with about the same efficiency, making it possible to span the entire scattered neutron range from 3 to 18 meV.

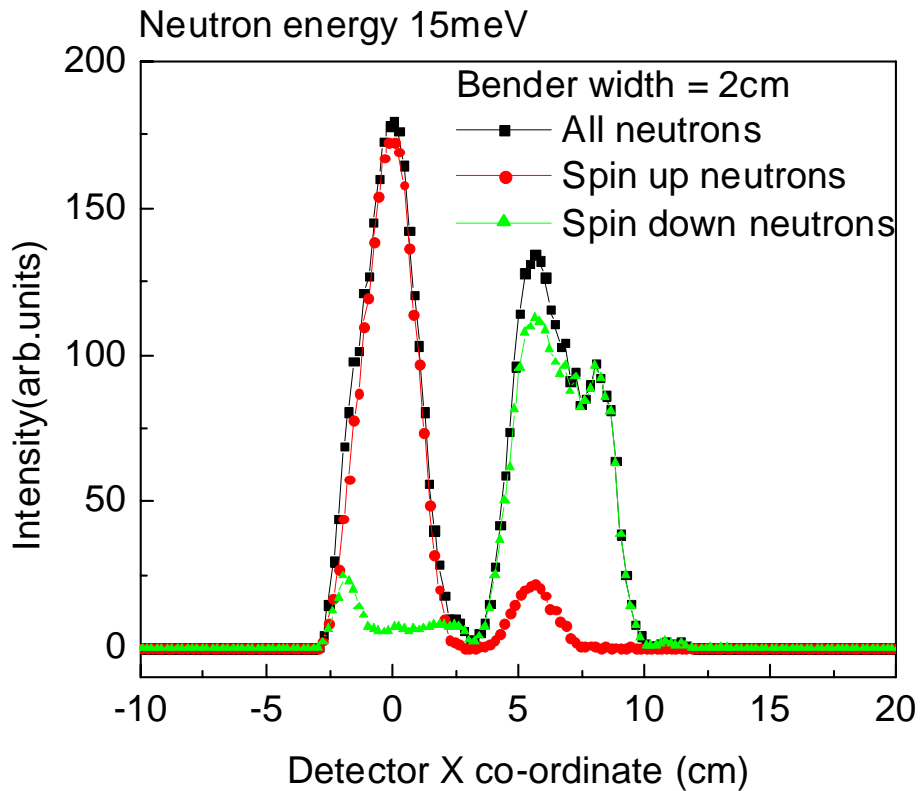


Fig. 6.3. Spatial distribution of two neutron polarizations on the detector as created by a single supermirror-bender.

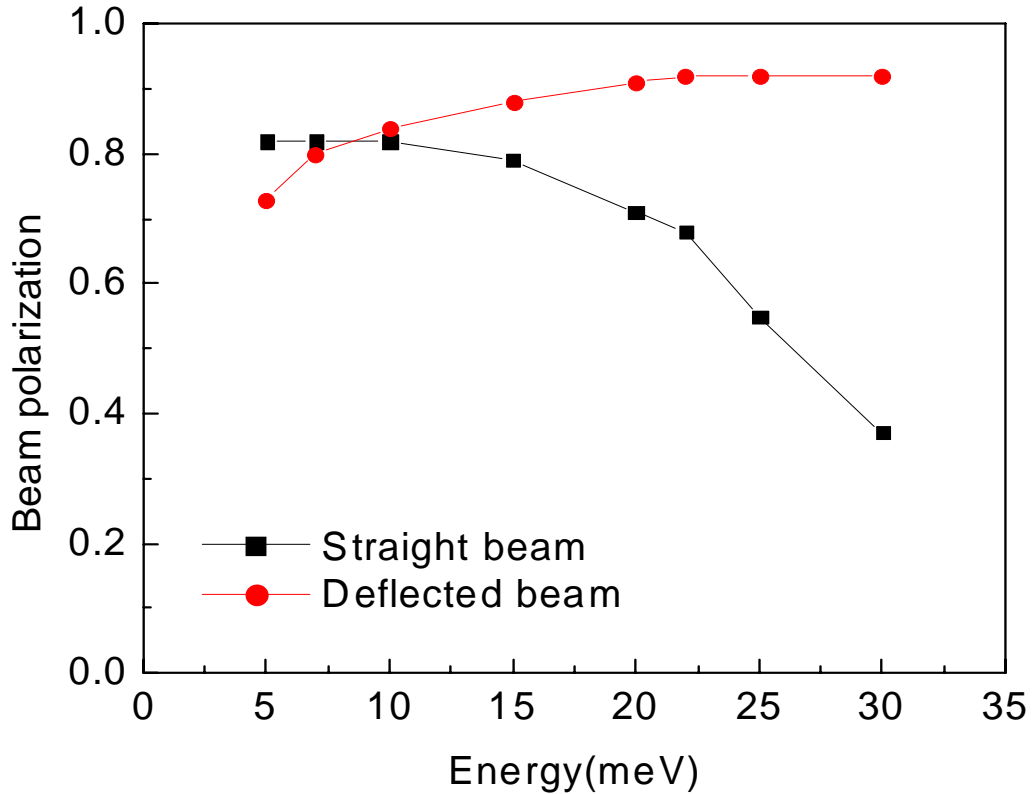
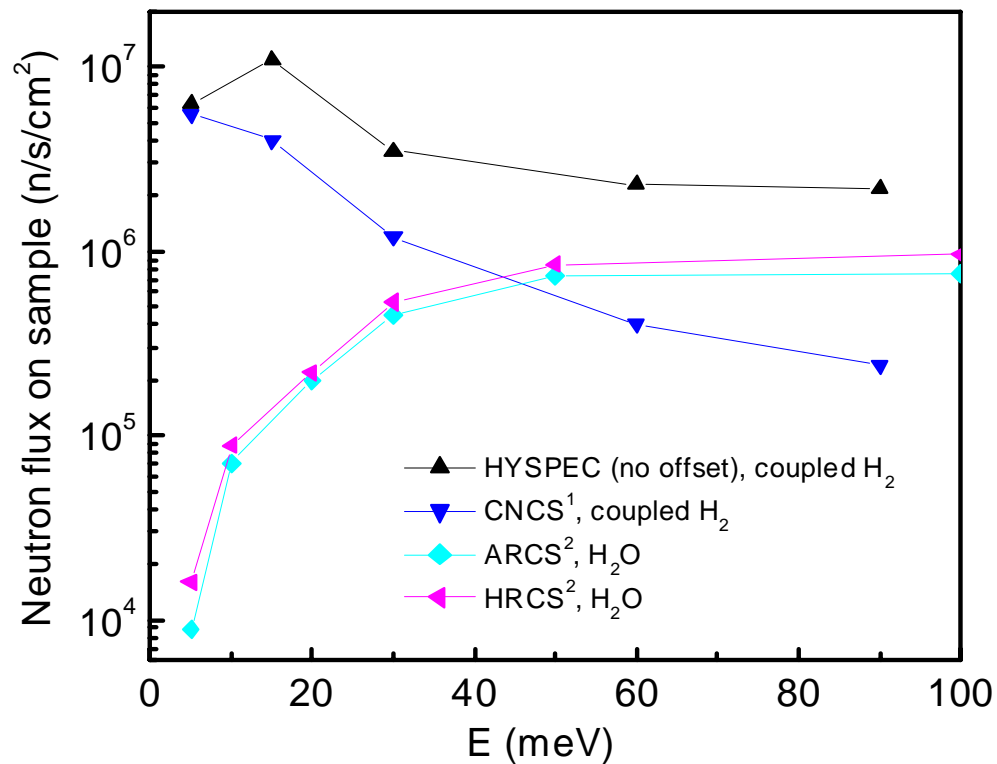


Fig. 6.4. Average beam polarization in each of the two beams.

Probably the most attractive feature of using bender analyzers in a time-of-flight energy analyzing system like HYSPEC's is the capability of monitoring *both* scattered neutron spin states simultaneously over a relatively broad scattered neutron energy range. But there are other attractions as well: bender analyzers are extremely stable and, as noted previously, once built require little or no attention and are completely maintenance free.

6.6 PERFORMANCE

Of the many special features of HYSPEC, the most important from the viewpoint of efficient use of source neutrons is the use of the superior focusing properties of curved crystals to concentrate the monochromatic flux on sample. To quantify the advantage of the HYSPEC concept in this respect, a number of MCSTAS, MC-based, flux-on-sample simulations were made to compare HYSPEC's flux on sample with that of other proposed SNS inelastic instruments. As is shown in Fig. 6.5, despite the finite reflectivity of the PG crystal, its superior focusing properties concentrate the monochromatic flux more effectively than converging guides over the greatest part of the energy range in which HYSPEC will operate. For the moderate-resolution, single-crystal sample studies for which it is planned, the HYSPEC approach is markedly superior.



¹CNCS model based on "Optimization...", J.V. Pearce et al.

²G. Granroth, Private communication

Fig. 6.5. Calculated flux on sample for HYSPEC and other inelastic spectrometers planned for SNS.

6.6.1 Moderator Choice

MC simulations have also shown that to perform optimally over the incident neutron energy range of interest (5–90 meV), a spectrometer of this type needs to be located on a beam line served by a coupled, 20 K, supercritical H₂ moderator. Because optimum performance requires that the monochromator and analyzer energy resolutions be reasonably well matched, the length of the monochromating section should not be much greater than 20 m. It is also important that it ends at a place on the SNS experimental floor where there is sufficient space to accommodate both the rotating drum shield and the relatively extended time-of-flight analyzer and its associated shielding. Lengthening the incident flight path beyond the length specified here would lead to a mismatch between the monochromating and analyzing resolutions and a corresponding reduction of monochromatic flux at the sample position for the same overall resolution.

6.6.2 Additional Advantages of the HYSPEC Concept

Apart from the aforementioned features, HYSPEC has many other attractive properties:

- Incident neutron energy selection and analysis of scattered neutron energies would be primarily by time of flight; thus, full advantage is taken of the pulsed beam.
- Only two components—the counter-rotating chopper pair and the Fermi chopper—would operate at high rotation speeds. Both would be of conventional design and would operate well within the limits imposed by the tensile strengths of the available materials.
- Moving the sample out of the direct beam and placing shielding between it and the detectors is expected to reduce beam-related background to a minimum.
- Near-forward sample scattering will be accessible to investigation.
- Depending on the type of measurement, the spectrometer operation could be optimized for either a wide angular acceptance or a selected **Q**-range.
- Apart from its focusing properties, the crystal also has the important effect of substantially reducing the (source-produced) spectral asymmetry of the beam incident on the sample: the energy resolution function will be more symmetrical than on other instruments on coupled moderators.
- A relatively wide primary beam (4 cm) will be available, thus making it possible to fully illuminate both large and small samples.
- A broad and continuous range of incident neutron energies ($5 \leq E_i \leq 90$ meV) will be accessible without order contamination.
- Energy resolution can be incrementally varied simply by changing the rotation rate of the counter-rotating and/or Fermi choppers.
- By changing the collimation of the incident monochromatic beam or the angular acceptance at the analyzer (or both), the longitudinal **Q**-resolution can easily be varied.
- Various kinds of monochromating crystals with a variety of focusing options could be employed, such as two-dimensional focusing, asymmetrically cut, perfect-crystal focusing.

6.6.3 Future Considerations

Yet to be addressed in detail are two design issues. The first and most important relates to keeping the background to a minimum: a choice will have to be made between a curved guide with a beam stop inside the monochromator drum shield and a straight guide with a “get-lost” pipe with the beam stop a considerable distance from the data collecting area. The second issue is purely mechanical: the large (and heavy) analyzer of the spectrometer will have to be rigidly coupled to the large (and heavy) monochromator drum shield and move with it when the incident energy is changed. Additionally, the detector array will have to rotate in a precise and reproducible fashion about the sample axis. This, however, does not seem to pose any conceptual difficulty, as similar tasks are successfully accomplished

in the design of several existing modern neutron spectrometers, such as FOCUS at Swiss Spallation Neutron Source SINQ, or a spin-echo machine recently commissioned at the National Institute for Standards and Technology Center for Neutron Research. There is also a location constraint: because the proposed secondary flight path is sufficiently long (nominally 4.5 m) and because the sample axis is offset from the primary beam (1.8 m), the combined drum shield, analyzer, and associated analyzer shielding will require an ample amount of space on the experimental floor and limit the choice of beam lines and allowable minimum moderator-to-monochromator distance.

REFERENCES

1. D. Abernathy, Spallation Neutron Source, Report IS-1.1.8.4-6033-RE-A-00.
2. R. Reidel, Spallation Neutron Source, Report IS-1.7.3.2-4034-SP-A-00.
3. J. Carpenter et al., Argonne National Laboratory, Report ANL-78-88 (1978).
4. C. G. Windsor, "Pulsed Neutron Scattering," Halsted Press (1981).
5. K. Lefmann and K. Nielsen, *Neutron News* **10**, 20, (1999).
6. E. Iverson, Spallation Neutron Source, Report TSR-202.
7. J. K. Zhao and J. Ankner, *A Single Crystal Diffractometer at SNS*, document No. ES-1.1.8.4-6018-RE-A-00.
8. C. C. Wilson, private communication.
9. A. J. Schultz, *Trans. Am. Cryst. Assoc.* **29**, 29 (1993).
10. J. Hodges, *POW-GEN3-High-Resolution General Purpose Powder Diffractometer Conceptual Design Study* (IS-1.1.8.2-6034-RE-A-01) (2001).
11. A. Evdokimov, A. J. Gilboa, T. F. Koetzle, W. T. Klooster, A. J. Schultz, S. A. Mason, A. Albinati, and F. Frolow, *Acta Cryst.* **B57**, 213 (2001).
12. D. Keen, private communication.
13. E. Iverson, *HPTS design basis model as of 2/21/01*; <http://www.sns.anl.gov/components/moderators.shtml> (2001).
14. J. X. Ho, E. H. Snell, R. C. Sisk, J. R. Ruble, D. C. Carter, S. M. Owens, and W. M. Gibson, *Acta Cryst.* **D54**, 200 (1998).
15. Equation 2.1, p. 105 of *Methods of Experimental Physics, Neutron Scattering*, Vol. 23, Part A.
16. J. M. Carpenter and D. F. R. Mildner, *Nucl. Instr. Meth.* **A196**, 341 (1982).
17. J. R. D. Copley, *Nucl. Instr. Meth.* **A287**, 363 (1990).
18. A. J. Schultz, Argonne National Laboratory (2000).
19. C. A. Tulk, *Conceptual Design of a Disordered Materials Diffractometer for the Spallation Neutron Source*, SNS Project Document IS-1182-6046-RE-A-00. (2001).
20. W. S. Howells, *Nucl. Instrum. Methods Phys. Res., Sect. A* **223**, 141-146. (1984).
21. A. Freund, et al., *Physica* **120B**, 86 (1983).
22. S. H. Lee and C. F. Majkrzak, *J. Neutron Res.* **7**, 131 (1999).